**RIGA TECHNICAL UNIVERSITY**

Faculty of Civil Engineering
Institute of Structural Engineering and Reconstruction

**Andrejs PUPURS**

# LOAD BEARING CAPACITY PREDICTION OF STEEL FIBER REINFORCED CONCRETE ELEMENTS SUBJECTED TO BENDING LOADS

**Dissertation Thesis**

Scientific supervisor
Dr.sc.ing. professor
Andrejs KRASŅIKOVS

**Rīga 2011**


This work has been supported by the European Social Fund within the project “Support for the implementation of doctoral studies at Riga Technical University”.

**PROMOCIJAS DARBS**
**IZVIRZĪTS RĪGAS TEHNISKĀS UNIVERSITĀTES**
**INŽENIERZINĀTŅU DOKTORA GRĀDA IEGŪŠANAI**

Promocijas darbs inženierzinātņu doktora grāda iegūšanai tiek publiski aizstāvēts 2011.g 9.decembrī, plkst. 14:30, Rīgas Tehniskās universitātes Būvniecības fakultātes sēžu zālē, Āzenes ielā 16, promocijas padomes "RTU-P06" atklātā sēdē.

OFICIĀLIE OPONENTI

Profesors, Dr.habil.sc.ing. Jānis Brauns
Latvijas Lauksaimniecības Universitāte

Vecākais zinātniskais līdzstrādnieks, Dr.sc.ing. Jānis Andersons
Latvijas Universitāte, Polimēru Mehānikas institūts

Emeritētais profesors, Dr.sc.ing. Ralejs Tepfers
Chalmers University of Technology, Zviedrija

APSTIPRINĀJUMS

Es apstiprinu, ka esmu izstrādājis doto promocijas darbu, kas iesniegts izskatīšanai Rīgas Tehniskās universitātes inženierzinātņu doktora grāda iegūšanai. Promocijas darbs nav iesniegts nevienā citā universitātē zinātniskā grāda iegūšanai.

Andrejs Pupurs …… (Paraksts)

Datums: 02.09.2011.

Promocijas darbs ir uzrakstīts angļu valodā, satur Anotāciju, Ievadu, 5 nodaļas, Secinājumus, Literatūras sarakstu, Pielikumu, 97 attēlus, kopā 157 lappuses. Literatūras sarakstā ir 94 nosaukumi.

# ANOTĀCIJA

Pašreizējie Eiropas un Pasaules fibrobetona pētnieku un inženieru veiktie zinātniskie un izpētes darbi galvenokārt mērķēti vispārēju un starptautiski atzītu projektēšanas normatīvu izstrādei. Vienotu projektēšanas normatīvu iztrūkums jau vairākus gadus kavē fibrobetona pielietošanu daudzās konstrukcijās un, neraugoties uz tā acīmredzamām priekšrocībām, pretrunas esošajās fibrobetona konstrukciju projektēšanas rekomendācijās ierobežo inženiera izvēli par labu fibrobetonam.

Tādēļ šobrīd ir svarīgi dot pētniecisku ieguldījumu, kas sekmētu fibrobetona normatīvu izstrādi, veicot oriģinālus eksperimentālus pētījumus un izstrādājot modeļus fibrobetona konstruktīvo elementu nestspējas un darbības prognozēšanai.

Kamēr fibrobetona stiprības īpašību noteikšanai lielākā daļa no šobrīd pieejamām projektēšanas rekomendācijām pielieto inverso modelēšnas pieeju (aproksimējot eksperimentāli iegūtas līknes), ir jāatzīmē, ka tiešā modelēšans pieeja fibrobetona projektēšanā ļautu iegūt ekonomiskākus konstruktīvos risinājumus un reālistiskākus fibrobetona elementu darbības raksturošanas modeļus, ievērtējot faktisko šķiedru veidu, daudzumu un orientāciju.

Tādēļ šī promocijas darba mērķis ir izstrādāt modeli fibrobetona konstruktīvo elementu nestspējas prognozēšanai plaisu izveidošanās un to atvēruma palielināšanās stadijā, izmantojot tiešo modelēšanas pieeju. Piedāvātais modelis ir izstrādāts vienkāršā formā ar nolūku, lai tas nākotnē būtu piemērojams lietošanai konstrukciju projektēšanas normatīvajos dokumentos. Šajā promocijas darbā izstrādātais modelis ir piemērots liektu fibrobetona konstruktīvo elementu (siju, plātņu) nestspējas prognozēšanai un tā izstrādāšanas pamatā ir novērojums, ka konstruktīvo fibrobetona elementu nestspēja ir stingri atkarīga no šķiedru izraušanas pretestības. Līdzīga pieeja nākotnē varētu tikt piemērota arī stieptu fibrobeotona elementu nestspējas un darbības prognozēšanai.

Šis promocijas darbs sastāv no 3 galvenajām sadaļām: 3.nodaļā veikta eksperimentāla programma 3 dažādu veidu komerciāli pieejamo tērauda šķiedru izraušanas pretestības noteikšanai. Eksperimentāli noteikta arī šķiedras enkurojuma dziļuma un orientācijas leņķa ietekme uz izraušanas pretestību un dotas šķiedras izraušanas pretestības sakarības dažādām konfigurācijām. 5.nodaļā veikta šķiedras izraušanas procesa skaitliskā modelēšana izmantojot galīgo elementu metodi. Pielietojot plīsumu mehānikas principus, parametriski tika analizēta plaisas starp tērauda šķiedru un betona matricu izplatīšanās. 4.nodaļā veikta arī šķiedras

pilnīga izraušanas procesa skaitliskā modelēšana. No salīdzinājuma un labākās atbilstības ar eksperimentālajiem rezultātiem tika noteikti un svarīgi parametri, kurus eksperimentāla noteikšana ir sarežģīta. Visbeidzot, 5.nodaļā izstrādāts modelēšanas algoritms liektu fibrobetona siju nestspējas prognozēšanai, par modelēšanas ieejas pamatdatiem ņemot iepriekš noteiktās šķiedru izraušanas sakarības. Atšķirībā no vairākuma esošo modeļu, kas pieejami literatūrā un projektēšanas rekomendācijās, šajā promocijas darbā piedāvātais modelis ļauj ievērtēt faktisko šķiedru daudzumu un veidu fibrobetona maisījumā. Modelēšanas rezultātu apstiprināšanai un modeļa lietderības izvērtēšanai tika veikti fibrobetona siju eksperimentāli lieces stiprības pētījumi. Neraugoties uz salīdzinoši vienkāršo modelēšanas pieeju, tika iegūta ļoti laba atbilstība ar eksperimentālajiem rezultātiem, apstiprinot izstrādātā modeļa pielietojamību.

Tā kā liektu fibrobetona elementu nestspēja plaisu izveidošanās un to atvēruma palielināšanās stadijā tika precīzi prognozēta, šis promocijas darbs pierāda iespējas un priekšrocības, ko dod tiešās modelēšanas pieejas izmantošana fibrobetona konstruktīvo elementu projektēšanā, salīdzinot ar inverso pieeju, kas tiek lietota lielākajā daļā no šobrīd pieejamiem fibrobetona konstrukciju projektēšanas dokumentiem. Šis promocijas darbs šobrīd arī ir viens no nedaudziem literatūrā publicētiem zinātniskajiem pētījumiem, kurā pētīts fibrobetons ar lielām šķiedru koncentrācijām ($100-300 kg/m^3$), kādas ir nepieciešamas fibrobetona pielietošanai konstruktīvajos elementos.

# ABSTRACT

At present concrete researchers and engineers in European and world-wide level are focusing their efforts towards developing generally accepted international design regulations for steel fiber reinforced concrete (FRC). It is realised that the lack of generally accepted design regulations has been too long in terms of time and despite the clear advantages of FRC in many applications the use of it has often been limited due to inconsistency of the existing design recommendations.

It is therefore important to contribute to FRC research community with original results and concepts of models for predicting the behaviour of FRC structural elements. While in order to determine the properties of FRC most of the currently available design recommendations use inverse approach (approximation of experimentally obtained relations), the direct approach, on the other hand, can provide more economical and realistic structural design of FRC by evaluating the actual type, amount and orientation of fibers.

The present Thesis therefore is aimed towards elaborating a constitutive model for prediction of load bearing capacity and post-cracking behaviour of FRC structural elements using the direct modeling approach. The model is elaborated in a simple form so that it could be applicable for integration within a structural design document in the future. The modelling procedure described in this Thesis is applicable to FRC structural elements subjected to bending loads, and the main principle of the model is based on the observation that performance of a FRC element strictly depends on the pull-out resistance of fibers. The same principle could be also used in the future for prediction of behaviour of FRC structural elements subjected to tensile loads.

The present Thesis consists of three major parts: in Chapter 3 extensive experimental study of fiber pull-out resistance of three types of commercially available steel fibers is performed. The effect of fiber embedded length and inclination angle is experimentally determined and the average pull-out laws for different configurations are presented. In Chapter 4 numerical modelling of the fiber pull-out process is performed using finite element method. Using fracture mechanics principles, steel fiber/concrete matrix interface debond crack growth is parametrically analyzed. Numerical modelling of the whole pull-out process of straight fibers is also performed in Chapter 4. From comparison and best fit with the experimental results different important parameters are determined that are difficult to measure experimentally. Finally, in Chapter 5 a model for predicting the load bearing

capacity and post-cracking behaviour of FRC beams is elaborated by using the previously obtained fiber pull-out laws. Unlike most of the existing models available in the literature and design recommendations, the model proposed in this Thesis takes into account the actual amount and type of fibers in the FRC mix. FRC beams subjected to 4 point bending were tested experimentally to validate the modelling results and the obtained agreement was very good despite the simplicity of the model.

This Thesis demonstrates the potential and advantages of applying direct approach of modelling to FRC alternatively to inverse methods suggested in most of the available design recommendations since the load bearing capacity and post-cracking behaviour of FRC beams was accurately predicted. The present work is also one of the few studies in literature so far that has been focusing on FRC with high fiber fractions ($100-300 kg/m^3$), which is essential for structural applications.

# PREFACE

The current Dissertation Thesis summarizes my work performed at Riga Technical University, Concrete Mechanics Laboratory during my doctoral studies period between September 2007 and February 2011. For the successful completion of this Thesis I must sincerely express my gratitude to my supervisor, professor Andrejs Krasņikovs. It was back in time, when I was a first year student still rather uncertain of my future career, when his lectures on Resistance of Materials evoked a strong interest in me for scientific work and research challenges. My participation in many European projects, international scientific conferences and collaboration with universities abroad during my doctoral studies has been a great experience, which would not be possible without his support.

I am also grateful to all senior researchers of Concrete Mechanics Laboratory: Dr. Videvuds Ā. Lapsa, Dr. Genādijs Šahmenko and associate professor Olga Kononova whose broad expertise has been very helpful for me during these years. I would also like to express my gratitude to Institute of Structural Engineering and Reconstruction – associate professor Leonīds Pakrastiņš personally for his kind assistance and professor Kārlis Rocēns for his constant interest in my work.

International collaboration with professor Janis Varna of Luleå University of Technology, Sweden, has been especially important for me.

As always, the work in the lab is much easier and more interesting with the support of colleagues – therefore I would like to thank my fellow PhD students Māris Eiduks, Amjad Khabbaz, Arturs Mačanovskis, Angelīna Galuščaka as well as technicians Imants Kļaviņš and Genādijs Koļesņikovs for their assistance and friendliness.

Finally, I would like to express my most sincere gratitude to my parents, my sisters, and especially Līva for being able to support and understand my occupation with this Thesis.

Andrejs Pupurs

Rīga, May 2011

# TABLE OF CONTENTS

# INTRODUCTION

Fiber reinforced concrete (FRC) has been widely considered as one of the most promising building materials for application in civil engineering during the last 20 years. Although first applications of FRC date back to 1960s it was the advances in concrete chemistry during 1990s that allowed obtaining FRC mixes with high fiber amounts while maintaining the workability of the mix. The invention of superplasticizers was an important boost for regaining research and application interest of FRC in civil engineering and other industries. The ability to add high amounts of fibers resulted in a significant improvement of FRC properties that are considered as the most advantageous compared to conventional reinforced concrete structures. High durability, toughness and ductile behaviour, wear and abrasion resistance, micro-crack distribution and crack width control are among the most significant advantages of FRC. The economical factor has also played a key role for gaining popularity of FRC applications: the time and cost saved by adding the fiber reinforcement directly in the concrete mix instead of transportation and mounting of traditional reinforcement bars is very motivating. Important to add is that the economical advantage can also be achieved in form of combined use of continuous reinforcement with fiber reinforcement – in such way not only the necessary amount of steel reinforcement bars can be reduced due to contribution of fibers but also the volume of concrete can be reduced since the thickness of the reinforcement protecting covers can be minimized due to crack control provided by disperse fibers.

Despite the increased interest during the past decades, it has to be realized that there have been several drawbacks associated with FRC that have significantly limited its use in many cases. First of all, the price of the fibers is not low and, without considering the previously mentioned advantages such as labour and time savings as well as long-term durability of FRC, the cost of material volume unit may seem high. Technological difficulties can be mentioned as the second major drawback of FRC. In order to achieve high load bearing capacity of a FRC structural element, high amounts of fibers has to be added according to design calculations. With higher fiber amounts the workability of FRC mix is generally decreased. Therefore, the use of FRC in structural applications is limited since in most cases it is not technologically possible to obtain FRC mix with fiber weight fractions larger than $300 kg/m^3$ and to maintain sufficient workability. Also it has to be realised that being a short fiber ceramic matrix composite, FRC can not in general be considered as a full replacement for conventional reinforced concrete with continuous reinforcement. Workability of FRC is,

however, not the only technological requirement for application in the building industry. Such features as pumpability, sprayability and similar are often required in, for example, tunnelling industry, which is one of the largest application areas of FRC. Usual scenario is the use of the existing pumps and spraying devices that have been developed for plain concrete or for FRC with low fiber amount. Certainly, larger amount of fibers will cause difficulties in operating such equipment and again, the use of FRC in structural applications is thus limited due to purely technological reasons.

Although economical and technological reasons are very important, it is still widely recognized that the most application-limiting drawback of FRC is the lack of unified and internationally accepted design regulations. Although over the past few decades FRC has been a subject broadly studied by both material scientists and engineers, the conclusions of these studies have not been consistent. The typical problem and the main reason for the lack of unified design regulations for FRC is the high scatter observed in experimental test results. And the main reasons for this high scatter are straightforward: there are variances in fiber orientation and fiber distribution in volume and that affects the mechanical properties. Fiber orientation and distribution significantly affects the performance of FRC structural element, but it is difficult to control or even measure experimentally these parameters given the fact of randomness of FRC mixing and casting procedure.

Many national level structural design recommendations have been published in Europe as well as in Japan, USA and elsewhere, however, having only these recommendations in hand, the structural design engineer is often not convinced that FRC element can be a reliable structural solution. In fact, due to the high scatter usually observed in bending, tensile and similar tests, the most of the currently available design recommendations are based on inverse modelling approach. This means that the strength properties of FRC are determined by performing a standard test, approximating the experimental curves with simple linear or multi-linear relations and by evaluating several safety factors, the strength of FRC is calculated from the approximated curves.

It has to be highlighted that behaviour of FRC element is strictly dependant on the fraction of fibers and completely different type of behaviour such as strain-softening or strain-hardening may be observed if the fiber fraction is low or high respectively. This means that the same approximation routine may not be applicable for different types of FRC. Therefore terms such as high performance fiber reinforced concrete (HPFRC) and ultra high performance fiber reinforced concrete (UHPFRC) have been recently defined in order to highlight the differences in behaviour as compared to “conventional” FRC.

On the other hand, the developers of structural design regulations for FRC, HPFRC and UHPFRC have clearly stated that similar calculation approaches have to be employed for all mentioned types of fiber reinforced concrete in order to provide the structural designer with easy-to-use document for structural design [1]. Even the analogy with existing design regulations for conventional reinforced concrete, which is completely different in general principles, is being considered for the sake of designer's convenience [1].

The direct modelling approaches for characterizing the performance of FRC structural elements have also been applied and investigated in the literature, however, the disadvantage is that direct modelling procedure is generally more complex and large amount of input parameters must be known prior to modelling. Validation tests are still considered essential even when using the direct modelling due to the previously described typical large scatter associated with non-uniform fiber orientation and distribution.

Although seemingly more complex and probably therefore less studied in the literature than the inverse approach, the direct modelling approach still possesses high potential to become an efficient tool for predicting behaviour of FRC structural elements. In fact, if the fiber volume fraction, type, orientation and distribution would be known, the prediction of behaviour of FRC structural element would be straightforward, since it is commonly agreed and recognized in numerous literature studies that the load bearing capacity and performance of the FRC element is related to pull-out resistance of fibers. Thus, the understanding of the fiber pull-out mechanism is crucial for development of a model using the direct approach. Given the random distribution of fibers in the volume of FRC element, it is essential to evaluate the effects of fiber orientation angle and embedded length on fiber's pull-out resistance. There are several types of fibers that are currently available commercially and evaluating the pull-out resistance and the effect of fiber orientation and embedded length for each type of fiber is a tedious, however, not impossible task.

The objective of this Dissertation Thesis is to elaborate a model for prediction of load bearing capacity and post-cracking behaviour of steel fiber reinforced concrete structural elements using direct modelling approach.

In order to achieve the formulated objective the following tasks of the study are outlined:

1. To determine experimentally the pull-out resistance of different types of commercially available steel fibers. Also to evaluate in the experimental study is the dependance of fiber pull-out resistance on fiber embedded length and inclination angle.

2. To perform numerical modelling of fiber pull-out process and to evaluate the significance of geometrical and mechanical parameters that affect the pull-out resistance of the fiber.

3. To elaborate the algorithm of the model for predicting the load bearing capacity and post-cracking behaviour of FRC structural elements subjected to bending loads.

The first task (described in Chapter 3) – experimental measurements of fiber pull-out resistance is performed using a specifically elaborated pull-out test procedure. Moulds for pull-out specimens were designed and manufactured in order to fulfill the requirements of the study, i.e., to investigate different fiber embedded lengths as well as different inclination angles. For this reason 66 different configurations of samples were manufactured. Testing grips accurately corresponding with the shape of the moulded specimens were also manufactured in order to perform the pull-out tests in the tensile machine. Zwick/Roell testing machine was used in combination with videoextensometer for measuring the pull-out displacement. At least 9 specimens were manufactured for each configuration resulting in total number of tested specimens equal to 594 pieces. The pull-out test results were processed using Microsoft Excel software. The experimentally measured pull-out load – displacement relations were averaged between specimens to obtain the average pull-out law for each configuration of fiber embedded length and inclination.

The second task (described in Chapter 4) – numerical modelling of fiber pull-out process was performed for straight shape and aligned fibers. Finite element method (FEM) software ANSYS was used for modelling. The objective of numerical modelling was to evaluate significance on fiber pull-out resistance of different parameters, which are often difficult to measure experimentally. First a 2-D FEM model was elaborated to analyze the propagation of fiber/matrix interface debond crack using fracture mechanics principles and calculating the energy release rate. Parametric analysis was performed in order to evaluate influence of individual parameters on growth of the interface debond crack. Further, a 3-D FEM model was elaborated in order to study the complete pull-out process and the significance of different parameters was analyzed.

Finally, the third task (described in Chapter 5) was performed using results from previous chapters in order to develop a model for prediction of load bearing capacity and post-cracking behaviour of FRC structural elements. FRC structural elements subjected to bending loads were studied. MATLAB software was used and a code for calculating the applied load – crack

opening displacment relation was written. Laboratory samples were manufactured to validate the modelling results with experimental test results.

In this Dissertation Thesis modelling of load bearing capacity and post-cracking behaviour of fiber reinforced concrete structural elements was performed using the direct modelling approach. Direct modelling has not been favoured in many previous studies due to its complexity. The direct modelling approach used in this Thesis, however, has the advantage over inverse models available in literature with its ability to take into account the actual volume fraction and type of fibers in FRC. And on contrary to direct models published in the literature, relative simplicity and ease of use is maintained in the model proposed in this Dissertation Thesis.

The requirement for modelling simplicity is the availability of fiber pull-out laws. Importance of fiber pull-out laws can be explained judging from the good agreement obtained between modelling and experimental validation test results. Thus the concept of assuming that the load bearing capacity of FRC structural element depends on fiber pull-out resistance is justified. Although there have been many studies in literature focusing on pull-out load-displacement relations of several types of fibers, a broad database of fiber pull-out laws for different fiber embedded lengths and inclination angles has not been available. It is significant to study the effect of fiber embedded length and inclination angle considering that the fibers are usually randomly oriented in FRC. In this study 3 most common types of commercially available steel fibers have been studied obtaining a database for 66 different configurations.

In Chapter 4 of this Dissertation Thesis numerical modelling was performed using latest versions of FEM software programs. For quasi-static loading the debonding of steel fiber/concrete matrix interface could be of too small time scale to be of practical interest (due to weak strength of the interface) therefore not many studies have been done on this subject. However, regarding to constant improvement of mix design of FRC, and increase of interface strength, the analysis of debond crack growth is significant. A 2-D axisymmetrical model was elaborated, which in combination with fracture mechanics concepts was used to calculate the rate of debond crack growth. Further in Chapter 4 a 3-D model was elaborated to model the complete pull-out of fiber. The novelty of 3-D model could be best described by its ability to take into account the shrinkage stresses and to include or neglect the interface strength.

Experimental validation of the proposed model for load bearing capacity of FRC structural elements was performed for FRC beams with reinforcement weight fractions up to 300 $kg/m^3$. This study thus can be highlighted as one of the few studies in literature focusing on such large fiber fractions in FRC.

At this point the use of FRC in many structural applications is significantly hindered due to lack of consistent structural design regulations. Since most of the currently available design recommendations use the inverse modelling approach performing approximations of standard experimental test results, the structural design of FRC can be considered as the adaption to available properties of experimentally tested material. The ability to perform the opposite, i.e., to determine the necessary mix design of FRC in order to suit for the given load and service conditions, is not attainable using the currently available structural design documents.

The model proposed in this Dissertation Thesis, on the other hand, provides the opportunity to predict the load bearing capacity and post-cracking behaviour of FRC structural elements with reasonable degree of complexity. Since the pull-out laws of individual fibers are used as an input data in the proposed model, the structural designer is provided with the ability to calculate the necesary volume fraction and type of steel fibers to fulfill specific requirements of loading and service. This means that more optimized and economical design of FRC is possible using this model, which could be of high economical significance.

Large fiber fractions are essential for structural applications of FRC, however, in such case it is difficult to maintain workability of concrete mix and achieve uniform fiber distribution. In the four years of the doctoral studies a know-how was obtained for the mix design of FRC by testing over 100 different fiber and other concrete ingredient combinations. The mix design presented in this Dissertation Thesis has been selected as one of the best for application in civil engineering for its ability to maintain workability even at high fiber fractions.

The experimental pull-out tests performed as a part of this Dissertation Thesis provides large amount of useful information for development of similar models and for more detailed analysis of fiber shape for the manufacturers of fibers.

The use of numerical FEM models demonstrated in this Dissertation Thesis can also be considered as useful for practical application. The good agreement between numerical modelling and experimental pull-out results actually shows that these models can be used by structural designer, materials selector of materials scientist to evaluate the pull-out behaviour of the fiber and how the pull-out resistance depends on different parameters and properties of concrete matrix.

Results presented for defence of this Dissertation Thesis are:

– Model for prediction of load bearing capacity and post-cracking behaviour of FRC structural elements.

– Experimentally determined pull-out relations of three types of commercially available steel fibers with different embedded lengths and inclination angles.

– Numerical (FEM) models for modelling of fiber/matrix interface debond growth and complete fiber pull-out process.

# 1. LITERATURE REVIEW

## 1.1. State of the art and recent developments

During the past 20 years, the use and applications of fiber reinforced concrete (FRC) and high performance fiber reinforced concrete (HPFRC) have significantly expanded. It has been widely regarded and considered as highly potential building material for future applications in both new structures and in reconstruction projects. The most typical applications of FRC are tunnelling (sprayed or precast as shown in Fig.1.1), industrial floors, precast piles, bridge decks, pavements, airport runways, shell and thin wall structures, etc.

Fig.1.1. Tunnel linings in London metro built from precast FRC panels

Dispersed reinforcement of concrete in form of short steel fibers can be used as the only reinforcement, for example, in industrial floors, pavements, ground supported plates, etc, while in structural elements such as beams, slab plates, columns and similar structures, where high tensile stresses occur, the fiber reinforcement alone is not sufficient, however, fibers can still be used to significantly reduce the amount of necessary continuous reinforcement thus allowing to obtain economical solutions.

The use of FRC as compared with conventional reinforced concrete with continuous reinforcement rods is usually considered beneficial for such reasons as ability to add reinforcement in the concrete mix and cast structures directly. Significant cost savings can be achieved regarding the amount of time and labour power needed for mounting traditional type of reinforcement (in form of continuous steel rods). In tunnel building industry, for example, the application of FRC has resulted in development of special casting technologies that allow

obtaining pre-stressed FRC tunnel walls significantly reducing the consumption of materials [2].

The use of FRC in sophisticated shape structural joints is also a very efficient solution compared to the effort of manually installing the reinforcement rods in places where it is often difficult to reach. Thus the use of FRC can be associated with more freedom in architectural sense, allowing obtaining reasonable structural solutions, which have been difficult before. Sleek, sophisticated structures such as paraboloid shape roofs are probably the best examples to illustrate the aesthetical advantages FRC can offer (see Fig.1.2).

Fig.1.2. Oceanographic museum in Valencia with FRC shell roof

Conventional reinforced concrete structures often suffer from wear and fatigue which leads to spalling of the concrete protective layer exposing the reinforcement to environment (see Fig.1.3). The lifetime of conventional reinforced concrete structures is significantly reduced if the reinforcement is not sufficiently protected. Repair of such structures with plain concrete cannot be considered as a long-term solution, while replacement of the whole damaged structure is also often not reasonable. Repairing of the damaged zones with FRC, however, can be a very efficient solution that not only repairs the structure and protects the reinforcement, but also provides better resistance to further wear and other types of loads. In fact, repair of the existing reinforced concrete structures is believed to be one of the major application areas for FRC [1].

The use of disperse fiber reinforcement in combination with conventional reinforcement is of high interest also from point of view of better crack width control (limitation). When used in small fractions the short fibers may not improve the load bearing capacity of a structural element, however, the crack width control can be significantly improved. One of the best examples of using conventional reinforcement bars in combination with disperse fiber

reinforcement are precast piles. While reinforcement bars bear the high tensile and bending loads, the fibers are an efficient reinforcement at the top head of the pile preventing the spalling of concrete matrix while subjected to dynamic loads during hammering.

Fig.1.3. Typical reinforced concrete pavement slab damaged by wear

Due to its high toughness, durability, abrasion and blast resistance, high interest in FRC from different military establishments is common.

At present, ambitious efforts among European and other FRC scientists and structural engineers world wide are aimed towards elaborating design regulations for both FRC and HPFRC. The two materials (FRC and HPFRC) in fact can be significantly different in their behaviour and therefore nowadays they are strictly separated in the ongoing research [1]. The development from normal strength plain concrete to high performance (strength) plain concrete took approximately 10 years. The same can be addressed towards development from FRC to HPFRC. Besides mix design and strength parameter issues, in case of HPFRC the engineers and scientists had to face other important problems including workability of fresh HPFRC mix which as described earlier is closely related to usage of different additives, plasticizers and superplasticizers.

The most common type of fibers used in FRC and HPFRC is steel fibers. It is due to the lower price of fiber as well as easier workability of FRC mix compared to glass, carbon or aramid fiber reinforced concrete mixes [2].

It must be mentioned that FRC is basically a short fiber ceramic matrix composite with randomly oriented fibers. Despite the ongoing development and significant increase of its properties, FRC still cannot be considered as a full replacement for conventional reinforced

concrete (where reinforcement is in form of continuous, aligned steel rods) in structural applications.

Orientation of fibers in FRC depends on many factors, such as fiber type and amount, mixing, compacting, casting methods, etc. The control of fiber orientation in FRC is a difficult challenge. For example, distinct edge effects are usually observed near the mould faces [2,3]. Fiber orientation can also be significantly dependant on casting and compaction procedure of FRC mix. It has been proved that fibers tend to align with the direction of the flow of concrete. Using vibration compacting as in case of conventional reinforced concrete is often not applicable for FRC since it can cause sinking of fibers [4]. And since vibration compaction is not desirable, the use of self-compacting concrete in FRC is widespread [4,5].

Although reinforcing concrete with continuous fibers (long fibers) would be much more effective, it has to be regarded that adding reinforcement straight in to fresh concrete mix together with the rest of ingredients is ultimately much more convenient and beneficial by saving much time and labour [6-9].

The ability to cast structures with sophisticated geometry, complex joints in one step should also be considered as a major benefit [10].

When subjected to overload, FRC or HPFRC structures will have cracks developing in their weakest sections. The density and size of cracks depend on the amount of fibers as well as on fiber type and the character of the applied load. The fibers have the ability to arrest (by bridging) the crack development and crack opening displacement by transporting stresses along the crack surfaces. Thus, when FRC or HPFRC structures are subjected to bending, a quasi-plastic behaviour is usually characteristic [2].

In general FRC provides more distributed crack development compared to reinforced concrete structures that will have cracks with relatively large opening displacements.

The strain to failure for FRC can be as much as 10 times higher than for traditional reinforced concrete structures. The ability to absorb energy is also higher for FRC compared to reinforced concrete by the same order of magnitude [2].

When the load applied to FRC structural element is extensively increased, the matrix cracks appear, the stress concentration is provoked in crack vicinity and fiber pull-out process can be the further scenario. In general, the behaviour of FRC structural element in the post-cracking stage is stricly dependant on the ability of fibers to resist the pull-out loads [6,7,10-13].

In the initial stage of elastic deformations, the response of SFRC can be considered the same as for the plain concrete matrix – due to the fact that the amount of fibers that provides

reasonable workability of the mix is rather small (approximately 2% of volume), the influence of steel fibers to the increase of elastic modulus of FRC is negligible.

Nevertheless, fibers significantly change properties of concrete mix (workability, shrinkage, early strength, etc.). Adding short steel fibers to the concrete mix has been proved to decrease the magnitude of shrinkage and to prevent formation of shrinkage induced cracks [14]. However, it has to be recognized that generally a higher amount of fibres added to the concrete mix will decrease its workability.

It is known that the more efficient contribution to strength increase in FRC can be expected from fibers with higher aspect ratio (ratio between fiber length and diameter). On the other hand, longer fibers are harder to distribute in volume of the fresh mix and the workability decreases significantly. Therefore, in many cases, a compromise has to be found between fiber aspect ratio and reasonable workability of the mix. The most common types of steel fibers used commercially in FRC have aspect ratios within limits from 50 to 100. Use of longer fibers can cause formation of fiber clusters – spherical shapes consisting of assembled fibers with often dry, unmixed ingredients in the middle. Certainly, formation of such clusters is highly undesirable, but often these clusters can not be noticed before hardening of FRC especially if large volume of FRC mix is used [2]. Therefore care should be taken with the mixing procedure of FRC when fibers are relatively long (>50 mm) and when fiber amount is high.

The force that is necessary to apply to start fiber pull-out depends on the shear strength of the interface between fiber and matrix, the angle of orientation with respect to the applied load, embedded length of the fiber, etc.

It would be preferable that fiber and matrix interface has higher strength, since weak interface allows pull-out and thus insufficient use of the strength potential of steel. It is therefore a common practice that the surfaces of fibers are mechanically and chemically treated before mixing them in the concrete. Since in general, steel fibers and concrete matrix do not provide a high interface strength between them, fiber pull-out is in most cases the typical scenario. The pull-out load can be significantly increased if shaped steel fibers are used – undulated form fibers or fibers with end hooks are very common among the commercially used steel fibers.

The pull-out load increases due to additional amount of work that is necessary to straighten the fibers during the pull-out process. Although, when using fibers with shapes such as hooked-end or undulated, the first cracks can appear at the same load levels as for ordinary straight steel fibers, the crack arresting capacity is many times higher in the first two

cases. The strength of the FRC reinforced with undulated or hooked-end fibers in post-cracking stage is therefore also much higher. The principle of different shapes of fibers to enhance their pull-out resistance actually comes from naturally occurring composites.

Also some unusual shapes of fibers have been studied such as, for example, ring type fibers [15]. Such fiber types are easy to mix within the concrete, however, they are not widely commercially available and the pull-out of fiber is often overtaken by fracture of fibers which is not desirable from point of view of providing ductile behaviour of FRC structures.

During the time when superplasticizers were not commercially available, some research work concerning FRC with high fiber volume fractions lead to interesting developments of material and technological methods. Probably the best example from those research activities is SIFCON (slurry infiltrated fibre concrete) – its production consists of stacking of fibers in mould in close arrangements and then infiltrating it with highly liquid cement paste [16]. The volume percent of fibers for SIFCON can thus reach up to 12-13%, which is remarkable compared to traditionally mixed FRC.

As a result of high fiber volume content, the post cracking strength of 120 – 140 MPa can be achieved. The strain to ultimate failure for SIFCON is also remarkable – up to 10 – 15% of strain. Certainly the cost efficiency of such material is questionable – the overall cost can be very high. The fiber alignment is also subject to variation, which results to rather large scatter in results due to local fiber misalignments and concrete matrix rich regions.

One very similar material developed at the same time was SIMCON (slurry infiltrated mat concrete) [17]. The use of it like in the case of SIFCON is not that common due to its high cost and difficulties in manufacturing routine.

The mix design of HPFRC is very much different to that of FRC. Usually, high performance (strength) limit is assumed to be 150 MPa in compression. The corresponding tensile strength then is usually 8 MPa. HPFRC typically contains very high fractions of cement, microsilica and other additives and plasticizers. The water – cement ratio is usually below 0.2. Fiber volume fraction is usually around 2%. The high amounts of microsilica and similar fine size ingredients has an increasing effect on the hydration reaction rate. Microsilica not only participates in the cement paste hydration reaction but also plays the role of extremely fine particle thus increasing compressive strength [18]. Adding fine size ingredients such as microsilica, silica fume, fly ash or similar leads to more homogeneous concrete properties and decreased porosity [19].

For normal strength concrete the final compressive strength develops in around 3 years time. For high strength concrete, however, the final compressive strength can develop in only 90 days time [18].

Another parameter that can be used to highlight the benefits of high strength concrete for use in FRC is the early strength. It is much higher for high strength concrete and thus the overall rate of structural casting can be notably increased. More than 3 times higher strength has been reported in literature for high strength concrete. The development of cracks during hydration reaction while the structural element is in the mould is therefore also smaller for high strength concrete [18].

Nevertheless, optimization of mix design and the technological development concerning mixing, casting and pumping the fresh concrete mix have led to HPFRC with typically more than 200 MPa compressive strength and fiber volume fractions up to 2.5% (175 kg/m$^3$ and more) while maintaining the workability of the mix.

Fig.1.4. FRC Pavement in Cordoba (Spain). Figure from [20]

In order to produce HPFRC it is first necessary that the strength of the plain concrete matrix is high. For these reasons, usually, the particle size of the ingredients does not exceed 2 mm. Furthermore, the particles must be well sized to form compact form of packing. The water – cement ratio, as mentioned before, is also required to be as small as possible (usually below 0.2). To achieve such water-cement ratios, a wide range of superplasticizers is used.

The strength properties of the fibers are also important. High strength (and high modulus) steel fibers are usually used as reinforcement in HPFRC. Depending on the type of structure, fiber reinforcement can fully or partly replace the conventional reinforcement of steel bars. The best example of full replacement of conventional reinforced structures by FRC is

industrial floors. Application of FRC and HPFRC in floors, pavements and tunnel linings has become a wide practice in commercial building and the mentioned applications are already considered as „traditional“ in the field [20]. Fig.1.4. shows a FRC pavement in military base in Cordoba (Spain).

Partial replacement of continuous reinforcement with fiber reinforcement has become a major application area of FRC and HPFRC in the recent years. There are several very popular examples of applications in reconstruction projects and in new projects, where FRC and HPFRC are used in combination with reinforced concrete structures (e.g., Kassel bridge in Germany (see Fig.1.5) and Kaag bridges in the Netherlands).

Fig.1.5. Pedestrian bridge in Kassel (Germany) built from HPFRC supported on a 3-D steel truss

There are several important reconstruction projects realized with HPFRC also in Switzerland [21]. And not only in Europe – in Japan there have been several major projects on repairing dams, water canals and refractory walls by spraying on a layer of HPFRC [22].

It was already back in 1991, when first research on hybrid concrete structures consisting of traditional and fiber reinforcement have been proved reasonable and beneficial [23].

Although it is self-recognized that development of FRC and HPFRC application has been rather slow in Australia, there are some exceptional applications such as Shepherd’s Gully bridge opened in 2005, which was one of the first highway bridges in the world, where shear and impact resistance reinforcement was fully replaced by steel fibers [24]. There are several more applications reported in [24] such as repairing walls of power plants and similar.

There are some specific structural applications for which the use of FRC and HPFRC can be highly beneficial. As an example, the shell piles, which almost always suffer from compressive stresses and are prone to spalling (small peaces of concrete matrix are breaking

off) due to dynamic loads or high levels of pre-stress in longitudinal steel bar reinforcement. Use of FRC or HPFRC fully eliminates these problems and now such piles can be placed without causing initial damage in them while mounting [1]. When using FRC or HPFRC in combination with conventional reinforcement, the volume of concrete can be significantly saved due to possibility of thin reinforcement protective layers, which are required for conventional reinforced concrete to prevent corrosion and degradation of reinforcement. FRC and HPFRC can supply the same corrosion protection with smaller thickness due to capability of micro-crack arresting.

It is recognized that reduced volume of the structural material leads to consequent benefits such as easier transport, quicker assembly options and longer service life [1].

It is characteristic for HPFRC structures that both high load bearing capacity and control of the crack width is maintained. And unlike conventional reinforced concrete structures, FRC and HPFRC structures can expose multiple micro-cracks instead of having one major crack [22].

Regarding the high interest and demand of FRC from the industry there have been many doctoral thesis dedicated to various investigation subjects. General issues such as mix design and technology, mechanical behaviour and structural design [25-29], shrinkage cracking [30] have been studied in detail. Due to demand for structural design regulations, the more recently published thesis [27,29] are more design oriented than the previously elaborated works.

The amount of available textbooks has also significantly increased recently [2, 31-33].

## 1.2. Micromechanical analysis of FRC

By micromechanical analysis in the present work it is meant that fiber diameter scale is being observed.

Micromechanics of FRC and HPFRC have been widely discussed in many scientific publications over the last decades. The increased interest from building industry has resulted in funding of many projects dealing with the micromechanics since it is considered as a key to characterization and behaviour prediction of this material.

The main obstacle that has prevented developing simple models of behaviour and mechanical properties prediction is heterogeneity of FRC. The properties of FRC will vary moving from one point to another in the casted volume depending on number of fibers, efficient length, fiber orientation, etc. Fiber orientation in turn depends on the casting or

spraying technique used and can be significantly different even if same casting routine is used repeatedly.

An important requirement for micromechanical modelling of FRC properties is that the concrete matrix itself could be considered as a homogeneous isotropic material. In order to achieve it, all the coarse aggregates should be avoided in the mix design [34].

The characteristic compressive strength of such plain concrete matrix usually exceeds 150 MPa with tensile strength reaching up to 10 MPa. Assuming that the concrete matrix is homogeneous, micromechanical models have been developed to predict mechanical properties of FRC and HPFRC. For example, a model has been presented which allows prediction of tensile behaviour of HPFRC depending on the amount of fibers, aspect ratio of fibers, fiber distribution and orientation [35]. Models for tensile behaviour of HPFRC in post-cracking stage have also been presented [36].

It has been concluded that higher amount (volume fraction) of fibers leads to higher degree of scatter in obtained experimental results. Nevertheless, the elastic modulus and tensile strength increases with the volume fraction of fibers in concrete. The same can be related to increase of strain to failure leading towards more ductile than brittle behaviour.

Due to the fact that behaviour of FRC and HPFRC in the post-cracking state is related to multiple fiber pull-out, many micro-mechanical models have been developed for analyzing single fiber pull-out from the concrete matrix. Pull-out tests of single steel fiber from concrete matrix has been widely used to characterize the efficiency and performance of fibers in FRC. Tests performed in [3,37-41] are worth mentioning. Not only different fiber shapes and concrete matrices have been analyzed but also the loading rate and dynamic effects of fiber pull-out.

Both analytical and numerical models for characterization of fiber pull-out resistance have been recently developed [6,42-44].

Commercially available steel fibers have been widely studied regarding their pull-out resistance and embedded length [45]. As it is concluded, the pull-out behaviour of single steel fiber is not only dependent on fiber shape or diameter, but also from properties of concrete matrix [45].

The orientation of fiber with the respect to applied pull-out load is also important. Therefore experimental studies observing behaviour of inclined single steel fibers have been performed [46]. Many different inclination angles have been studied regarding the random orientation of steel fibers in FRC.

Similar fiber pull-out studies have been performed earlier, where it was concluded that the maximum pull-out load is not much different from straight fiber pull-out load [47-49], however, the energy absorbed during the pull-out process was found to be very dependant on the inclination angle. Some research has been done in order to find the optimal angle, which would provide highest amount of absorbed energy during the pull-out process.

Unlike for straight fibers, where only interface shear stresses have to be overcome in order for pull-out to start, for inclined steel fibers additional amount of energy has to be consumed in order to straighten and bend the fiber during the pull-out process. Very often, pull-out of inclined, non-straight fibers is accompanied by spalling of the concrete matrix due to stress concentration. Non-uniform and local friction is another of the obstacles associated with inclined fiber pull-out process [46].

Interesting and comprehensive numerical modelling of a hooked-end steel fiber has been presented in [44]. A state of the art finite element codes are nowadays incorporated to account for nonlinearities of the shaped fiber pull-out process such as interface debonding, non-uniform friction and plasticity of fiber and concrete matrix in a single model [44].

Rather recently an analytical model was presented in [9] concerning pull-out of inclined fiber based on material strength theories. Many of the earlier mentioned micro-mechanisms were evaluated in the model [9], however, the presented model is self-predictive since it is based on many empirical parameters which are not known unless some experimental results are available. A systematic parametric analysis has been performed in rather few studies, for example, in [46].

Without doubt, as concluded in all mentioned papers, the interface shear strength has a key role on the pull-out resistance of fiber. Therefore many of the future work plans are aimed towards increasing the adhesion between the steel fiber and concrete matrix.

Another alternative approach to increase fiber pull-out resistance is to use multiple size fiber mix in the concrete. It is often referred to as „fiber cocktail“ when different length fibers are used at once providing with multi-scale crack arresting capability. Several authors have reported effectiveness of such reinforcement as compared with the same weight fraction of just one type of fibers [4,5,50].

## 1.3. Macro-mechanical analysis of FRC

Several length scales have been referred to in literature concerning the properties and modelling of FRC. The most often terms used are micro-scale, macro-scale, meso-scale, structural scale, etc [1,2]. While micro-scale is often attributed to fiber diameter scale, the

other mentioned terms – macro-scale, meso-scale, structural-scale are not always consistent in the literature. Therefore it has to be defined that within this study macro-mechanical analysis is attributed to the scale of test samples such as beams, cubes plates with cross-section sizes not exceeding 15-20 cm, while the span of beam and plate samples is in the range between 30 – 100 cm. These are actually the dimensions of common laboratory samples.

As the most relevant methods for characterizing the macro-mechanical properties, the load bearing capacity and structural behaviour of FRC bending and tension tests are the most commonly used. Bending tests of SFRC beams are usually performed using 3-point or 4-point bending loading schemes [4,5,51,52]. Usually notched beams are preferable as initiation and development of one dominant crack is facilitated and more controlled and thus more consistent results are obtained. The bending tests of FRC beams without notch are usually associated with higher scatter and more inconsistent results and larger number of samples is necessary for reasonable analysis of results [51]. Certainly, the scatter between bending test results depends not only on the existence of notch, but on the quality of manufacturing (mixing, casting, compacting, etc.). Thus there can be large differences in results between the bending tests performed in laboratory environment or tests performed at the construction site [51-53].

The axial tension tests are usually performed using cylindrical shape samples with a circumferential notch in the middle of sample [53,54].

Fatigue performance of FRC structures has not been widely studied and probably deserves more attention. Only few scientific papers can be mentioned relevant to cyclic pull-out resistance of fibers [38] or performance in cyclic bending of structural beams [55].

The application of FRC in civil engineering has been highly inhibited by the lack of modelling tools and guidelines that would allow reliable prediction of behaviour and characterization of FRC. Therefore the general objective of the macro-mechanical research studies of FRC in literature has mainly been aimed towards derivation of the constitutive laws for FRC structural elements. Several models of constitutive laws have been proposed in literature. Generally, the proposed models can be divided in two groups: inverse and direct methods. The inverse methods are based on performing mechanical tests (bending, tension, etc.) and then fitting the experimentally measured stress-strain ($\sigma - \varepsilon$) or stress-crack width ($\sigma - w$) laws. Direct methods, on the other hand, use input parameters in order to construct $\sigma - \varepsilon$ or $\sigma - w$ relations. Due to large amount of necessary input parameters for the direct methods, they are often regarded as impractical. That is one of the main reasons why most of the proposed methodologies in literature are based on inverse approach.

A comprehensive review of currently proposed constitutive laws and their methodologies has been assembled in recently published doctoral thesis [29].

The simplest models of constitutive laws in form of a stress-strain relation $\sigma - \varepsilon$ were elaborated, for example, in [56], [57] and [58] assuming linear, bi-linear and multi-linear behaviour respectively in order to characterize FRC post-cracking behaviour. Interestingly, that in [56] and [58] the pre cracking behaviour of FRC was considered as independent of presence of fiber reinforcement and only properties of plain concrete were taken into account.

Similar inverse methodology approaches in form of stress-crack width $\sigma - w$ relation have been developed in [59-61] using bi-linear functions and in [62] using exponential function.

In [63] a direct approach methodology was used to derive $\sigma - w$ relation as a constitutive law for FRC. Many behaviour-governing factors such as amount of fibers, fiber pull-out laws as well as orientation and effective length were used in this model. However, as mentioned earlier, the direct approaches require knowledge of many parameters which are not always at hand for an engineer, therefore such methods have not gained popularity due to impracticality. Furthermore, the direct methods proposed in literature are often limited in the range of predictions by being restricted to rather small crack widths $w$.

Macro-mechanical investigations of FRC and HPFRC have been mostly performed analyzing behaviour of beams, plates and shells.

The importance of macro-mechanical analysis of FRC and HPFRC is high since it can be considered as potential basis for developing design regulations. In fact, most of the currently available design recommendations are based on inverse constitutive laws that are recommended to be used in combination with tests, such as beam and plate bending tests, tensile tests, etc.

Macro-mechanical models may also comprise findings and results of micromechanical investigations. In fact, many macro-mechanical research works report that the obtained results were in good agreement with micro-mechanical predictions.

In [64] for example, the averaged and approximate pull-out test curves from [45] were used as an input in a macro-mechanical model for behaviour prediction of FRC and HPFRC beams in bending. In general, the allowable limits of crack opening displacement and load bearing capacity at large crack openings are important tasks for developing design regulations.

There have been several attempts to apply fracture mechanics as a tool to predict the macro-scale crack growth in FRC [65,66]. However, the routine proposed in the papers is

somewhat based on use of experimental coefficients and difficult to incorporate in design regulations.

As shown by many experimental observations, the cracks appear in the most stressed section of the beam and the load bearing capacity of a beam reaches its peak and with the further increase of load, crack starts to open and load bearing capacity decreases as a result of fiber pull-out.

Expected conclusions from various studies of FRC flexural strength tests is that the load bearing capacity of FRC and HPFRC beams is higher if fibers with higher pull-out resistance are used. Usually undulated shape fibers and fibers with different shape end hooks provide high resistance to pull-out loads. The use of „fiber cocktails“ is also supported by many investigations in the literature. The concept of “fiber cocktails” also known as hybrid fiber reinforced concrete is to use several types of steel fibers in the same mix instead of using only one type and length of fibers. A combination of different fiber types and lengths can be found so that a synergistic effect is achieved. The general objective and interest of hybrid FRC is to obtain a composite whose mechanical and physical properties would benefit from contribution of fibers in different length scales. A typical example demonstrating the benefits of hybrid FRC is a composite with multi-scale fiber reinforcement – when the micro-cracks form in the tensile loaded FRC element the small steel fibers are bridging the stress and thus restricting the micro-crack opening, however, when the load is increased, the micro-cracks grow forming the macro-cracks which, in turn, are bridged by larger length scale fibers. As the cracks grow larger, the larger scale fibers are activated to resist the crack growth.

A chapter of recently published PhD thesis has been devoted for investigating this subject in [27] obtaining results in favour of using a hybrid fiber reinforced concrete. Various combinations of fibers and their fractions were analyzed [27] in order to evaluate the usefulness of adding fibers to increasing flexural (bending) strength of a beam.

## 1.4. Design regulations for FRC and HPFRC

Despite its remarkably increasing application in industrial floors, pavements, tunnel linings, the use of both FRC and HPFRC still is limited due to lack of generally accepted design regulations. Possibility of manufacturing the modern, slender and cost-efficient structures from HPFRC described is also limited because of the same reason [1].

Although during the past decades there has been an extensive amount of scientific and on-site research of this material – no easy-to-use structural design documentation have been defined based on the conclusions from these research works. Possible and reasonable

explanation for this particular problem is the presence and influence of many factors such as mix design, mixing technology, fiber type and many other factors that notably affect the final properties of the material.

Despite the lack of generally accepted international design regulations, many national level structural design recommendations have recently been published [67-72].

One of the major drawbacks of most of the currently available design recommendations is the fact that they are based on simplified constitutive relations in form of stress-strain ($\sigma - \varepsilon$) or stress-crack width ($\sigma - w$) laws. A comprehensive review of most European design recommendations has been presented in [29]. As it is well described in the review in [29] simple linear, bilinear or multi-linear relations are proposed for structural design and characterization of FRC.

Regardless of previous efforts, the work on elaborating unified design regulations is still a priority in the researchers and structural engineers community.

Special activity groups have been formed by International concrete federation (FIB) to gather all the necessary information and formulate design regulations for FRC and HPFRC. The new regulations will be designed as an addition to previous regulations CEB-FIP Model Code 90.

As it has been reported in [50], the large amount of research works and information gathered about FRC and HPFRC over the past few years has led to more general understanding of behaviour and properties of the material. Thus, two separate work groups have been formed by FIB to work with FRC and HPFRC respectively. Separated groups are motivated by recent investigations that proved strain-hardening behaviour at post-cracking stage for HPFRC while conventional FRC may typically exhibit strain-softening behaviour [50].

It is clearly recognized that separate design regulation documents have to be formed for FRC and HPFRC. It can as well be written in form of an addition to existing reinforced concrete regulations. Use of existing conventional reinforced concrete design regulations is supported from point of view of easier adaption and understanding for the structural engineers. This might be especially important for hybrid structures where reinforced concrete is used together with short steel fiber reinforcement since it is most likely to be one of the main application areas of FRC and HPFRC [1].

Although two separate work groups have been formed by FIB, it is still recognized that two separate regulations for FRC and HPFRC will most likely lead to many uncertainties – structural designer may not be sure which material (FRC or HPFRC) document to use.

Therefore unified design regulations concerning both FRC and HPFRC are proposed by several authors [1].

While general design regulations for FRC and HPFRC are not yet available, there have been many national level documents and recommendations published in several countries around the world. In the USA, for example, some general design considerations of FRC have been summarized in recommendations [73] and [74]. In Europe, very widely known are the RILEM TC162-TDF design recommendations for simple structures [58] and [75].

As mentioned earlier, similar design recommendations for FRC have also been published in France [67], Sweden [68], Germany [69], Austria [70] and Italy [71].

Recently, design recommendations for FRC structures have also been released in Japan [76]. The general considerations of recommendations [76] which were developed by Japanese Society of Civil Engineers (JSCE) over the past 2 years are well reviewed in [22]. In the Japanese recommendations [76] differences between FRC and HPFRC are recognized. The chapters in [76] include general considerations of structural design, parameters of design, validation and on-site testing of FRC and HPFRC structures [22].

It has to be highlighted that since release of design recommendations [76], there have already been realized several major projects utilizing HPFRC in Japan [77].

As for every structural engineering material, there has to exist a clear and reasonable method to classify different types of FRC and HPFRC. According to the previously mentioned, there is a large variety of different FRC types starting from moderately reinforced up to HPFRC. The mechanical and technological properties of these different types of fiber concretes can be very different. However development of separate and possibly conflicting design regulations for each type of FRC is not desired – rather a unifying design regulations have to be elaborated.

Since it has been previously proved that the usual amounts of fibers in concrete (less than 2% of volume) does not affect the compressive strength – it could be used as a parameter of characterization of matrix – tests of plain concrete cubes in compression are easily performable [50].

Some guidance on manufacturing technology has also be given in the design regulations: a very important part is the manufacturing (mixing, casting) of FRC. It is during manufacturing process, when orientation and distribution of fibers in concrete is set. The more non-uniform production, the higher scatter of results can be expected [1].

It is known that fibers influence the workability of the concrete mix. However, workability classes of plain concrete can still be adapted to characterize FRC as well.

A well-known practice of FRC and HPFRC in applications in civil engineering is for reducing the thickness of protective layer for conventional continuous reinforcement. Furthermore, FRC has the ability to prevent formation of cracks thus preventing corrosion of the main reinforcement. Although, it has been a wide practice to use protective layers made of FRC and HPFRC, the minimum allowed thickness has not yet been clearly defined by the existing recommendations. It should be evaluated taking into account the type of structure, environment, size of the reinforcement and other key parameters [50].

For example, in recommendations [76] published by JSCE it is recognized that the use of FRC and HPFRC in protective layers is beneficial since it is preventing formation of cracks which can serve as a transport of corrosion products which increase the corrosion rate significantly. It is highly important for durability and from point of view of structure lifetime.

It is recognized in the research work groups that the design regulations must contain a description of on-site and laboratory testing methods that are reasonable and provide enough information about material properties for general characterization of the material so that classification of FRC can be performed.

Concerning the tensile properties of FRC and HPFRC it has to be recognized that fibers in concrete contribute to stress transfer only when the micro-cracks have formed. Therefore tensile strength of concrete matrix can also be applied for characterization of FRC and HPFRC. However, as for most ceramic materials the tensile tests are not easy to perform – manufacturing of specimens requires much accuracy and the results will strongly depend on the uniformity or non-uniformity of specimens.

Although, in some of the recommendations small sample tensile tests are suggested, the most common way of on-site and laboratory testing are beam tests in bending loading [50]. In general, a list of parameters should be obtained from these tests in order to classify material and its behaviour in post-cracking stage [50].

It is known that the strength of FRC and HPFRC in the post-cracking stage depends on the crack opening displacement (COD). In general two critical values of COD have to be defined for FRC and HPFRC – one for serviceability limit state and other for the ultimate state.

In fact, in the European standard EN 14651 (2005) there are 4 different values of residual strength in post cracking state $f_{R1}$, $f_{R2}$, $f_{R3}$, $f_{R4}$, which correspond to COD values of 0.5, 1.5, 2.5 un 3.5 mm respectively. According to the mentioned standard, the residual strength and COD is measured for the notched beam specimens. However, only two of the mentioned

residual strength values are used in practice - $f_{R1}$ un $f_{R3}$ for serviceability and ultimate limit states respectively.

To simplify use of the standard the ratio between these two values is introduced as $f_{R1}/f_{R3}$ [50].

According to the mentioned standard, there are several classes defined with the following values of $f_{R1}$: 1.0; 1.5; 2.0; 2.5; 3.0; 4.0; 5.0; 6.0; 7.0; 8.0 (MPa)

Regarding the ratio $f_{R1}/f_{R3}$ the following classes are defined: „a“, if $0.5 \le f_{R1k}/f_{R3k} < 0.8$; „b“ , if $0.8 \le f_{R1k}/f_{R3k} < 1.1$; „c“ , if $1.1 \le f_{R1k}/f_{R3k} < 1.4$; „d“ , if $1.4 \le f_{R1k}/f_{R3k}$.

Such type of classification may as well be applied for HPFRC [50].

Since brittle failure of structures is by any means undesirable, the use of FRC and HPFRC as a full replacement of conventional concrete seems attractive. However according to the standard it can only be allowed if $f_{R1k}/f_{Lk} > 0.4$ and $f_{R3k}/f_{R1k} > 0.5$, where $f_{Lk}$ is the maximum strength of the tested beam in the region when COD is between 0 and 0.05 mm.

In [22], testing methods for tensile strength are presented according to procedures of Japanese recommendations [76].

However, the use of results from one test cannot be straightforward. It has to be recognized that due to the well-known scatter of the test results, several safety factors have to be introduced. Another important parameter to consider is the size of the structure (size factor). The overall distribution and orientation of fibers will strongly depend on the size of the cast structure [50].

It is recognized by the authors working on new design regulations that fiber distribution and orientation are important factors that influence the final strength properties of all types of FRC. However, these factors are hard to control with the existing manufacturing methods and tools available.

Several studies have been using the American standards (ASTM) on FRC slab plate testing [78,79] subjected to bending instead of more popular beam bending tests. According to the typical test results obtained for plates in [78,79], the scatter can be reduced significantly due to formation of three major cracks (forming 120° angle) which are also much longer than cracks in standard beam specimens. Therefore much more volume of the material is “involved” in the crack bridging process and the non-uniform distribution and orientation effects are not as crucial as for beams. Although smaller scatter can be achieved by this

method, it is relevant only for slab or shell structures but not for structural design of beams [50].

In the previously mentioned design recommendations developed by JSCE [76] also the use of synthetic fibers and testing of cast and sprayed structural elements is generally described.

Technological aspects and new technological solutions are very important for development of design regulations for FRC and HPFRC.

In [1] a discussion is presented giving an overview on standard testing of FRC and HPFRC. It is recognized that the current testing methods may give conservative results that may have to be translated to conditions of each specific case of application. At present, several testing methods exist and it is recommended for the designer to apply the testing method that is the closest to the conditions of the structure in question.

Although in studies [78,79] using ASTM for plates have proved to give relatively small scatter, the stress state of the tested plate is very specific and therefore a straightforward linking to rectangular or square slab plates is questionable.

As mentioned earlier, most of the design recommendations are based on the inverse modelling approach, characterizing the performance of FRC by mechanical tests and approximating the obtained results by simple and usually multi-linear relations. As an exception to this approach structural design rules attached to Russian code [72] can be mentioned, since its procedures are presented for calculating the properties of FRC structural elements, using direct approach. For instance, the code addition [72] contains relation to calculate the tensile strength of the structural FRC element

$$R_{fbt} = m_2 R_b \left( K_T \frac{k_{or}^2 \mu_{fv} l_f}{8 \eta_f \cdot d_{f,red}} + 0.08 - 0.5 \cdot \mu_{fv} \right) \tag{1.1}$$

where among other parameters $R_b$ is the tensile strength of the concrete matrix and $\mu_{fv}$ is the fiber volume fraction. The code addition [72] also takes into account the orientation of fibers through coefficient $k_{or}$ and the type of fibers by means of coefficient $\eta_f$ in Eq.(1.1). However, the document [72] is limited in the number of types of fibers and its relevance to higher fiber volume fractions and high performance concrete has to be further investigated.

It has to be emphasized from the previous overview of the proposed design recommendations that similar relations for FRC and HPFRC are often aimed to be unified. On the other hand recent developments have resulted in a significant improvement of mix design and workability, thus allowing to produce concretes with high fiber volume fraction and

resulting in significantly higher bending and tensile strength. Many characteristics of behaviour such as stress-strain ($\sigma-\varepsilon$) or stress-crack width ($\sigma-w$) relation of such high performance material are actually different in principle from conventional FRC with low and moderate fiber contents.

Although it is motivated in progress reports of new design recommendations such as in [1,50] that for the sake of structural engineers convenience the existing recommendations will be used as the basis, the capability of existing multi-linear models may not be sufficient to characterize behaviour of a material which is significantly different in its behaviour.

# 2. OBJECTIVE OF THE STUDY

Following the state of the art description and current problems outlined in the literature review section the following objective is formulated for this study:

To elaborate a model for prediction of load bearing capacity and post-cracking behaviour of steel fiber reinforced concrete structural elements using direct modelling approach.

In order to achieve the formulated objective the following tasks of the study are outlined:

1. To determine experimentally the pull-out resistance of 3 different types of commercially available steel fibers. Also to evaluate in the experimental study is the dependance of fiber pull-out resistance on fiber embedded length and inclination angle.

2. To perform numerical modelling of the fiber pull-out process and to evaluate the significance of geometrical and physical parameters that affect the pull-out resistance of the fiber.

3. To elaborate the algorithm of the model for predicting the load bearing capacity and post-cracking behaviour of steel fiber reinforced concrete structural elements subjected to bending loads.

# 3. EXPERIMENTAL SINGLE FIBER PULL-OUT TESTS

## 3.1. Objective of experimental fiber pull-out tests

There are 3 geometry types of commercially available steel fibers that have been mostly used in FRC: straight, hooked-end and undulated form fibers. While aligned straight fibers in FRC resist the pull-out load only by means of weak interface bonds and residual shrinkage stresses, the hooked-end and undulated fibers are expected to provide much higher resistance to pull-out by means of mechanical anchorage. Mechanisms of pull-out for hooked-end and undulated form fibers are thus much more complicated than for straight fibers and those mechanisms typically involve plastic deformation of the fiber during the process.

Because of these differences between different fibers the load bearing capacity and post-cracking behaviour of FRC structural elements such as beams plates, etc, will be highly dependent on the type and volume fraction of the fibers added to the concrete mix. This study aims to develop a constitutive model alternative to those using the inverse approach and to characterize load bearing capacity and crack opening displacement in a FRC structural element by using the pull-out relations (laws) of individual fibers as the input data. To achieve this a detailed database of experimental pull-out laws is necessary to obtain. Regarding the chaotic orientation and distribution of fibers in FRC the effects of different embedded lengths as well as different orientation angles have to be evaluated. Several studies [25,80] have been published presenting experimental and modelling results for inclined fibers, however, the combined effect of embedded length and inclination angle has not yet been studied.

Therefore, in this chapter experimental pull-out tests have been performed for the three mentioned types of commercially available fibers under various embedded lengths and inclination angles with respect to applied pull-out load. It would have certainly be of great interest to analyze fiber pull-out behaviour in various different types of concrete matrix, however, this study focuses only on investigation of the mentioned fiber alignment parameters. All experimental samples were thus made using the same mix design for the concrete.

## 3.2. Manufacturing of pull-out test samples

The pull-out test samples for this study were manufactured using plywood moulds pictured in Fig.3.3. A better alternative would probably be steel moulds, however the plywood moulds are more cost-efficient if many samples have to be manufactured.

The configuration of the moulded specimen and its dimensions are given in Fig.3.1. In Fig.3.1. $l_f$ shows the embedded length of the fiber (that will be subjected to pull-out) and $\alpha$ shows the inclination angle of the fiber with respect to the applied pull-out load direction.

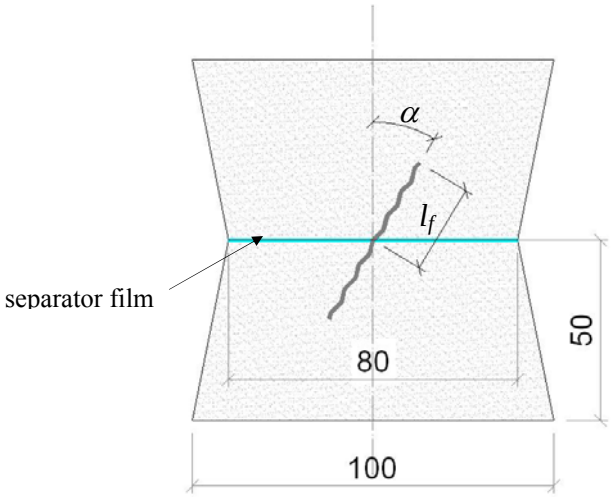


Fig.3.1. Configuration of a pull-out test specimen: $l_f$ - embedded length, $\alpha$ - inclination angle

To prevent concrete samples from sticking to the smooth surfaces of the plywood mould base, a thin layer of oil was applied on the base surface. Furthermore, in order to prevent the transfer of water from concrete through the edges of plywood mould, a thin plastic film was placed along the perimeter of the mould before casting. The same plastic film was used also as a separator between the two halves of the specimen as shown in Fig.3.1. Because of the bad adhesion between the smooth surfaces of the plastic separator film and concrete, it can be practically considered as the initial crack with crack opening $\delta = 0$ at the start of the pull-out experiment. When the tensile load $F_z$ is applied using the tensile testing machine, the embedded fiber is bridging the load from one half of the specimen to another and thus, when the applied displacement increases further, the pull-out of fiber is expected to occur. Certainly, if the pull-out resistance of fiber is high, then the fracture of fiber might occur before or during the process of pull-out depending on the type and alignment of the fiber. According to the configuration of samples shown in Fig.3.1. for symmetrically embedded

fibers it is not possible to control which end of the fiber will have weaker resistance and will therefore pull-out. The lower end of fiber in Fig.3.1. was therefore bent in order to prevent accidental pull-out of the undesired part of the fiber regarding that the mechanical anchorage between steel fiber and concrete matrix provides much larger resistance to pull-out load than the weak interface bonds.

The concrete mix for experimental pull-out test samples was prepared in a conventional concrete mixer shown in Fig.3.2.

Fig.3.2. Mixing of concrete in a conventional concrete mixer

After the concrete mix had reached a homogeneous appearance, the plywood moulds were filled. The mix design of the concrete mix was carefully selected in order to be suitable for such experimental samples. No coarse aggregates were used in order to ensure isotropic material and better interface with the embedded steel fiber. The mix design used for pull-out test specimen preparation in this study is listed in Table 3.1.

During the mould filling procedure first, each mould was half filled with concrete before the embedded length $l_f$ and orientation angle $\alpha$ of fiber were adjusted to desired alignment by hand. Filling the half of the mould prior to aligning the fiber ensured that the fiber in all specimens would be in the same plane. After adjusting the desired length and inclination angle of the fiber, the rest of the mould was filled. It is important to note that adjusting of fiber was performed in the shortest possible time in order to avoid drying of the filled concrete part that could possibly lead to weaker properties similar to weld lines or flow fronts in metallic and polymer materials respectively. Due to embedded fiber, the stress concentration will occur in this plane of the pull-out sample and, if the mould is filled in two steps with long time spent between those steps, the chance of splitting of concrete along the weakened surface and obtaining unrepresentative sample is increased. However, in the

present study the mould filling was performed with short interval for adjusting the fiber and no weakened surfaces were found in the experiments.

After filling the mould completely a soft polyethylene film was placed on the top surface of the specimens to prevent evaporation of water from concrete. After 48 hours of curing in room temperature conditions, the samples were carefully removed from the moulds and placed in a water bath until the age of 28 days was reached. Fiber pull-out experiments were then carried out.

Fig.3.3. Plywood moulds before filling of concrete and a close-up showing plastic insert film with steel fiber

## 3.3. Experimental pull-out test procedure

All single fiber pull-out experiments were carried out using tensile testing machine Zwick/Roell Z150 shown in Fig.3.4. The frame of the machine is capable to resist 150 kN, however, since the maximum pull-out loads were expected to be much smaller the pull-out load was measured by a ±1 kN capacity load cell.

The pull-out displacement, which in the further text will be referred to as $u_z$, was measured using videoextensometer "Messphysik" shown in Fig.3.5. The videoextensometer, being a non-contact measuring device, was particularly suitable for the performed pull-out tests. It has capability of measuring displacement between two reference lines drawn on the sample. Following the recommendations provided in the user's manual of the videoextensometer, a good contrast between the surface of the specimen and the reference line has to be ensured. Therefore, a white (or similar light colour) tape was first glued on each specimen surface and reference lines were drawn on each side of the specimen with a thin permanent marker as depicted in Fig.3.6. Custom-made stainless steel grips were used for the pull-out tests also shown in Fig.3.6.

Fig.3.4. Tensile testing machine Zwick/Roell Z150

.


Fig.3.5. Non-contact videoextensometer Messphysik

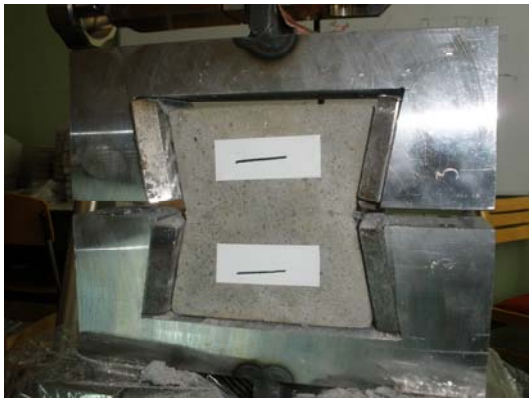

Fig.3.6. A pull-out specimen is mounted in the tensile test machine grips. Reference (measurement) lines drawn on a white tape glued on surface of specimen

As it can be noted, the fixture of the grips is very simple and the joints used with the tensile machine grips were rigid. Although, as it will be discussed further, several drawbacks were realized after completion of the pull-out tests, the presented fixture of the specimen grips was still considered as being suitable for achieving the goals of this study.

During the pull-out test the displacement between the reference lines is measured as shown in Fig.3.7. It is assumed to be equal to the pull-out displacement $u_z$. Prior to running the test, the automatic reference (measurement) line detection was controlled and adjusted if necessary in a computer display using the software connected to the videoextensometer. The displacement data were always synchronized with corresponding load $F_z$ data being read from the load cell.

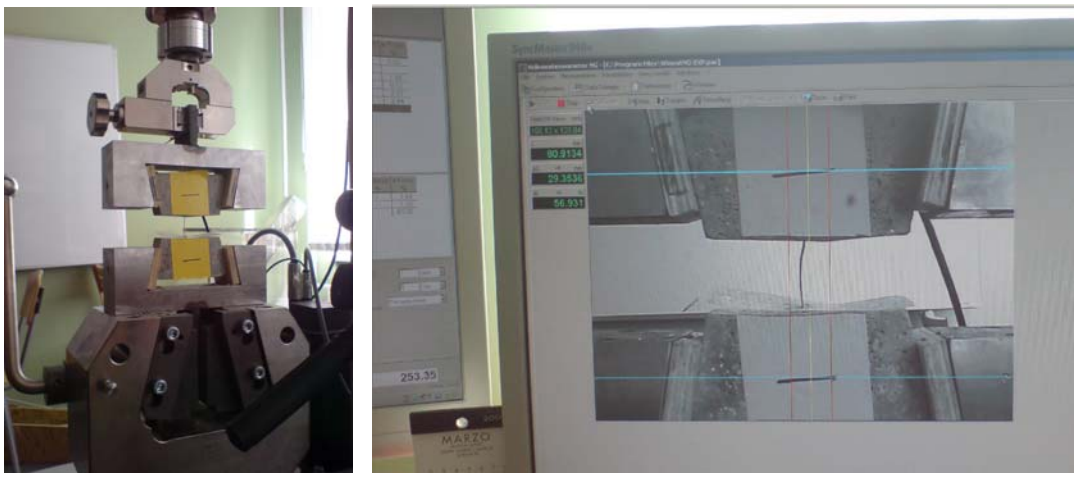

Fig.3.7. Pull-out test experiment: a) specimen in tensile machine grips; b) Display of videoextensometer software during the pull-out test

The test speed for all specimens was set to 10 milimeters per minute. Each test was conducted until complete pull-out of the fiber or seldom the fiber fracture had occurred. After each specimen had been tested, a description of test was written in the specimen test protocol saving valuable information about the quality and representativeness of the specimen and for further reference and guidance on interpretation of test results.

It has to be noted that according to the build-up of the test specimens according to the described procedure a predefined crack exists in each specimen where fiber is the only element bridging the forces across the two parts of it. In some studies [80, 81], a small unit of concrete cross-section was also intentionally bridging the initially applied load before its failure in tension after which only fiber continues to bridge load. In the mentioned studies the

small (reduced) section is aimed to represent fiber spacing in real composite [80,81]. Obviously, it results in initial pull-out response being almost linear until the brittle failure of the concrete section at typically low applied strains. The brittle failure results in instant and often significant drop of load. After the cross-section of concrete has failed, the fiber remains the only load bridging component. The load may then increase or decrease during the pull-out process depending on the type of fiber, embedded length and orientation.

However, in the current research it is assumed that the micro-crack pre-exists, the fiber is initially the only load bridging component and the pull-out of fiber is expected to occur smoothly. This approach is motivated by experimental observations of macro-scale and experiments of FRC beams with high fiber content subjected to bending loads, which is of interest in this study. From the FRC beam tests it was observed that large amount of micro cracks form before a larger macro-scale crack forms from these micro-cracks in the critical cross-section of the beam and hence, the load-deflection curve has the smooth shape with no visible drops of load or similar distortions.

Therefore, before each test, the specimens were inspected to make sure that there is no concrete cross-section that could possibly bridge loads during the pull-out test. The existence of such concrete cross-section can most likely occur when the moulds shown in Fig.3.3. are overfilled so that they exceed the height of the separating plastic film. All specimens with such characteristics were carefully processed (e.g., by removing the undesirable concrete sections) before the test so that the fiber would be the only load-bridging component.

It was already mentioned in the objective of the present study that commercially available steel fibers are of interest. 3 most common types of steel fibers were used in single fiber pull-out experiments: straight fibers, hooked end fibers and undulated shape fibers. The 3 fiber types and their respective geometrical parameters are demonstrated in Fig.3.8.

Hooked end fibers were Bekaert Dramix trademark fibers, undulated shape fibers were Tabix trademark fibers from ArcelorMittal, while the straight fibers were hand cut from 60 mm long Bekaert Dramix trademark hooked-end fibers (the end hooks were cut off). In Fig.3.8. the length of the fibers is specified as $2L_f$ for the reasons of notation convenience in the following experimental fiber pull-out study.

As it is shown in Fig.3.8. the length of fibers is defined as a distance from one fiber end to another and parallel with the fiber longitudinal axis. Straight fiber and hooked-end fiber diameters were equal to $d_f = 0.75$ mm, while undulated shape fibers were a little larger in diameter, i.e., $d_f = 1.0$ mm. This difference in fiber diameters between undulated shape and

other 2 types of fibers was not of primary concern in this work since the objective of this experimental study is to obtain the pull-out laws of these specific fibers. The significance of different geometrical parameters of fiber was analyzed in Chapter 4 of this work, where numerical modelling was performed.

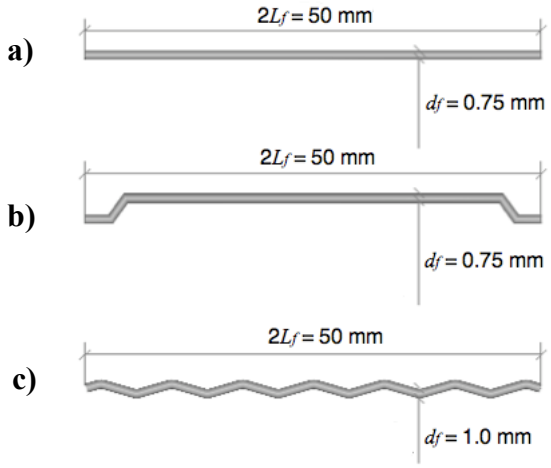


Fig.3.8. common types of commercially available fibers: a) straight; b) hooked-end; c) undulated shape fibers

According to manufacturer's data sheet, the tensile strength for undulated shape fibers is 1100 $N/mm^2$ while for straight and hooked-end fibers the tensile strength is equal to 1160 $N/mm^2$. Elastic modulus of all fiber types corresponds to $E_f = 210$ GPa.

Mix design of the concrete used in the pull-out experiments is given in Table 3.1.

Table 3.1.

Mix design of concrete mix B4

| Nr. | Ingredient | Amount, kg/m$^3$ |
|---|---|---|
| 1 | Cement CEM 42.5 | 539 |
| 2 | Sand (0 – 0.5 mm) | 264 |
| 3 | Sand (0.3 – 2.5 mm) | 1161 |
| 4 | Dolomite | 137 |
| 5 | Micro-silica | 74 |
| 6 | Water | 254 |
| 7 | Plasticizer | 12 |

As presented in Table 3.1 the concrete mix used in this study is a mix consisting of fine aggregates only. According to Table 3.1, the largest size of ingredients was the fraction of

sand 0.3-2.5 mm. The concrete mix in Table 3.1 and in the following is denoted as B4 for the reasons of convenience, since such notation was used in laboratory for labelling the samples.

The water/cement ratio of concrete mix is quite high ($w/c = 0.47$) however, the objective of this study was to investigate the pull-out behaviour of different fibers and not study different properties of concrete matrix.

The strength of the mix was medium – the test results from standard cube compressive tests showed the average strength of 78 MPa. However, the main criterion for the concrete used in this study was not its compressive strength but the good flow-ability and suitable viscosity so that the small moulds could be sufficiently filled and the surface of the single fiber well wetted and embedded.

A list of all test sample configurations in terms of Fig.3.1. is summarized in Table 3.2.

Table 3.2.

Pull-out test sample configuration and notation of samples

| Name | Fiber type | $\alpha$ [°] | $l_f$ [mm] | Name | Fiber type | $\alpha$ [°] | $l_f$ [mm] |
|---|---|---|---|---|---|---|---|
| F1 | straight | 0 | 25 | F34 | straight | 30 | 20 |
| F2 | hooked-end | 0 | 25 | F35 | undulated | 30 | 20 |
| F3 | undulated | 0 | 25 | F36 | hooked-end | 30 | 20 |
| F4 | straight | 0 | 20 | F37 | straight | 45 | 20 |
| F5 | hooked-end | 0 | 20 | F38 | undulated | 45 | 20 |
| F6 | undulated | 0 | 20 | F39 | hooked-end | 45 | 20 |
| F7 | straight | 0 | 15 | F40 | straight | 60 | 20 |
| F8 | hooked-end | 0 | 15 | F41 | undulated | 60 | 20 |
| F9 | undulated | 0 | 15 | F42 | hooked-end | 60 | 20 |
| F10 | straight | 0 | 10 | F43 | straight | 20 | 15 |
| F11 | hooked-end | 0 | 10 | F44 | undulated | 20 | 15 |
| F12 | undulated | 0 | 10 | F45 | hooked-end | 20 | 15 |
| F13 | straight | 0 | 5 | F46 | straight | 30 | 15 |
| F14 | hooked-end | 0 | 5 | F47 | undulated | 30 | 15 |
| F15 | undulated | 0 | 5 | F48 | hooked-end | 30 | 15 |
| F16 | straight | 10 | 25 | F49 | straight | 45 | 15 |
| F17 | hooked-end | 10 | 25 | F50 | undulated | 45 | 15 |
| F18 | undulated | 10 | 25 | F51 | hooked-end | 45 | 15 |
| F19 | straight | 20 | 25 | F52 | straight | 60 | 15 |
| F20 | hooked-end | 20 | 25 | F53 | undulated | 60 | 15 |
| F21 | undulated | 20 | 25 | F54 | hooked-end | 60 | 15 |
| F22 | straight | 30 | 25 | F55 | straight | 20 | 10 |
| F23 | hooked-end | 30 | 25 | F56 | undulated | 20 | 10 |
| F24 | undulated | 30 | 25 | F57 | hooked-end | 20 | 10 |
| F25 | straight | 45 | 25 | F58 | straight | 30 | 10 |
| F26 | hooked-end | 45 | 25 | F59 | undulated | 30 | 10 |
| F27 | undulated | 45 | 25 | F60 | hooked-end | 30 | 10 |
| F28 | straight | 60 | 25 | F61 | straight | 45 | 10 |
| F29 | hooked-end | 60 | 25 | F62 | undulated | 45 | 10 |
| F30 | undulated | 60 | 25 | F63 | hooked-end | 45 | 10 |
| F31 | straight | 20 | 20 | F64 | straight | 60 | 10 |
| F32 | undulated | 20 | 20 | F65 | undulated | 60 | 10 |
| F33 | hooked-end | 20 | 20 | F66 | hooked-end | 60 | 10 |

For each fiber configuration a number of 8 - 9 specimens were manufactured. The number of manufactured specimens for each case was high due to expecting to encounter high scatter in the test results. Since the objective of this study is to employ the experimentally measured pull-out laws in a larger scale model for predicting the load bearing capacity and

post-cracking behaviour of FRC beam, fully representative pull-out relations (laws) are necessary as well as the statistical distribution for these laws.

## 3.4. Pull-out test results and discussion

In the following section experimental pull-out test results are presented and discussed in detail. Only the average curves for each configuration are presented, the statistical distribution of test results is discussed further in this section. During the averaging procedure of the pull-out curves fixed values of displacements were selected starting from $u_z = 0$ mm and incrementing by $\Delta u_z = 0.1$ mm. The average of corresponding values of load $F_z$ was calculated. Unrepresentative samples were excluded from averaging.

First, aligned and symmetrically embedded fiber pull-out curves for the three studied types of fibers are compared. During the manufacturing of the first series of samples some difficulties such as in aligning the fiber, compacting the concrete and sample demoulding were experienced. The necessary skill of manufacturing was obtained based on the errors and imperfections that occurred for the first set of samples. For this reason, unfortunately, the results obtained for samples with symmetrically embedded and aligned fiber F1 (see in Table 3.2) were considered as unrepresentative and had to be excluded from the current study. Thus, the comparison of pull-out curves for the three different fiber types was performed through samples F4, F5 and F6 which, as listed in Table 3.2, all have embedded length equal to $l_f = 20$ mm. The average pull-out curves for samples F4, F5 and F6 are shown in Fig.3.9.

As it can be seen in Fig.3.9., undulated shape steel fibers F6 exhibit the highest pull-out force $F_z$ and the highest pull-out resistance throughout the whole pull-out process. The maximal pull-out load for hooked-end fibers F5 is according to the obtained results approximately 2 times lower than for undulated type fibers F6. Compared to undulated and hooked-end fibers, that provide additional mechanical anchorage with concrete the straight aligned fibers F4 showed the smallest maximal pull-out load values and the smallest resistance throughout the whole process. According to Fig.3.9. the peak load for straight fibers F4 is more than two times smaller than for hooked-end fibers F5. The much higher resistance for undulated and hooked-end fibers is achieved through straightening of the fiber through the channel during the pull-out process. Straightening of fibers is accompanied by significant increase of local fiber and concrete surface friction and for overcoming this resistance higher applied loads are required.

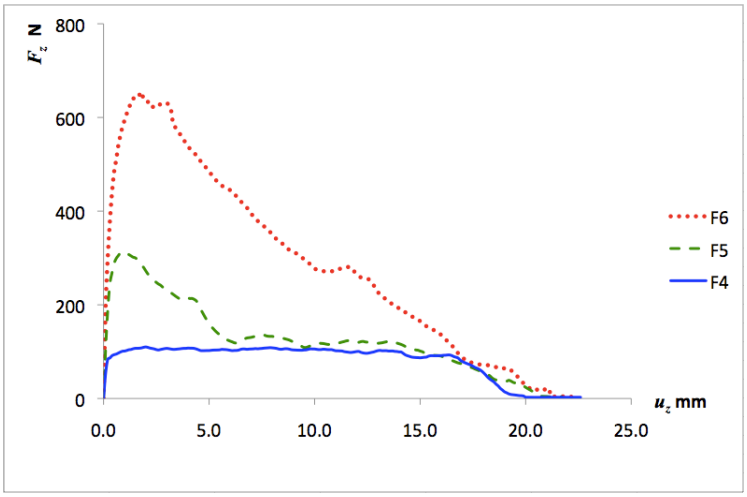


Fig.3.9. Average pull-out curves for three fiber types: F4 – straight; F5 – hooked-end; F6 – undulated. All fibers were aligned with the applied pull-out load

The results in Fig.3.9. generally show the advantage of different shapes of steel fibers that can lead to significant increase of pull-out resistance. However, it is always necessary to remember, that the performance of such fibers depends much on the properties of concrete matrix – in fact, for weak concrete matrices the stress concentration around the shaped fibers may often cause spalling resulting in abrupt, brittle loss of pull-out resistance and straight aligned fibers can actually be better in performance. In this study, as it is seen from Fig.3.9. the strength of the concrete matrix was sufficient to resist those stresses and the potential of mechanical anchoring and fiber straightening has been successfully taken as advantage.

Comparing the undulated and hooked-end fibers it has to be noted that the maximal pull-out load $F_z$ for undulated fibers although is approximately 2 times higher is reached at higher displacement values $u_z$ than the maximal pull-out load for hooked-end fibers. It should be a considerable and important factor to keep in mind when crack width control is of primer interest.

Further, experimental results revealing the influence of fiber embedded length $l_f$ are discussed.

Results for straight fibers are presented in Fig.3.10. showing the pull-out curves for samples F4, F7, F10 and F13 (see Table 3.2).

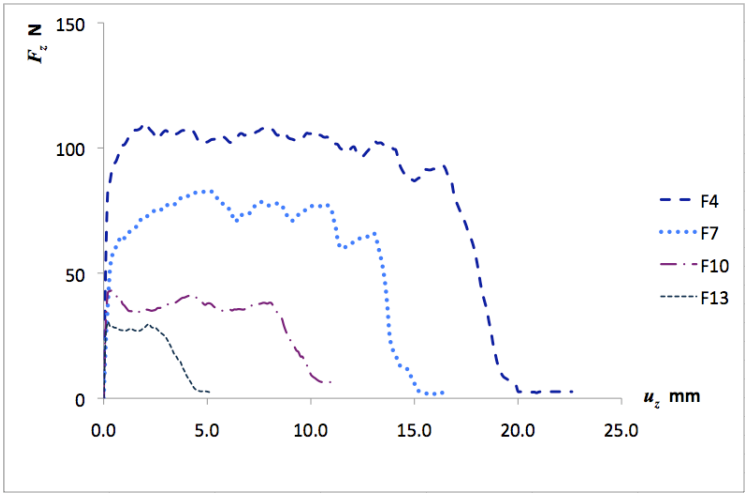


Fig.3.10. Average pull-out curves for straight fibers: F4 ( $l_f = 20$ mm) F7 ($l_f = 15$ mm); F10 ($l_f = 10$ mm); F13 ($l_f = 5$ mm)

As it can be seen from Fig.3.10. for straight fibers the influence of fiber embedded length $l_f$ is significant. The general observation is that the maximal pull-out load is higher for longer embedded lengths and there is a gradual decrease of the maximal pull-out load for the respective shorter embedded lengths. According to the obtained results the maximal pull-out load $F_z$ for straight fibers is reached at relatively small displacements ($u_z$ = 0.2 – 0.5 mm). As it can be seen from the pull-out curves, the force-displacement relation from initial point to maximum load is not linear. Obviously the very initial pull-out response of fiber can be considered as linear but deviation from linear relation starts to occur soon (at $u_z$ approximately 0.1 mm) most probably due to debonding between the steel fiber and concrete matrix interface. When the fiber/matrix interface has been debonded along the whole fiber length the movement (slip) of fiber becomes possible as a result of continuous applied displacement. It has been reported in literature [82] that because of the initial stress-state forming during the concrete shrinkage the radial stresses on the interface remain compressive and the pull-out resistance is provided through friction forces forming along the interface. A constant friction resistance along the whole length of the interface would lead to gradual decrease of the load as the pull-out displacement is increased and the fiber embedded length gradually decreases. However, the results obtained and demonstrated in Fig.3.10. show a rather small decrease of the pull-out load up until the last few millimetres of the length remaining in the concrete matrix when a steep decrease of load occurs concluding the complete pull-out of the fiber. This phenomenon could be explained by an increase in local friction resistance. Increasing friction resistance can be induced by the movement and

compaction of small concrete particles separated during the fiber sliding against the matrix surface. Also, the role of fiber misalignment in some specimens might have been responsible for such a result. Although if the fiber is just a few degrees inclined, it might be enough for local friction to occur (e.g. at the exit point) and the pull-out curve thus can be affected especially regarding that during the manufacturing of specimens fiber orientation angle was set manually with help of a ruler.

However, similar plateau regions can be found from pull-out test results of aligned fibers in literature [80,83] therefore the statement of increase of local friction is more likely to correspond to reality.

What is seen in Fig.3.10. as an oscillating type of character for the pull-out curves after the peak load leads to conclude that the form of the local friction is not stable – the particles are compacted, they provide locally higher friction between fiber/matrix surfaces until it is overcome by higher applied load which distorts the compacted regions. The compaction can thus have multiple occasions in single fiber. Hence, the frictional resistance can locally decrease or increase and it shows in the pull-out curves in Fig.3.10.

However, the oscillations of pull-out load during this stage are not of significant amplitude. Nevertheless, this type of behaviour was observed for all embedded lengths including the shortest $l_f = 5$ mm, as clearly seen in Fig.3.10.

When only last 2-4 mm of fiber embedded length are left to be pulled out, the effects of local friction, misalignment and similar become negligible and the pull-out load thus starts to decrease at a much higher rate (well seen in Fig.3.10. for all observed embedded lengths). The fiber exit point and its region most likely has the highest local friction coefficient and thus it is likely that the concrete matrix channel is damaged and flattened as a result of increased friction and particle removal or small-scale matrix spalling related to this.

In Fig.3.11. average pull-out curves for hooked-end fibers are presented for different embedded lengths. Results for samples F2, F5, F8, F11 and F14 are presented. The most notable difference from pull-out curves of straight fibers is the distinct first peak load (at displacements approximately $u_z = 0.8$ mm on average) after which a sudden decrease of the pull-out load occurs. Generally analyzing the pull-out curves presented in Fig.3.11., an important notification is that the value of this peak load does not depend on the embedded length with the only exception being the smallest embedded length $l_f = 5$ mm. It was mentioned previously in the text that the increase in the maximal pull-out load is due to mechanical anchorage provided by the end hook of the fiber. It can be concluded that as long

as the fiber is embedded with sufficient length ($l_f \geq 10$ mm according to results in Fig.3.11) the pull-out load will not increase with increasing the embedded length. This is important to emphasize this result, for example by imagining that significant amount of fibers can be saved without affecting the behaviour and load bearing capacity of a structural FRC element.

Another conclusion from this is the fact that the interface bond strength in the present system of fibers and concrete matrix is weak and negligible since it is clearly evident in Fig.3.11 that the pull-out resistance for longer fibers which have larger fiber/matrix contact zone does not increase. In fact, even after the peak load the pull-out resistance for the fibers with embedded lengths $l_f \geq 10$ mm is very much similar.

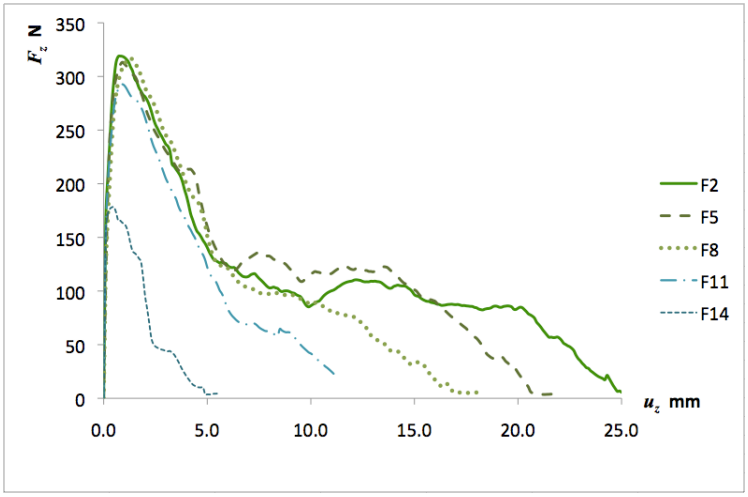


Fig.3.11. Average pull-out curves for hooked-end fibers: F2 ($l_f = 25$ mm); F5 ($l_f = 20$ mm); F8 ($l_f = 15$ mm); F11 ($l_f = 10$ mm); F14 ($l_f = 5$ mm)

There is typically another small recognizable peak on the steep section of curves after the peak load indicating the straightening of the fiber end hook around the 2nd exit as shown in Fig.3.12. The occurrence of this peak has always been reported also in literature, where hooked-end fibers have been tested [80,83].

After the fiber has fully passed the 2nd exit point (see Fig.3.12.) the fiber has generally been straightened. This shows in its further pull-out response as the character of pull-out resistance is very similar to straight fibers (see Fig.3.10.). Similarly to straight fibers, the pull-out response of hooked-end fibers after full straightening can be divided into two parts – one with slow but recognizable decrease of load, where local friction can increase and provide local increase of load, and the final part, where due to very small remaining length of fiber the pull-out load decreases very fast. The physical explanation of this experimental observation

can be based on the same aspects as for the straight fibers – due to increased local friction at the fiber exit point (1st exit in Fig.3.12.) possible flattening or spalling is favoured and can thus lead to decreased resistance when very small length of fiber is remaining.

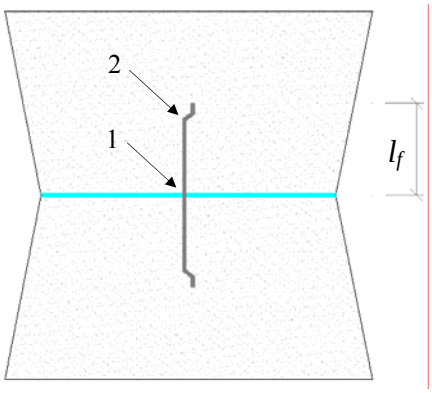


Fig.3.12. Hooked-end fiber pull-out exit points: 1 – at the bridged crack surface; 2 – at the beginning of the hook of the fiber

Generally, the hooked-end fiber pull-out curves show how a small size hook at the end of each fiber, which is not really difficult to achieve during fiber manufacturing, can significantly improve the pull-out resistance with no increase of the material consumption. Since the maximal pull-out load for hooked-end fibers was proved to depend mostly on the mechanical anchorage of fiber, the resulting pull-out curves are more stable and more reliable for predictions. For straight fibers the differences in the bond strength between the test samples can be very high thus resulting in large deviation between pull-out relations. Using hooked-end fibers as reinforcement in FRC beams can in this way also decrease the statistical distribution of, for example, flexural strength.

Pull-out curves for undulated shape fibers are shown in Fig.3.13. Results for samples F3, F6, F9, F12 and F15 are presented.

As it was found earlier from the comparison performed in Fig.3.9., the undulated shape fibers provide the highest pull-out resistance from all three fiber types that were studied. The effect of a single hook at the end of fiber was well demonstrated in previous text and figures and one can imagine the additional resistance that can be achieved if there is more than one hook in the fiber. During the pull-out of undulated fiber straightening and bending of fiber occurs simultaneously several times, depending on the shape and number of the “waves”.

From the results presented in Fig.3.13. it is evident that the highest pull-out load corresponds to highest fiber embedded length, i.e., $l_f = 25$ mm. However, if we consider and compare the pull-out curves for fibers with embedded lengths $l_f = 20$ mm and $l_f = 15$ mm,

the peak pull-out load in both cases is the same. Something similar was observer in the case of hooked-end fibers, where it was proved that in a particular range the maximal pull-out load of fiber depends only on the number of hooks and not on the embedded length. In order to explain the coincidence between maximal loads in samples F6 and F9, we have to analyze the geometrical shape of pull-out specimens and fibers. In Fig.3.14. pull-out configurations corresponding to F3, F6, F9, F12 and F15 have been depicted side-by-side for comparison. The actual geometry of Tabix fibers has been reproduced in the figure.

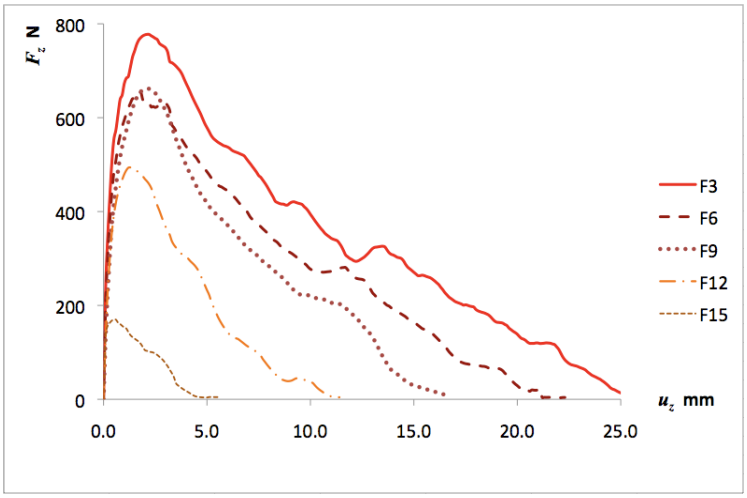


Fig.3.13. Average pull-out curves for undulated fibers: F3 ($l_f = 25$ mm); F6 ($l_f = 20$ mm); F9 ($l_f = 15$ mm); F10 ($l_f = 10$ mm); F15 ($l_f = 5$ mm)

It can be seen in Fig.3.14. that for fiber configuration F3 with embedded length $l_f = 25$ mm the number of embedded hooks can be considered as 3 pieces. Although the total embedded length for fiber configuration F6 is larger than for F9 (20 mm and 15 mm respectively), for both fibers the number of embedded hooks can be concluded being the same, i.e., 2 hooks. Confirmed by experimental results that maximal pull-out loads for these two fiber configurations are very much the same, this leads to conclude, that number of embedded hooks is crucial for pull-out resistance.

Further, continuing analysis of Fig.3.14., we can note that for fiber configuration F12 ($l_f = 10$ mm) the number of embedded hooks is 1 and for fiber configuration F15 ($l_f = 5$ mm) according to Fig.3.14. it has to be considered as 0.5 (only half of the hook is embedded in matrix). Therefore, the corresponding pull-out resistance for configuration F15 is significantly lower than for F12.

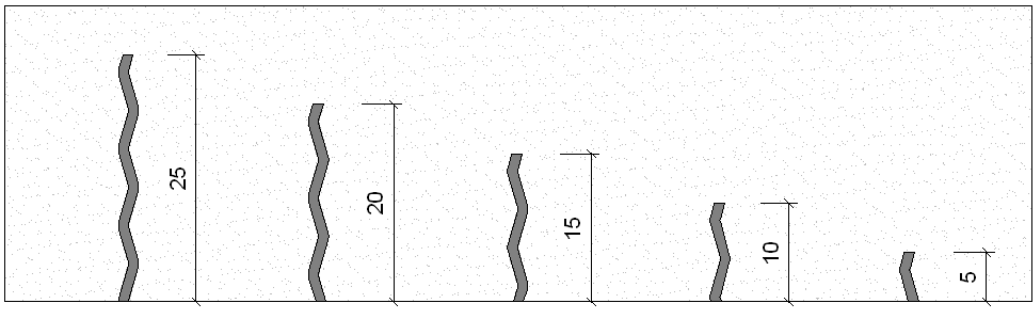


Fig.3.14. Undulated fibers with different embedded lengths $l_f$. Fiber configurations F3, F6, F9, F12 and F15 shown respectively from left to right

Since experiments demonstrate that the pull-out resistance for undulated fibers significantly depends on mechanical adhesion (anchorage), the influence of interface strength like in the case of hooked-end fibers can be assumed as negligible.

Considering the undulated shape and the complex stages of pull-out of such a fiber (straightening, bending, friction etc.) high non-linearity of pull-out curve is expected. Even what in Fig.3.13. seems to be a linear initial part of pull-out curves is actually highly non-linear behaviour if we observe the same curves in a much smaller scale as demonstrated in Fig.3.15.

It was found from the curves presented in Fig.3.15. that the initial linear response can be associated only up to displacement value of approximately $u_z = 0.1$ mm. After this displacement level, debonding starts to occur starting from the fiber exit point where highest interface stresses occur.

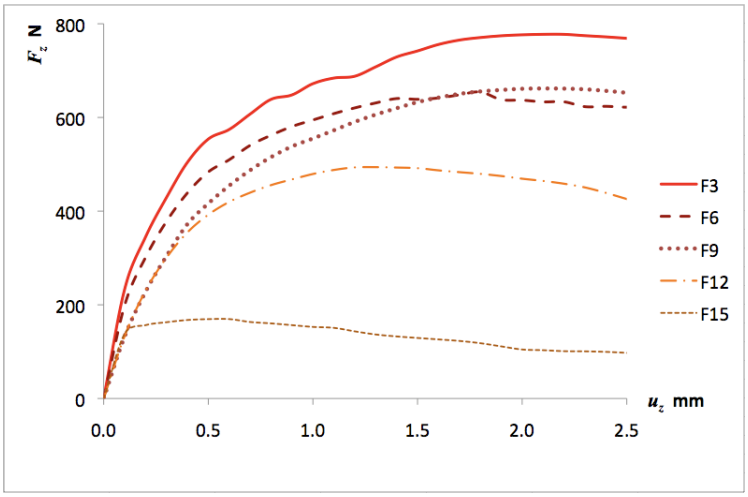


Fig.3.15. Initial part of average pull-out curves for undulated fibers: F3 ($l_f = 25$ mm); F6 ($l_f = 20$ mm); F9 ($l_f = 15$ mm); F10 ($l_f = 10$ mm); F15 ($l_f = 5$ mm)

Because of the undulated shape of fiber the interface debonding process is complex and while the interface debond grows, the effect of local friction in already debonded region may become significant. When fiber/matrix interface debonding has occurred along certain length of the undulated fiber and the sliding movement of fiber becomes possible it is, of course, counteracted by mechanical anchorage of fibers and hence a load sufficient to cause straightening and bending of fiber has to be applied in order to pull out the fiber.

At the peak load simultaneous straightening or bending of all embedded hooks takes place. After each hook has gone through the exit point (out of the matrix) the number of hooks subjected to straightening/bending decreases and thus the pull-out resistance of fiber correspondingly decreases. In fact, since the pull-out resistance of undulated fiber was proved to depend mainly on mechanical anchorage the decrease of pull-out load is almost linearly dependant on the length of remaining fiber provided that the channel in which fiber is embedded stays intact.

Although the decrease of pull-out load after the peak load can be generally considered as linear, there is a distinct characteristic of pull-out curves that some local regions of load increase exist as one can see in Fig.3.13. As a result of complete pull-out the shape of a undulated fiber becomes straight due to plastic deformations caused by applied tensile load and resistance at the last exit point from the matrix. Typical specimen with undulated fiber which has become straight after pull-out is shown in Fig.3.16. Initial positions of corrugation are still recognizable at a closer view.

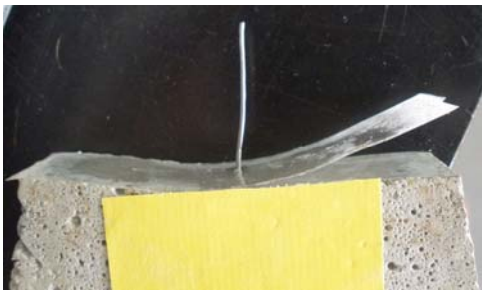

Fig.3.16. Undulated form fiber after complete pull-out

Generally, the pull-out test results revealed the benefits of undulated shape fiber since the highest maximal pull-out load as well as the highest resistance throughout the whole pull-out process was observed. The deviation between the pull-out curves as it will be shown further in the text was also much smaller than in the case of straight fibers where the interface bond strength and local friction governs the pull-out response. However, it is necessary to remember that high stress concentration occurs during the pull-out of undulated fibers. Under

real conditions of FRC, where many fibers often overlap and interact, the stress concentration may cause severe local failure of the concrete leading to more deviated results of, for example, flexural strength than it is found from single fiber pull-out tests.

Further in the text experimental pull-out curves revealing the influence of fiber inclination angle with respect to loading direction are shown in Fig.3.17., Fig.3.18. and Fig.3.19. for straight, hooked-end and undulated shape fibers respectively.

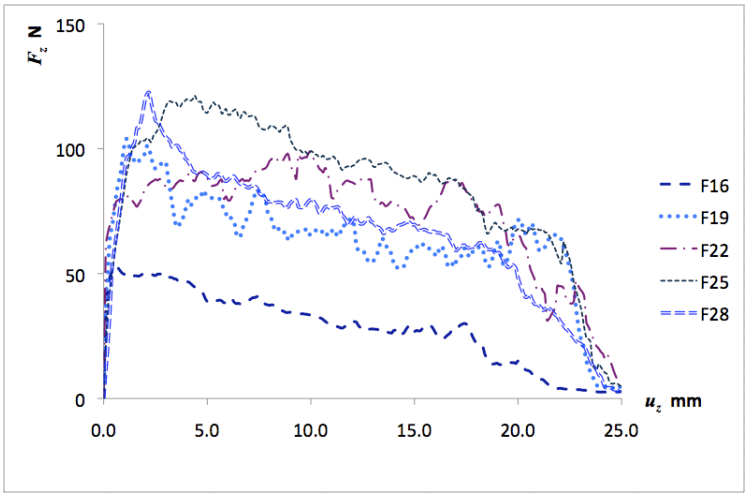


Fig.3.17. Average pull-out curves for straight fibers: F16 ($\alpha = 10°$); F19 ($\alpha = 20°$); F22 ($\alpha = 30°$); F25 ($\alpha = 45°$); F28 ($\alpha = 60°$)

Analyzing the pull-out curves for straight fibers shown in Fig.3.17. one can conclude that, generally speaking, increasing inclination angle has a beneficial effect on the pull-out resistance since pull-out tests for fibers F25 with fiber orientation angle $\alpha = 45°$ and F28 with $\alpha = 60°$ showed the highest maximal load value among all tested configurations. However, an opposite conclusion is that the displacement $u_z$ at maximal load is higher for inclined fibers and it normally increases with the inclination angle. This in turn is a drawback considering the crack width control.

It has to be noted that even though the inclination angle was different, the character of the curves presented in Fig.3.17. is similar for all studied configurations. This leads to conclude that fibers undergo the same stages (interface debonding, slip, local friction, etc.) in the same sequence but with different amount of work being necessary in order to complete each stage.


Fig.3.18. Average pull-out curves for hooked-end fibers: F2 ($\alpha = 0°$); F17 ($\alpha = 10°$); F20 ($\alpha = 20°$); F23 ($\alpha = 30°$); F26 ($\alpha = 45°$); F29 ($\alpha = 60°$)

Fig.3.18. shows the influence of inclination angle for hooked-end fiber pull-out relation. Judging from the curves presented in Fig.3.18. the influence of fiber orientation angle is significant also for hooked-end fibers. The most notable observation from Fig.3.18. is that the peak of the maximal pull-out load shifts towards higher values of displacement $u_z$ as the inclination angle increases. Opposite from study of inclined straight fibers, no increase of maximal load has been found in the case of hooked-end fibers. Since it was concluded previously that for hooked-end fibers the maximal pull-out load depends mostly on mechanical anchoring, there is no reason to expect significant increase of the pull-out load if these fibers are inclined. However, it is clearly seen that, when the end hooks have been straightened and the fiber has basically become a straight, inclined fiber, the influence of the inclination angle is important. In fact, the trend from Fig.3.18. is that the highest inclination angle observed ($\alpha = 60°$) demonstrates the highest pull-out resistance due to additional local friction forces at the fiber exit point.

Finally, the influence of inclination angle for undulated fiber pull-out relation is analyzed. According to pull-out curves in Fig.3.19. for undulated shape fibers, the influence of inclination angle was also found to be significant. No significant change of maximal pull-out load was found in the angular range between $\alpha = 0°$ up to $\alpha = 45°$, however, for inclination angle $\alpha = 60°$, the maximal pull-out load was considerably smaller ($F_z$ = 500 N) than for the aligned fiber ($F_z$ = 800 N). No general dependence on inclination angle could be found from the post-peak sections of curves (after the maximal pull-out load) since the pull-

out resistance of all inclined fibers in the post-peak section seems to be very similar. Even the samples with highest inclination angle $\alpha = 60°$ for which the maximal pull-out load was significantly smaller showed the same degree of resistance after the peak load as fibers with other angle configurations.

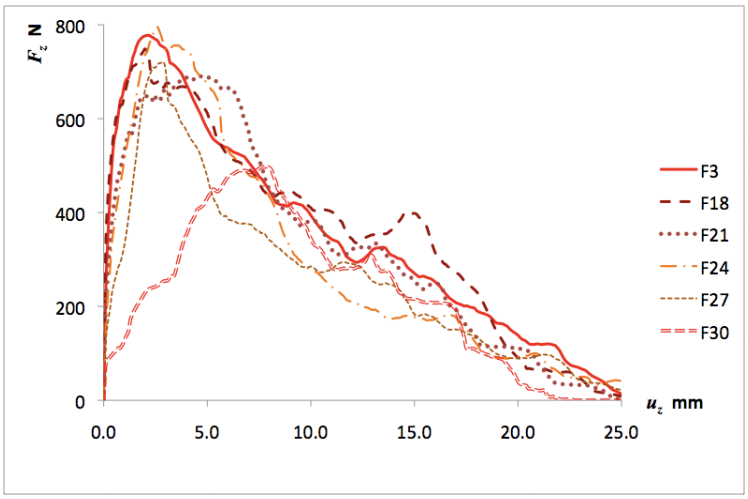


Fig.3.19. Average pull-out curves for undulated fibers: F3 ($\alpha = 0°$); F18 ($\alpha = 10°$); F21 ($\alpha = 20°$); F24 ($\alpha = 30°$); F27 ($\alpha = 45°$); F30 ($\alpha = 60°$)

Similar trends with some few exceptions were also found for inclined fibers with other fiber embedded lengths for all 3 types of fibers. The pull-out curves of these cases will not be analyzed in detail in this study. The pull-out curves for inclined fibers embedded at lengths $l_f$ equal to 20, 15, 10 and 5 mm are presented in Appendix.

One way to analyze the pull-out of fiber is by the pull-out relation $F_z$ - $u_z$. Often graphical representation of such relation is not comprehensible and quantity such as pull-out energy (work) is used. The pull-out energy $U_{sum}$ shows the amount of work necessary to pull-out the fiber and basically it can be interpreted as the area under the pull-out curve for the complete pull-out process, i.e.,

$$U_{sum} = \int_0^{l_f} F_z du_z \tag{3.1}$$

High pull-out energy values speak for the ductility associated with the pull-out process, while low values are related to more brittle character and less energy dissipation.

Pull-out energy may also be used as a convenient way to analyze the statistical distribution of pull-out curves for each configuration. In the present study the pull-out energy $U_{sum}$ values were calculated for the complete range of pull-out curve. Certainly a more

detailed analysis of pull-out energy related to different events of the pull-out process such as interface debonding, straightening of the hooks, etc., is possible and maybe the whole pull-out relation is not relevant keeping in mind the structural applications especially at large displacements. However, the aim of this study is to evaluate the overall pull-out performance of fibers.

Along with calculation of the pull-out energy $U_{sum}$, maximal force $F_{\max}$ for all configurations listed in Table 3.2 was analyzed. It was shown in the pull-out test curves for all 3 types of fibers in all configurations that there is the maximal force $F_{\max}$ after which the pull-out resistance decreases. This suggests that in a load controlled test the pull-out after the maximal load $F_{\max}$ would accelerate. Thinking in a structural level and assuming that the behaviour of a structural element in the post-cracking stage depends on the fiber pull-out mechanism we can imagine that exceeding the maximal load bearing capacity would cause catastrophic failure of the structural element.

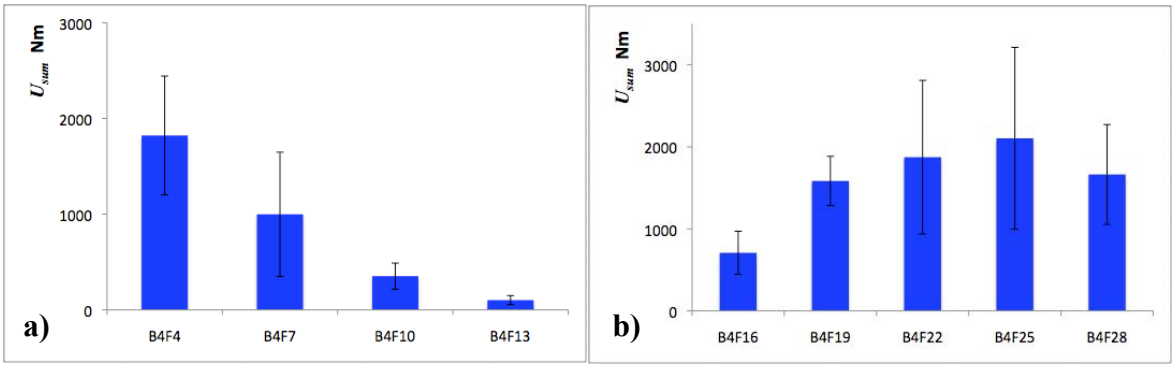


Fig.3.20. Pull-out energy $U_{sum}$ for straight fibers. Results shown for: a) different embedded lengths; b) different inclination angles

In Fig.3.20. pull-out energy $U_{sum}$ and its standard deviation has been shown for straight fibers in different configurations according to Table 3.2. Fig.3.20.a shows results for straight fibers with different embedded lengths. As it can be seen from Fig.3.20.a the obvious trend is that the higher embedded length can be related to higher pull-out energy. Generally, standard deviation in range between 35 to 65 % was found for straight aligned fibers. The highest deviation approximately 65 % was found for configuration F7, where $l_f = 15$ mm. In Fig.3.14.b the pull-out energy $U_{sum}$ for straight, symmetrically embedded fibers with different inclination angles is compared. According to calculations the smallest pull-out energy corresponds to configuration F16 where $\alpha = 10°$. The pull-out energy increases for

configurations F19 ($\alpha = 20°$), F22 ($\alpha = 30°$) and F25 ($\alpha = 45°$), but as it is shown in Fig.3.20.b the pull-out energy for configuration F28 ($\alpha = 60°$) is smaller.

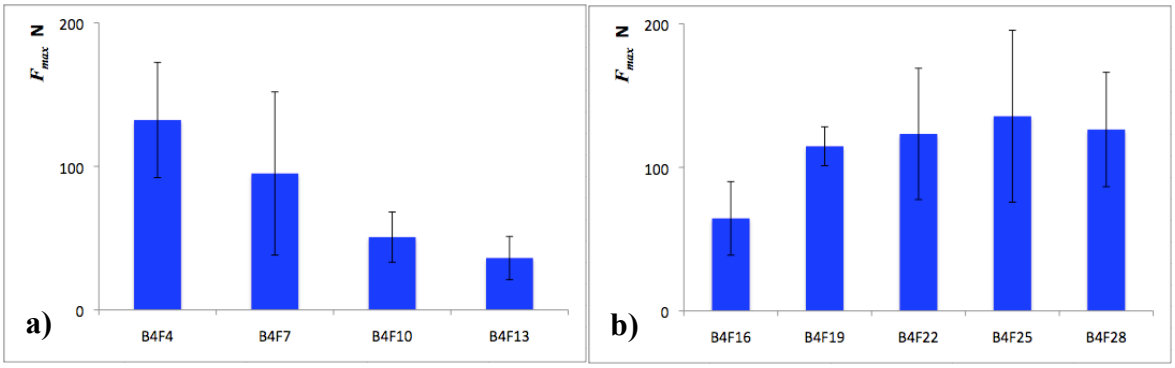


Fig.3.21. Maximal pull-out load $F_{max}$ for straight fibers. Results shown for: a) different embedded lengths; b) different inclination angles

In Fig.3.21. the maximal pull-out load $F_{max}$ is shown for straight fibers. Fig.3.15.a shows how the maximal pull-out load $F_{max}$ decreases as the embedded length of the fiber decreases. Standard deviation for results in Fig.3.21.a varies between 30 to 60% with the highest deviation corresponding to configuration F7 and the lowest to configuration F4. In Fig.3.21.b the maximal pull-out load $F_{max}$ values and deviation are shown for different inclination angles. According to results the highest maximal pull-out load corresponds to configuration F25 with inclination angle $\alpha = 45°$. These results give motivation to research the optimal angle of fiber inclination that would provides the highest pull-out load and highest pull-out energy. However, it can be clearly seen from Fig.3.21.b, that the standard deviation increases with the inclination angle in the range from $\alpha$ = 10° to 45°. Standard deviation for samples with configuration F28 with $\alpha$ = 60° is smaller than for configuration F25.

The pull-out energy $U_{sum}$ values and standard deviation for hooked-end fibers with different embedded lengths and inclination angles are shown in Fig.3.22.a and b.

From the results presented in Fig.3.22.a it can be concluded that the pull-out energy is smaller for smaller embedded lengths although the dependence on $l_f$ is not so strong as in the case of straight fibers. Standard deviation for results given in Fig.3.22.a is in the range between 20% and 29%. The highest deviation of approximately 29% corresponds to configurations F2 and F14. For configuration F2, where $l_f$ = 25 mm, the high deviation can be explained by the fact that the length of fiber is long and after straightening the fiber behaviour is generally the same as for straight fibers involving, for example, non-predictable

events such as local increase of friction. For the F14 configuration, on the other hand, the embedded length is short ($l_f$ = 5 mm) and the fiber end hook is situated near the exit point. Regarding the straightening of fiber, it can be expected that significant stress concentration will occur and spalling of concrete matrix is especially favoured in the vicinity of fiber exit point. Thus the pull-out behaviour for fiber with configuration F14 becomes dependent on unstable matrix cracking which results in higher deviation.

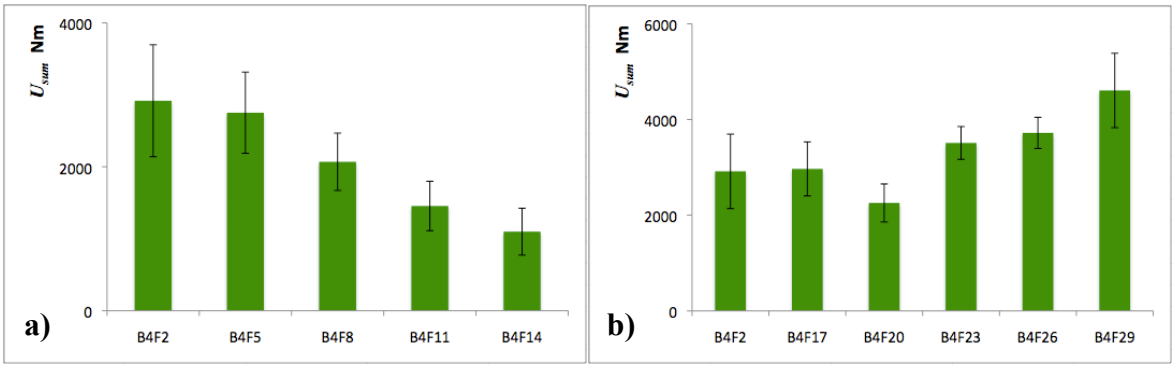


Fig.3.22. Pull-out energy $U_{sum}$ for hooked-end fibers. Results shown for: a) different embedded lengths; b) different inclination angles

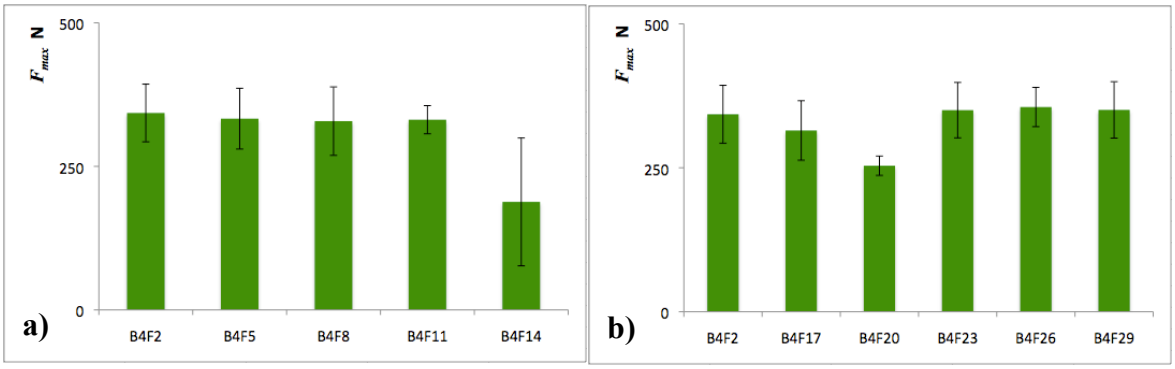


Fig.3.23. Maximal pull-out load $F_{\max}$ for hooked end fibers. Results shown for: a) different embedded lengths; b) different inclination angles

In Fig.3.23. results for maximal pull-out load $F_{\max}$ are presented for hooked-end fibers. One can certainly note the independence of maximal pull-out load on the embedded length for fiber configurations F2, F5, F8 and F11. The high deviation of results for $F_{\max}$ can be noted for configuration F14 which, as explained earlier, is a result of increased concrete matrix spalling.

Considering the $F_{\max}$ angular dependence shown in Fig.3.23.b it is difficult to draw any conclusions. Although the results in Fig.3.23.b show that $F_{\max}$ is the smallest for

configuration F20 ($\alpha$ = 20°) this has to be confirmed by additional study. Also the standard deviation in Fig.3.23.b does not seem to have a systematic dependence on inclination angle.

In general, standard deviation for the pull-out energy $U_{sum}$ is significantly smaller for hooked-end fibers compared to straight fibers, which proves the previous conclusions and demonstrates the advantage of hooked-end fibers.

Not like it was found for the case of hooked-end fibers the pull-out energy for undulated shape fibers is very dependent on the embedded length, since the pull-out resistance of undulated was earlier found out to depend directly on the number of embedded hooks. This is well shown in Fig.3.24.a. The standard deviation of results presented in Fig.3.24.a was in the range between 10 to 30% with the highest deviation 30% corresponding to the shortest embedded length configuration F15. The high deviation for the shortest embedded length may again be explained by the occurrence of matrix spalling during straightening.

According to results in Fig.3.24.b a general trend is that the pull-out energy of undulated fiber decreases with the increase of inclination angle. However, the standard deviation for configurations F21, F24 and F27 with inclination angles $\alpha$ = 20°, 30° and 45° respectively, was in the range between 25 and 50 %.

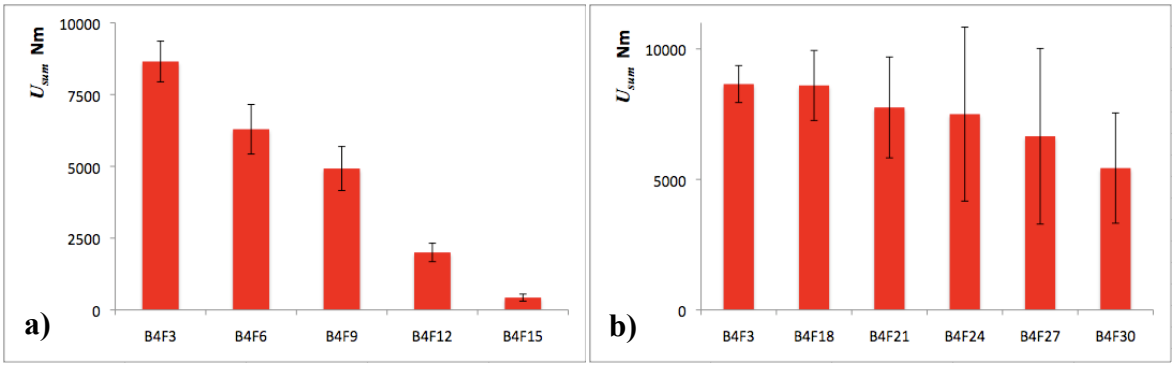


Fig.3.24. Pull-out energy $U_{sum}$ for undulated shape fibers. Results shown for: a) different embedded lengths; b) different inclination angles

Results of maximal pull-out load $F_{\max}$ are summarized in Fig.3.25. Fig.3.25.a shows the dependence on embedded length while in Fig.3.25.b dependence on inclination angle is shown. Compared with the pull-out energy results shown in Fig.3.24. much smaller deviation of average values is notable. For example, for configurations F3, F6, F9 and F12 with respective embedded lengths $l_f$ = 25, 20, 15, and 10 mm, the standard deviation was in the range of only 6 to 10 %. For the shortest embedded length the corresponding deviation was 25 %. Judging from Fig.3.25.b it can be concluded that the maximal pull-out load $F_{\max}$ does not

depend on inclination angle in the range between $\alpha$ = 0° (F3) and $\alpha$ = 30° (F24). However, for higher inclination angles, such as $\alpha$ = 45° (F27) and $\alpha$ = 60° (F30), the values of $F_{max}$ decrease. The deviation can be generally concluded to increase with the inclination angle.

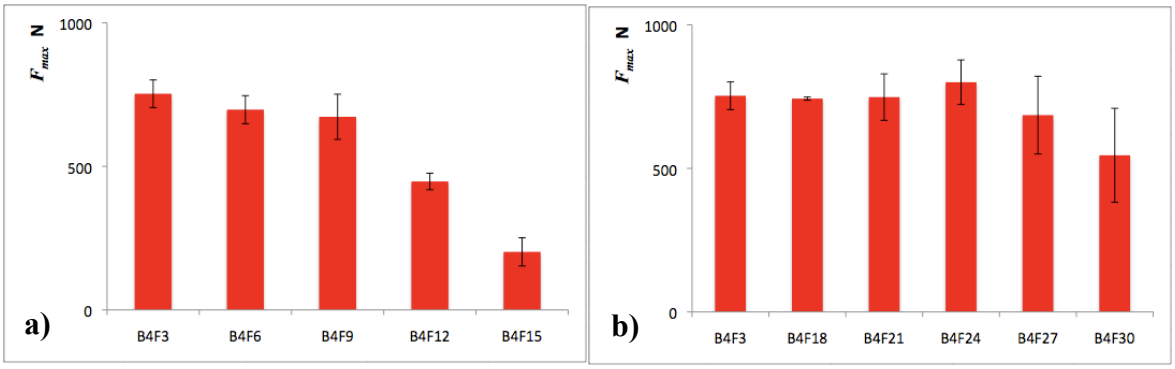


Fig.3.25. Maximal pull-out load $F_{max}$ for undulated shape fibers. Results shown for: a) different embedded lengths; b) different inclination angles

To sum up results for undulated shape fibers, certainly higher pull-out energy and higher maximal force values have to be emphasized. However, compared to hooked-end fibers higher deviation of results has to be noted for undulated fibers. Deviation generally increases with the inclination angle and for very short embedded lengths there will always be higher deviation of pull-out response. This means that using undulated shape fibers in FRC significantly higher load bearing capacity can be achieved, but the expected strength will be more difficult to determine accurately.

All pull-out tests were performed using the same concrete mix design according to Table 3.1. Certainly the pull-out response of all fibers depends also on mechanical properties of the concrete matrix. To investigate experimentally the influence of concrete matrix strength, mix design, density and other properties is a tedious task to include and it has not been covered in this study. However, it was already previously stressed that concrete matrix properties significantly affect fiber/matrix surface friction, residual shrinkage stresses, matrix spalling, etc. Given the fact that matrix properties are significant to account for but additional experimental tests are time consuming, numerical modelling can be the best alternative. Therefore, parametric analysis of several mechanical properties of concrete has been performed in the next section, where fiber pull-out process is analyzed using 2-D and 3-D finite element models.

## 3.5. Remarks on the specimen quality and the representativeness of the pull-out experiment

The results presented and discussed in this section were obtained by performing detailed and broad manufacturing and mechanical testing programme. In all cases it was always aimed to perform manufacturing of the specimens as precisely as possible by adjusting the fiber orientation angle, embedded length, by controlling the quality and homogeneity of fresh concrete mix, by avoiding to introduce imperfections such as air voids and so on. The specimens, which were considered to be insufficient in terms of quality, were not taken into consideration and were excluded from the testing programme. Even after the pull-out tests were performed, the quality of each test specimen was reconsidered by observing the surface and the actual embedded length was measured. More specimens were thus excluded after the quality control. Nevertheless, the manufacturing method used in this study was based on the hand lay-up technique, which inevitably introduces imperfections even if additional care on accuracy is taken.

Further, the representativeness of the testing rig has to be addressed. As known, in this study, the aim of a pull-out test is to study the pull-out behaviour of a single fiber. Different embedded lengths as well as orientation angles were studied in order to comprehend the behaviour of a chaotically oriented fiber, which is bridging the load over the micro level or the macro level crack in tensile loaded section of FRC structural element (beam, plate, shell, etc). Crack opening conditions according to real structural element should therefore be maintained during the pull-out experiments. It was already discussed previously that in order to analyze a single fiber pull-out process, the specimens with the current build-up can be considered as sufficient. However, if inclined fiber pull-out tests are performed according to scheme shown in Fig.3.1. the part of fiber, which has pulled out and is no longer supported by the solid concrete matrix will tend to align itself with the direction of applied tensile load. As a result, horizontal reaction force component starts to act in the pull-out sample. In order to maintain representative crack opening conditions for structural FRC elements subjected to bending loads the horizontal reaction force should be constrained since no Mode II displacements of surfaces are really possible in such case. Some extent of shear displacement might be possible in axially tensile loaded FRC elements but only after the concrete matrix section has been fully cracked and fibers become the only stress bridging elements. The interest of this study is to employ the obtained pull-out relations in a model for predicting the load bearing capacity and post-cracking behaviour of FRC beams subjected to flexural loads.

Restraining the horizontal forces in the experimental set-up used in this study by a rail or similar limiting tool would cause friction forces which would contribute to the resistance to pull-out load. A possible solution for minimizing the influence of friction could be introduction of rolling type of restraints but manufacturing of such equipment requires additional expenses and the experiments become more sophisticated.

In the present study no restraints were applied to counteract the horizontal reaction forces. Despite the rigid elements of the grips a considerable horizontal displacement between the jaws was observed during the pull-out of inclined fibers. However, it was observed that at small pull-out displacements, when the loads are usually the highest, the horizontal movement of the grips is not significant. Therefore, it can be considered that in terms of determining the maximal pull-out load and corresponding displacement the present method is sufficient and accurate. The deviation from the "representative" behaviour starts when pull-out displacements of highly inclined fibers are large, which is often not of interest in most structural applications. The straightening of fibers due to the reaction forces results in inclination of angle between the pull-out load and the crack surface. Judging from the results obtained from pull-out tests of inclined fibers (Fig.3.17., 23 and 24) and from the data available in the literature [80] it can be concluded that the obtained load values are probably larger than it would be in restrained, representative crack opening conditions.

From the pull-out test results demonstrated in this section it can be concluded that all characteristic stages of fiber pull-out have been identified also for inclined fibers– i.e., during the pull-out process the fiber is subjected to the same stages as in the case of aligned fibers, but the values of reaction forces and displacements depend on the inclination angle.

As the pull-out process of the fiber progresses, the pull-out resistance decreases and also does the horizontal reaction forces. This means that at one point the horizontal displacement once again becomes insignificant.

## 3.6. Summary of experimental fiber pull-out tests

In this chapter experimental pull-out tests were performed in order to obtain representative pull-out laws for three different types of commercially available steel fibers. The pull-out laws are intended to be used as an input data for the larger scale model described in Chapter 5 of this study. The model described in Chapter 5 is elaborated for predicting the load bearing capacity and post-cracking behaviour of FRC elements subjected to bending loads.

Regarding the chaotic orientation of fibers in FRC the influence of embedded length and inclination angle were studied in this chapter and 66 different configurations of fibers were experimentally tested in almost 600 single fiber pull-out experiments.

The samples were produced by specially elaborated hand lay-up technique and the tests were performed in tensile testing machine, the pull-out displacements were measured using non-contact videoextensometer.

The pull-out curves for all relevant configurations have been presented and all the micromechanical events during the pull-out have been analyzed. The statistical deviation for all configurations were analyzed by comparing the total pull-out energy $U_{sum}$ and the maximal pull-out load $F_{\max}$.

Undulated shape fibers were concluded to have the highest resistance to pull-out since the values of $U_{sum}$ and $F_{\max}$ were much higher than for hooked-end fibers and, understandably, for the straight fibers.

However hooked-end fibers were best in terms of combining high pull-out resistance with uniformity of test results as the standard deviation of $U_{sum}$ and $F_{\max}$ values was the smallest.

Straight fibers were proved to have low pull-out resistance and high scatter between the measured entities.

In the discussion part in Chapter 3 representativeness and applicability of the obtained pull-out curves were analyzed.

# 4. NUMERICAL MODELLING OF FIBER PULL-OUT PROCESS

In this chapter numerical FEM modelling of fiber pull-out process is performed for single straight cylindrical steel fiber that is aligned with the direction of the applied pull-out displacement. While micro damage initiation and propagation within a system consisting of a steel fiber embedded in a concrete matrix block is difficult to be measured experimentally FEM is an adequate tool to analyze it. Also, although there have been numerous analytical approaches demonstrated [9,42,43], the most of the analytical methods published in the literature still have struggled to provide a parameter-independant model for this problem.

Furthermore, since a short fiber reinforced composite is under consideration, a feasible analytical solution might not even be achievable because of the uneven stress distribution in fiber and weak bonding between fiber and matrix interaction. Also issues of interaction between fibers have not been studied.

The objective of this section is to provide a detailed micromechanical analysis of the pull-out process of straight fiber and to analyze the significance of various parameters such as constituent material elastic properties, fiber geometry and others. Since it was already described before that the mechanical behaviour and load bearing capacity of a FRC structural element directly depends on the pull-out characteristics of the individual fiber, the parametric analysis presented in this chapter is aimed to provide a tool for materials scientist, engineer or materials selector to improve or achieve desirable mechanical properties of the designed structure.

It was also described in the literature review chapter of this work that new additives are nowadays widely used in FRC mix design that especially suit for better adhesion with the reinforcement fibers. The additives certainly affect both the fiber/matrix interface properties as well as the elastic properties of the concrete itself. So far the most of the studies have not discussed the general significance of these mentioned parameters.

Thus a detailed parametric analysis is performed in this chapter and the modelling parameters for particular cases are found and presented from the best fit with experimental results determined in Chapter 3. Generally, it means that experimentally measured fiber pull-out law (load vs. displacement) can be also used as the input data in a numerical model in order to calculate several micromechanical parameters and thus characterize the interface properties (for example, critical strain energy release rate $G_c$). Certainly, the calculated interface properties can then be employed to analyze other, more complex problems with different boundary conditions.

First, the debonding stage of fiber pull-out is modelled using a 2-D axisymmertric model. The potential crack propagation modes are analyzed. It is evaluated how different parameters, such as fiber and matrix elastic properties, fiber geometry and the shrinkage of concrete affect the propagation of debond crack. The propagation of crack is analyzed by linear elastic fracture mechanics approach by calculating the energy release rate $G$ for different interface debond lengths. The changes of energy release rate $G$ with the debond length are comprised in simple mathematical expressions that allows to perform debond crack growth simulations and, more importantly, to derive the fiber pull-out law in the debonding stage.

Further on, modelling of the complete fiber pull-out is performed using a 3-D FEM model. Two cases are subdivided: initially debonded interface, where it is assumed that there is no bonding between fiber and matrix, and initially bonded interface. Regarding the weak interface bond strength between the steel fiber and concrete, it might be applicable to neglect it in many cases. On the other hand, a constant development and improvement of concrete mix designs such as micro and nano-scale additives allows obtaining interfaces with much better properties than for conventional concrete. Both of these cases therefore could be interesting from point of view of application.

In both cases it is modelled and analyzed how the interface properties and residual shrinkage stresses affect the pull-out curves. It is shown that these parameters can be found for particular cases from the best fit with experimental pull-out test results.

All the numerical models used in this chapter were generated and solved using finite element code ANSYS [84].

## 4.1. Modelling of fiber/matrix interface debond crack growth

### 4.1.1. Interface debond crack initiation

Interface debonding is the first of the non-linear events to occur during the fiber pull-out process. When the fiber is subjected to pull-out load the initial response of fiber is expected to be linear elastic. However, as it was described in the literature review chapter, the interface bonds between steel fiber and concrete matrix are weak and thus occurrence of debonding is expected at relatively low loads.

The debond initiation and growth is significant to be analyzed since the pull-out resistance of fiber is expected to decrease when debonding is initiated and when debond crack propagates. Furthermore, during debonding process, the sliding movement (slip) of debonded

part of fiber with respect to its embedded position in the concrete matrix becomes possible which is in favour of opening of the crack. Thus from point of view of crack width control, the debond growth rate has to be prevented or slowed down.

Assuming that the interface strength is the same along the whole length of the embedded fiber, the interface debond crack will initiate at the maximal interface stress location. Distribution of stresses in the fiber and at the interface depend on the boundary conditions and thus different locations of debond crack initiation are possible. Two general cases relevant to the current study are: 1) a single fiber embedded and fully surrounded by a continuous matrix block; 2) a single fiber that is bridging the stresses over two crack-separated sections of concrete matrix. The two mentioned cases are shown in examples in Fig.4.1.a and b.

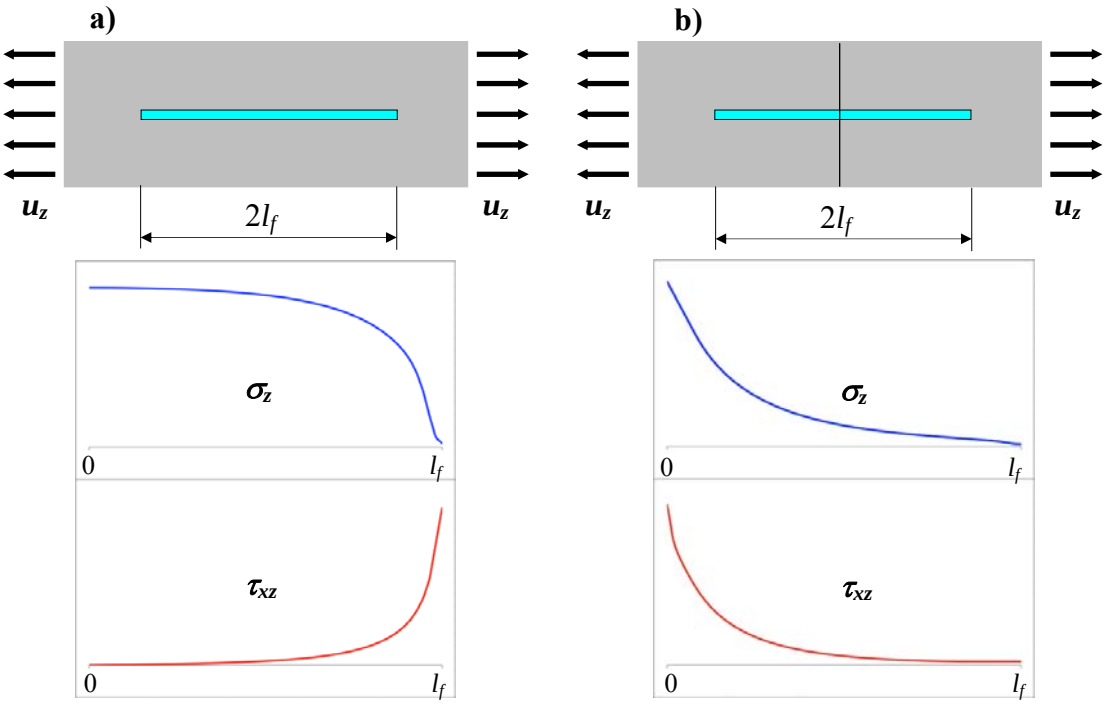


Fig.4.1. Short steel fiber with length $2l_f$ embedded in concrete matrix block, which is subjected to axial displacement $u_z$: a) case of continuous matrix; b) case of crack bridging

Stress distributions in Fig.4.1.a and b are shown for ½ of the fiber length, i.e., $l_f$. $\sigma_z$ is a notation for fiber axial stress and $\tau_{xz}$ is the shear stress at the fiber/matrix interface.

Once the debond crack starts to propagate, the further propagation of the debond crack will depend on the stress redistribution after crack growth. Typically for ceramic matrix composites with low interface strength it can happen that the debond crack propagation is instant and spontaneous because the energy released for initiating the crack may be larger

than the energy needed for crack propagation, and in such a case detailed response during the debonding stage cannot be experimentally measured. In a FEM based numerical model understandably, the debonding process can be analyzed in detail since the length of the debond crack can be controlled.

If the fiber is bridging a crack (see Fig.4.1.b), the largest interface shear stresses form at the fiber exit point. One can note that boundary conditions for this case are the same as for the samples used in the experimental study (Chapter 3).

When these interface shear stresses have reached the strength of the interface a debond crack will initiate. The amount of the released energy due to formation of this initial crack may be sufficient enough to cause immediate propagation of the debond crack along the whole length of the fiber/matrix interface. Because of the weak strength properties of the steel fiber/concrete interface, the growth of the debond crack is often under real circumstances an instant process. The other scenario might be that the initial debond crack propagates but then stops, for example, due to friction at a certain distance because the amount of released energy is not sufficient to propagate the crack further. In the latter scenario additional displacement $\Delta u_z$ is then required in order to cause the further debonding. The first scenario is assumed in sub-section 4.2.1. of this work, where fiber/matrix interface is considered as initially debonded.

If the second scenario takes place and step by step debond crack propagation is analyzed, then due to the stress redistribution the maximal shear stress will shift with the debond crack tip and the further increase of the pull-out displacement will lead to propagation of this debond crack.

In literature, there has not been presented a detailed parametric analysis of the interface debonding process in FRC and how it is affected by different elastic properties of the constituents, fiber embedded length and diameter, initial residual shrinkage pressure, etc. Therefore, it is the aim of this study to provide this parametric analysis and demonstrate significance of these parameters on interface debond growth rate for the cases of straight, aligned fibers (F4, F7, F10 and F13). And, since experimental data of fiber pull-out laws are available (Chapter 3), quantitative data such as values of fracture mechanics parameters can be found for these particular cases.

### 4.1.2. Characterization of debond crack growth by fracture mechanics analysis

In order to analyze crack initiation and propagation in engineering materials, fracture mechanics analysis has been most commonly used method. Fracture mechanics parameters such as stress intensity factor $K$ and energy release rate $G$ are commonly used to estimate whether the given applied load will cause crack initiation or propagation.

Interface debonding is a Mode II crack propagation and is very commonly occurring in polymer based composites. An extensive number of analysis and modelling approaches are available in the literature [85-88]. The debond growth can be evaluated by calculating the energy release rate $G$ for a particular fixed debond length. If experimental measurements of debond crack length and crack growth are available, a critical value of energy release rate $G_c$ (fracture toughness) can be determined. $G_c$ which is a property of material can then be used in modelling crack growth at other different loading conditions.

While there have been many analytical solutions of energy release rate for continuous (long) fiber composites and long debond lengths [87,89], for short fibers or short debond lengths due to overlapping stress states the analysis and calculations of $G$ are usually more convenient to be performed numerically, e.g. using FEM [86] or BEM [88] calculations. There are several calculation techniques by which fracture mechanics parameters can be conveniently calculated particularly by FEM. Crack closure technique and virtual crack closure technique are widely used to calculate energy release rate of the debond cracks in composites with progressing damage [86,90,91]. In this study virtual crack closure technique was used and the principles of calculation are presented further in the text.

The case analyzed in this study is the one of aligned straight fiber bridging the stresses across two large, crack-separated concrete matrix blocks (see Fig.4.1.b). Then the problem can be considered as axisymmetric and the FEM model shown in Fig.4.2. can be used to analyze debond crack growth and calculate the energy release rates. The advantage of the axisymmetric problem is that a 2-D model can be used with the finite elements assigned to axisymmetric behaviour. In Fig.4.2. $z$ is the axis of symmetry, $r$ is the radial direction axis and the boundary conditions used are symmetry on the fiber at the exit point and uniform displacement on the surface of load application. Fiber radius used in the reference calculation example was equal to $r_f = 0.375$ mm that corresponds to the radius of straight steel fibers, which were used in experimental pull-out tests in Chapter 3.

Prior to doing calculations, a parametric study of mesh convergence and geometry of the model was performed. A refined mesh was used in vicinity of the crack tip in order to assure accurate results for stress and displacement distributions, which will later be used for $G$ calculations.

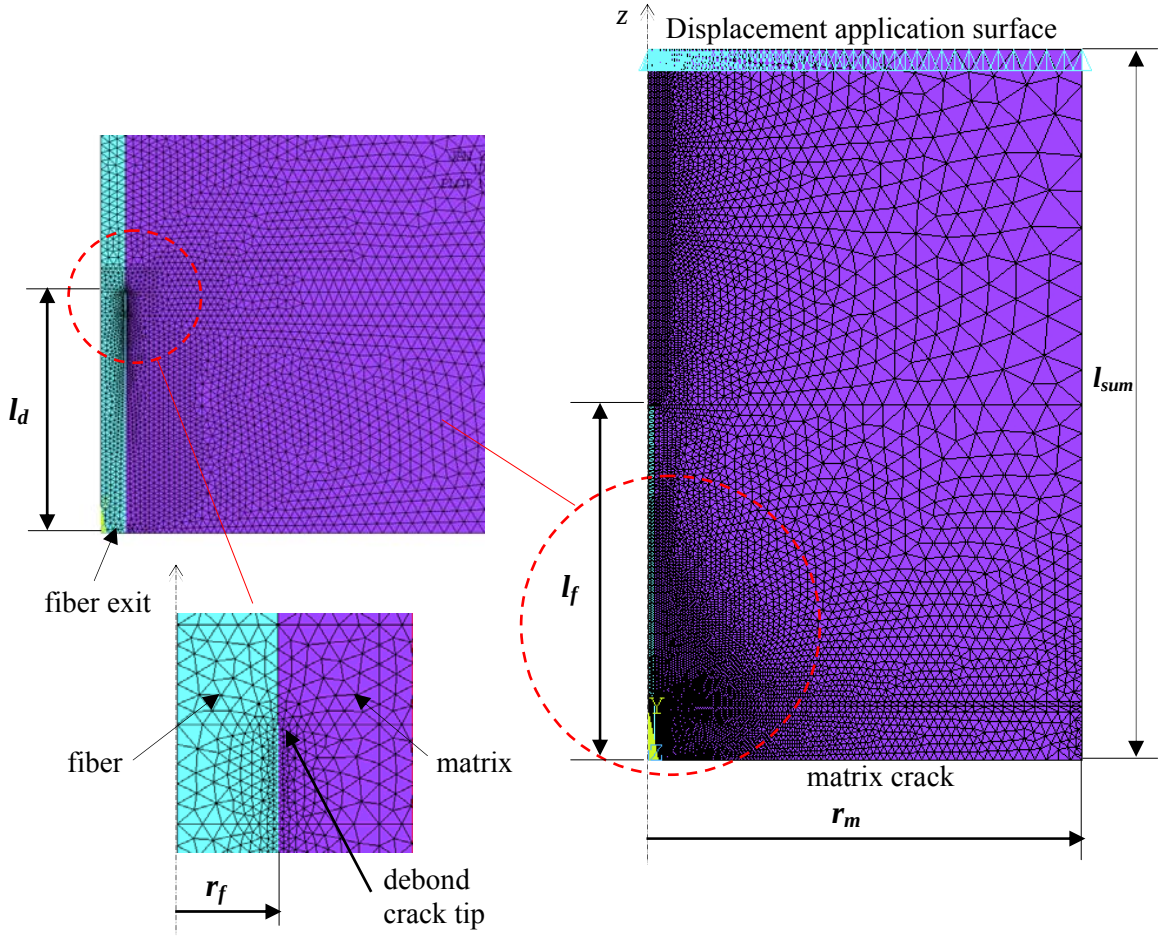


Fig.4.2. A 2-D axissymmetrical FEM model for $G$ calculations. Finite element mesh and geometrical parameters: $r_f$ - fiber radius; $r_m$ - outer matrix radius; $l_f$ - fiber embedded length ( ½ of total fiber length); $l_d$ - interface debond length; $l_{sum}$ - the length of the model

Apart from determination of necessary mesh refinement, the geometry of the model was also evaluated. Appropriate size of representative volumes has to be incorporated in the FEM model in order to avoid interaction between stress fields at the crack tip and the load application or outer boundary surfaces. On the other hand, it is preferable that the overall size of the FEM model is reasonably small in order to save calculation time.

A parametric analysis is therefore necessary to find a sufficient size of matrix radius $r_m$ as well as the total length of the model $l_{sum}$. The performed parametric analysis revealed that a model with outer diameter $r_m = 80 \cdot r_f$ and of length $l_{sum} = 130 \cdot r_f$ is sufficient. It has to be noted that the parametric analysis of pull-out problem geometry was already performed before, in order to elaborate a proper representative size of the experimental pull-out samples which were used in this study (Chapter 3).

Since the debond crack propagation was not measured experimentally, the comparison between numerical modelling and experimental results was performed indirectly and was based on numerically calculated fiber axial reaction forces during propagation of the debond crack.

Further, a description of the principles of the virtual crack closure technique are described.

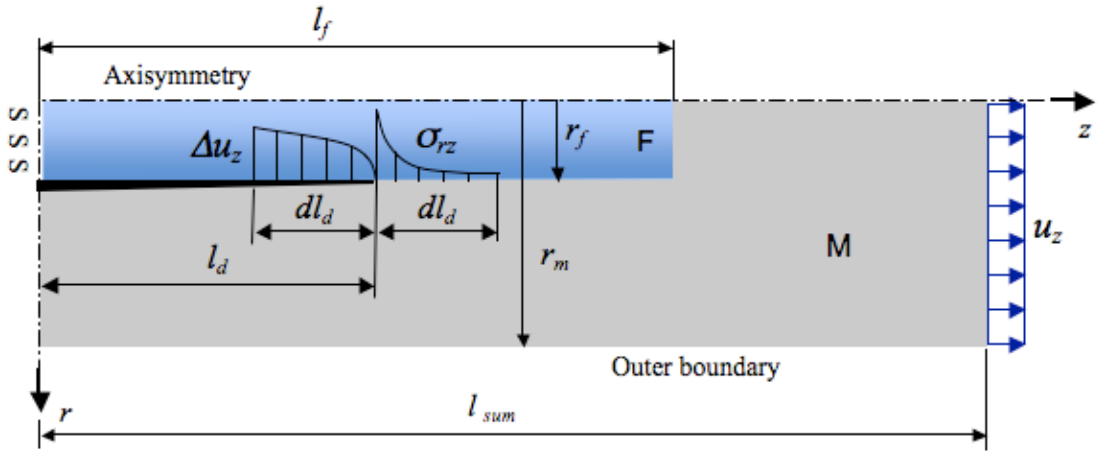


Fig.4.3. Schematic representation of an axisymmetric FEM model used for calculating *G* with virtual crack closure technique: F – straight steel fiber; M – concrete matrix; S – symmetry boundary conditions on fiber

The virtual crack closure (VCC) technique [90] is a convenient method to calculate the energy release rate *G* when doing FEM calculations regardless of the crack propagation mode.

For Mode II crack propagation, which is expected to dominate in the given fiber pull-out problem, the relative tangential displacement $\Delta u_z$ distribution behind the debond crack tip and the shear stress $\sigma_{rz}$ distribution ahead of the crack tip can be obtained directly from the FEM model as shown schematically in the Fig.4.3. The respective displacements for Mode I

crack propagation are in the radial direction $\Delta u_r$ and the respective stresses are the radial stresses $\sigma_r$ at the interface.

The main principle of the crack closure technique is that the energy released due to debond crack growth by $dA$ is equal to the work which is required to close the newly created surface from size $A + dA$ back to size $A$, where $dA = 2\pi r_f dl_d$. Upper indices in the further presented equations (Eqs. (4.1)-(4.6)) are used to indicate the length of the debond crack. Closing the debond crack by $dl_d$ (from length $l_d + dl_d$ to length $l_d$) by applying tangential (Mode II) or radial (Mode I) tractions, points at the debonded surface in the region $z \in [l_d; l_d + dl_d]$, which have relative tangential or radial displacement equal to:

$$\Delta u^{l_d+dl_d}(z) = u_{fz}^{l_d+dl_d}(z) - u_{mz}^{l_d+dl_d}(z) \tag{4.1}$$

are moved back to coinciding positions. At the end of this procedure the shear stress (Mode II) or radial stress (Mode I) in point $z$ is equal to $\sigma^{l_d}(z)$, which is the shear stress (Mode II) or radial stress (Mode I) in front of the crack with length $l_d$. Then the work required to close the crack by $dl_d$ can be expressed as follows:

$$W = 2\pi r_f \frac{1}{2} \int_{l_d}^{l_d+dl_d} \Delta u^{l_d+dl_d}(z)\sigma^{l_d}(z)dz \tag{4.2}$$

The principle of the VCC technique is the same as for the crack closure technique described here with the exception that that due to small value of $dl_d$ the relative sliding displacement (for Mode II) or relative radial displacement (for Mode I) at the tip of the crack with size $l_d + dl_d$ can be assumed to be equal as at the tip of the debond crack with size $l_d$, i.e.:

$$\Delta u^{l_d+dl_d}(z) = \Delta u^{l_d}(z - dl_d) \tag{4.3}$$

The benefit of this assumption in VCC technique is that only one stress state calculation for a given debond length $l_d$ is required (there is no need to calculate two stress states with respective lengths $l_d$ and $l_d + dl_d$).

Since the energy release rate is defined by relations:

$$dA = 2\pi r_f dl_d \tag{4.4}$$

where $A$ is the newly created surface area,

and the energy release rate is defined as:

$$G = -\frac{dU}{dA}\Big|_{u=const} \tag{4.5}$$

where the work $W$ has been expressed in terms of the released strain energy $U$ through relation $W = -U$.

The following expression is obtained using Eqs.(4.2), (4.3) and (4.4):

$$G\ (l_d) = \lim_{dl_d \to 0} \frac{1}{2dl_d} \int_{l_d}^{l_d + dl_d} \Delta u^{l_d} (z - dl_d) \sigma^{l_d} (z) dz \tag{4.6}$$

where term $G(l_d)$ denotes that energy release rate is a function of debond length $l_d$.

It has to be noted though that for the FEM based solution the integration is performed over a finite region ($dl_d$ in this case), which most probably is larger than the region where the solution for stresses is local (singular). Therefore, the values obtained using Eq.(4.6) will not accurately correspond to $G$. In fact, the value calculated by Eq.(4.6) depends on the integration region $dl_d$ and rather should be called "energy release rate over distance $dl_d$".

As it was mentioned, in the current study FEM software code ANSYS [84] was used for numerical calculations. One can use the post-processing options such as path and array operations provided by the software to facilitate calculation of $G$ using Eq.(4.6).

In the reference example properties of the constituents (see Table 4.1) were in correspondence with those used in experimental part of this study. In the following parametric analysis different properties of constituents and geometrical entities were changed in order to evaluate their significance on $G$ and thus on the debond crack propagation. In all parametric cases both steel fiber and concrete matrix were assumed to be isotropic materials.

### 4.1.3. Interface debond crack growth modelling results. Parametric analysis

The simplest case to model is a problem assuming that there are no initial residual stresses caused by concrete shrinkage. In such case the only loading in the model would be mechanical load in form of the applied displacement $u_z$ (see Fig.4.3), which causes the reaction force at the symmetry surface to induce pull-out of the embedded fiber. However, in most practical applications the residual shrinkage stresses are present. In order to evaluate for that, the simpest approach would be to use thermal analogy by assigning thermal expansion (contraction) properties to the concrete matrix and applying thermal load (temperature change) and solving it as the first load step prior to applying the mechanical pull-out.

Considering the case with no residual stresses, when mechanical load is applied through displacement $u_z$, tensile stress will occur in fiber and due to stress transfer through the

interface the stresses will be also induced in the concrete matrix, meaning that radial contraction in both constituents will occur. Considering the typical material elastic properties of steel and concrete matrix (given in Table 4.1) a larger contraction is expected for the steel fiber since Poisson's ratio is always higher than for concrete. This leads to conclude that for the given boundary conditions and material properties the applied displacement apart from causing the shear (Mode II) will also cause the radial (Mode I) opening and mixed mode crack propagation will take place. While in general the interface between steel fiber and concrete matrix can be considered as having weak mechanical properties Mode I crack propagation is still more undesirable since the fracture toughness $G_{Ic}$ is usually much lower than $G_{IIc}$. Thus in order to prevent or slow down the rate of debond growth it would be useful to eliminate or reduce Mode I crack propagation. In the following calculations both crack propagation modes were considered and the parametric analysis reveals how different factors could increase or decrease crack propagation in a certain mode.

The cases of parametric analysis have been summarized in Table 4.1.

Table 4.1.

Cases of the parametric analysis

| Case name: | $E_f$ | $E_m$ | $\nu_f$ | $\nu_m$ | $r_f$ | $l_f$ | $l_f / r_f$ | $\Delta T$ |
|---|---|---|---|---|---|---|---|---|
| | [GPa] | [GPa] | [-] | [-] | [mm] | [mm] | [-] | [°C] |
| Reference | 210 | 30 | 0.3 | 0.2 | 0.375 | 20 | 53.33 | 0 |
| Case 2 | 210 | 30 | 0.3 | 0.2 | 0.375 | 15 | 40 | 0 |
| Case 3 | 210 | 30 | 0.3 | 0.2 | 0.375 | 10 | 26.67 | 0 |
| Case 4 | 210 | 30 | 0.3 | 0.2 | 0.375 | 5 | 13.33 | 0 |
| Case 5 | 210 | 30 | 0.3 | 0.2 | 0.4 | 20 | 50 | 0 |
| Case 6 | 210 | 30 | 0.3 | 0.2 | 0.5 | 20 | 40 | 0 |
| Case 7 | 200 | 30 | 0.3 | 0.2 | 0.375 | 20 | 53.33 | 0 |
| Case 8 | 220 | 30 | 0.3 | 0.2 | 0.375 | 20 | 53.33 | 0 |
| Case 9 | 210 | 35 | 0.3 | 0.2 | 0.375 | 20 | 53.33 | 0 |
| Case 10 | 210 | 25 | 0.3 | 0.2 | 0.375 | 20 | 53.33 | 0 |
| Case 11 | 210 | 30 | 0.35 | 0.2 | 0.375 | 20 | 53.33 | 0 |
| Case 12 | 210 | 30 | 0.25 | 0.2 | 0.375 | 20 | 53.33 | 0 |
| Case 13 | 210 | 30 | 0.3 | 0.25 | 0.375 | 20 | 53.33 | 0 |
| Case 14 | 210 | 30 | 0.3 | 0.15 | 0.375 | 20 | 53.33 | 0 |
| Case 15 | 210 | 30 | 0.3 | 0.2 | 0.375 | 20 | 53.33 | -10 |
| Case 16 | 210 | 30 | 0.3 | 0.2 | 0.375 | 20 | 53.33 | +10 |

Both energy release rates $G_I$ and $G_{II}$ were calculated using Eq.(4.6). For the reference case fiber radius was equal to $r_f$ = 0.375 mm. As it is stated in Table 4.1 four cases of fiber

embedded lengths were studied corresponding to the ones used for experimental study: $l_f = 20$ mm (fiber aspect ratio $l_f / r_f = 53.33$) corresponding to F4 in experimental study; $l_f = 15$ mm ($l_f / r_f = 40$) corresponding to F7; $l_f = 10$ mm ($l_f / r_f = 26.67$) corresponding to F10; $l_f = 5$ mm ($l_f / r_f = 13.33$) corresponding to F13. The initial debond length in all cases was chosen equal to $l_d = 1.5 \cdot r_f$ and then increased for each of the subsequent calculations until debond length $l_d$ is equal to fiber embedded length $l_f$. In Case 5 and 6 (see Table 4.1) the significance of fiber radius $r_f$ was analyzed. Also in the cases of parametric analysis the effect of fiber and matrix elastic modulus $E_f$ and $E_m$ (Cases 7 – 10) , Poisson's ratio $\nu_f$ and $\nu_m$ (Cases 11 – 14). Finally the significance of residual stresses was analyzed in Cases 15 and 16.

In the following the calculation results are presented for all studied cases showing: 1) energy release rate as a function of normalized debond length, i.e., $G(l_{dn})$, where $l_{dn} = l_d / r_f$ 2) the significance of different parameters on it. The applied displacement in all cases studied here was $u_z = 0.005$ mm. Although for the sake of parametric analysis the value of applied displacement could as well be different (since the modelling is linear elastic), this particular value was chosen because the reaction forces for such case would be somewhat close to the experimentally measured forces. For example, for the reference case defined in Table 4.1 the corresponding reaction force from the applied displacement $u_z = 0.005$ mm was equal to $F_y = 258.2$ N.

The first results presented in Fig.4.4. are Mode I and Mode II energy release rates $G_I(l_{dn})$ and $G_{II}(l_{dn})$ for the reference case. As it is seen in the picture, Mode II energy release $G_{II}(l_{dn})$ values are overall higher although it has to be concluded that Mode I energy release $G_I(l_{dn})$ has considerable contribution to debond crack propagation at shorter debond lengths.

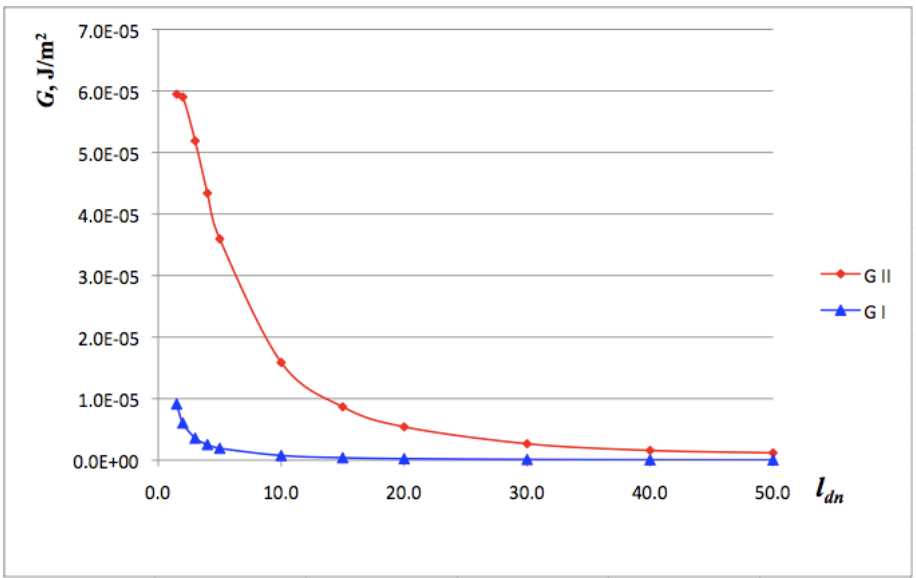

Fig.4.4. Mode I and Mode II energy release rate ($G_I$ and $G_{II}$ respectively) for the reference case in Table 4.1 presented as a function of normalized debond length $l_{dn} = l_d / r_f$. $u_z = 0.005$ mm

As it can be seen in Fig.4.4. both $G_I$ and $G_{II}$ are much higher at smaller debond lengths, where the interaction between debond crack and the bridged matrix crack is significant. As the debond crack length increases the distance between the debond crack tip and the matrix crack increases and thus interaction decreases resulting in smaller $G_I$ and $G_{II}$ numerical values. Would the fiber be continuous or with very high aspect ratio the energy release rates at certain debond length would achieve plateau values as it has been shown in literature [86] and the crack growth in such case could be considered as self-similar. For self-similar crack growth conditions analytical calculation methods are available (see for example [85]). In the current case, however, the aspect ratio of fiber is small and as shown in Fig.4.4. $G_I$ and $G_{II}$ continuously decrease until complete debonding of fiber has occured.

In Fig.4.5. the reaction force (equal and opposite to the pull-out load) $F_Z$ is shown. The figure can be interpreted as a case when a constant displacement (in this case $u_z = 0.005$ mm) is applied and the debond crack propagates. The curve then shows the decrease of the reaction force $F_Z$ as a result of fiber/matrix interface debonding. For the reference case according to the calculation results the reaction force decreases from above 200 N down to approximately 25 N, which, of course, is a significant decrease and further motivates the interest to perform this parametric analysis.

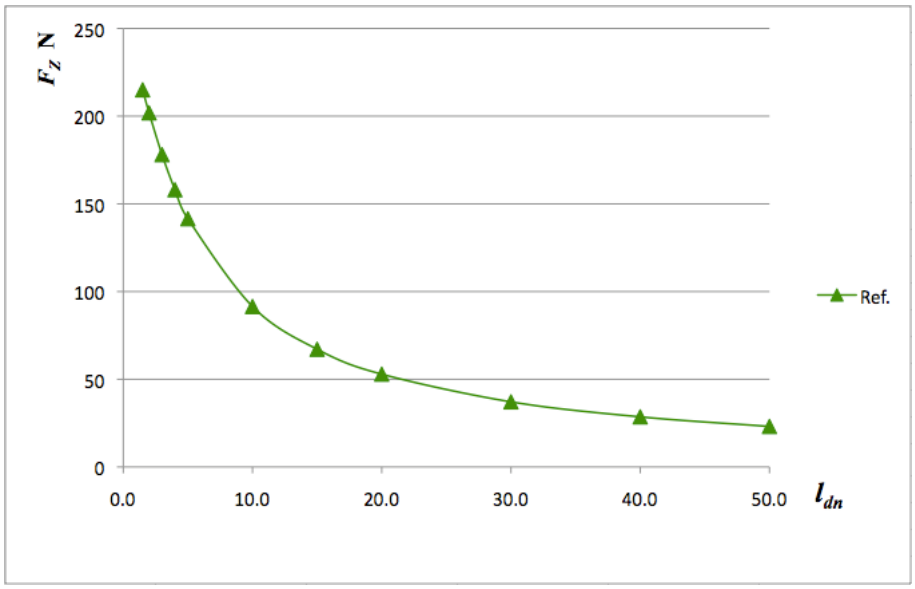


Fig.4.5. Reaction force $F_Z$ for the reference case (Table 4.1) presented as a function of normalized debond length $l_{dn}$

Fig.4.6. Shows Mode I energy release rate $G_I(l_{dn})$ for various embedded lengths $l_f$. The results presented in the figure state that fiber embedded length $l_f$ within the observed range does not affect $G_I$ and the propagation of the interface debond crack will occur at the same rate for all embedded lengths.

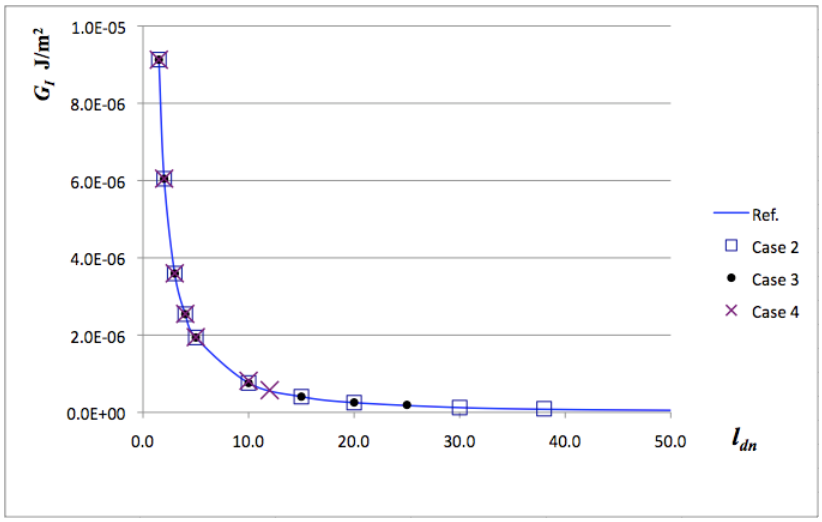


Fig.4.6. $G_I$ calculation results showing significance of fiber embedded length $l_f$. Cases according to Table 4.1

The same conclusion can be addressed to Mode II energy release rate $G_{II}(l_{dn})$ shown in Fig.4.7. As it is seen in figure, the deviaton from the reference case curve is evident only when fiber is almost fully debonded, which can not be considered important.

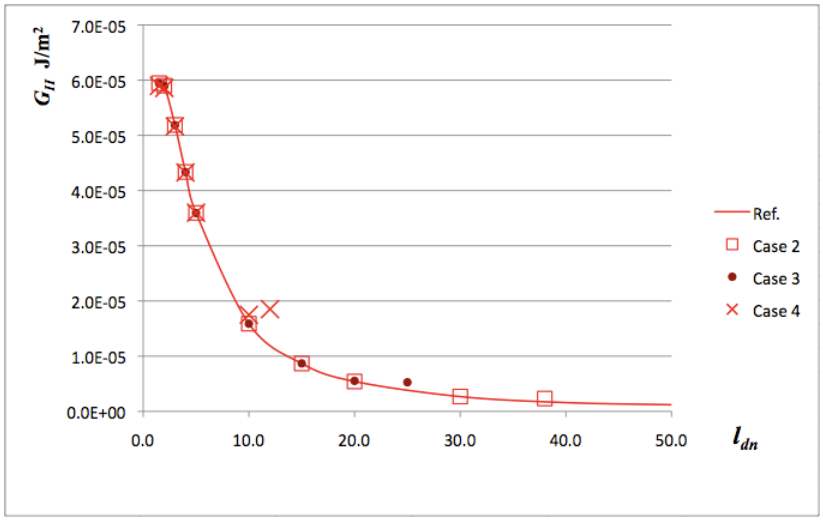


Fig.4.7. $G_{II}$ calculation results showing significance of fiber embedded length $l_f$. Cases according to Table 4.1

Further in the parametric analysis the results for significance of fiber radius $r_f$ (or fiber aspect ratio) are presented. Compared to the reference case, where $r_f$ = 0.375 mm, the fiber radius is increased to 0.38 mm and 0.4 mm in Cases 5 and 6 respectively. However, according to the results shown in Fig.4.8 and 4.9 the debond crack growth energy release rates $G_I$ and $G_{II}$ are smaller for larger size fibers, which can be explained by lower stresses in fiber due to cross-section increase. According to the trends of curves shown in Fig.4.8 and 4.9 the decrease of $G$ is linear with the increase of radius. This linear relation can be very useful to recalculate $G$ for various fiber aspect ratios.

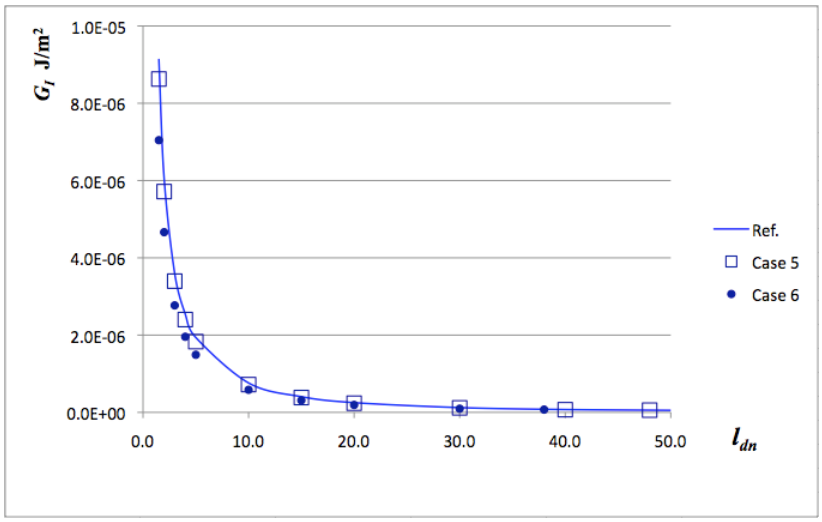


Fig.4.8. $G_I$ calculation results showing significance of fiber radius $r_f$. Cases according to Table 4.1

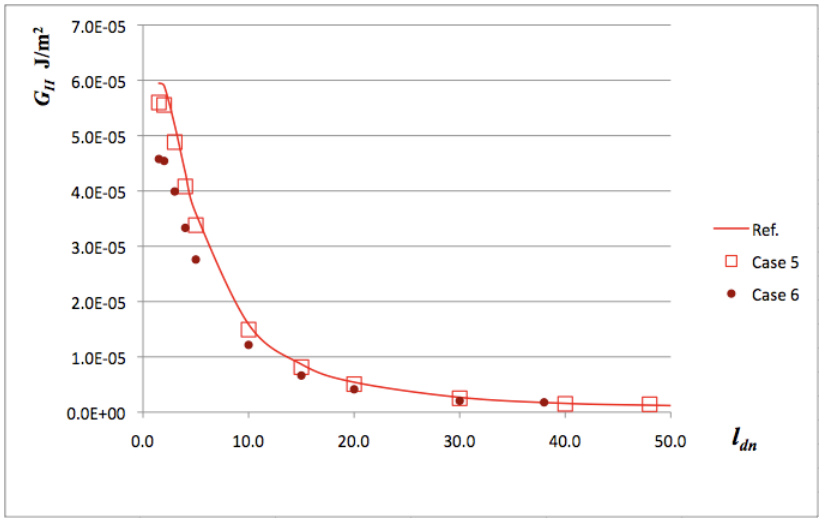


Fig.4.9. $G_{II}$ calculation results showing significance of fiber radius $r_f$. Cases according to Table 4.1

The significance of fiber elastic modulus $E_f$ was studied by varying it within the reasonable range: as shown in Table 4.1, values of 210, 200 and 220 GPa were used in reference, Case 7, and Case 8 respectively which is a narrow, but a realistic range of elastic modulus of steel. Therefore the significance of fiber elastic modulus $E_f$ on $G$ is also difficult to evaluate from results presented in Fig.4.10 and 4.11. In fact, the significance of elastic modulus on $G$ is quite significant since $G$ changes linearly with $E_f$. This trend has also been observed in [85]. This linear trend can also be very useful to recalculate $G$ for different fiber/matrix systems.

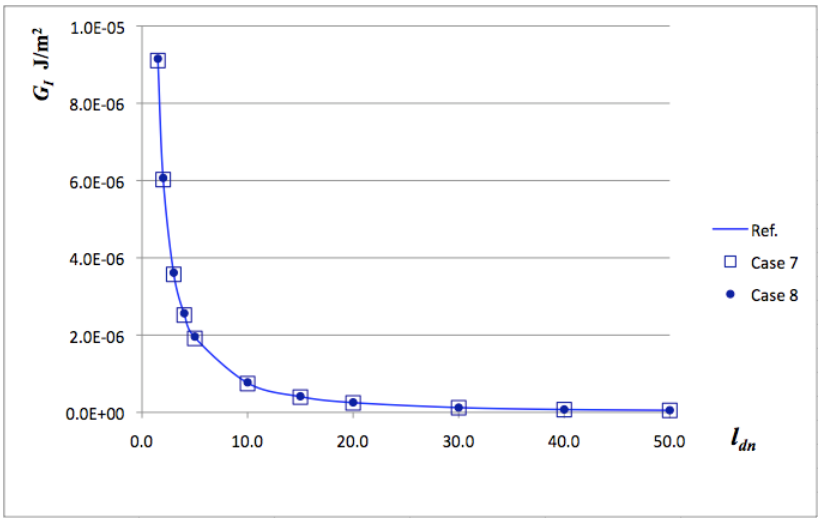


Fig.4.10. $G_I$ calculation results showing significance of fiber modulus $E_f$. Cases according to Table 4.1

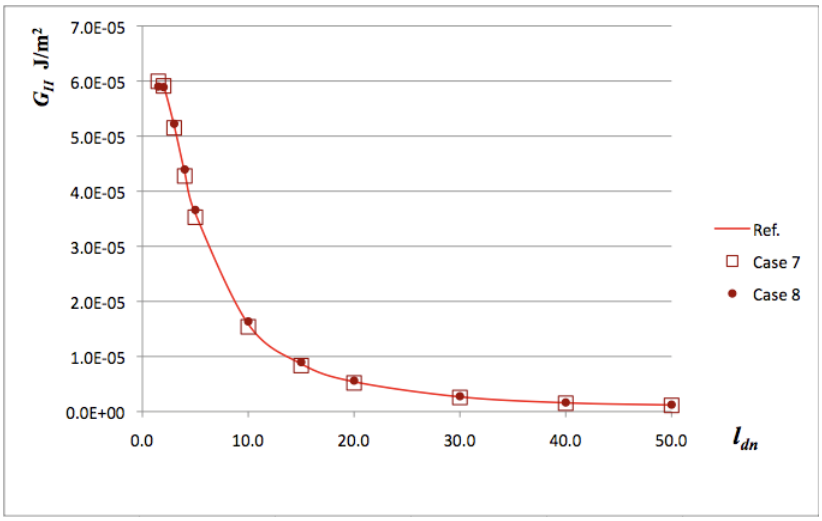


Fig.4.11. $G_{II}$ calculation results showing significance of fiber modulus $E_f$. Cases according to Table 4.1

According to the obtained results, the energy release rate $G$ increases with the increase in $E_f$.

The significance of concrete matrix elastic modulus $E_m$ according to the results demonstrated in Fig.4.12 and 4.13 also is quite high. Matrix modulus were 30, 35 and 25 GPa for reference, Case 9 and Case 10 respectively and notably higher changes in $G$ are seen compared to changes in fiber elastic modulus $E_f$. Although the range of observed matrix moduli $E_m$ was actually relatively wider than the range of $E_f$, it was observed that both $G_I$

and $G_{II}$ are more sensitive to concrete matrix modulus since in the model the volume fraction of concrete matrix is much higher than for the steel fiber.

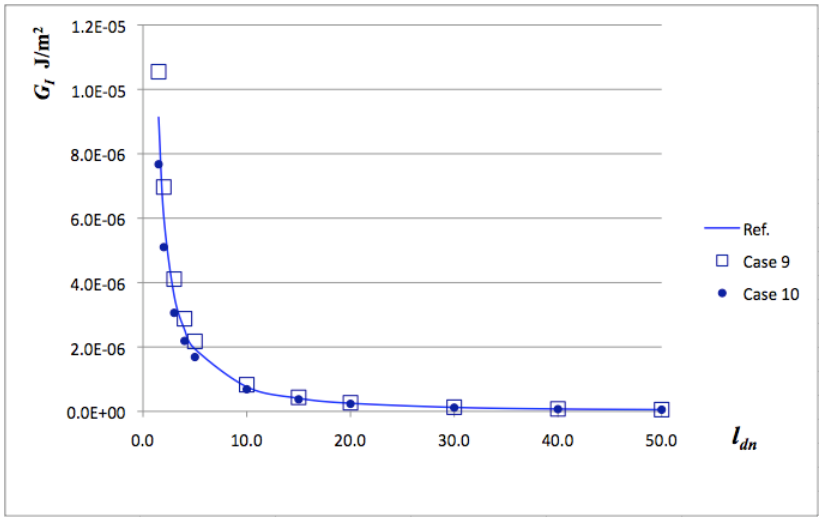


Fig.4.12. $G_I$ calculation results showing significance of concrete matrix modulus $E_m$. Cases according to Table 4.1

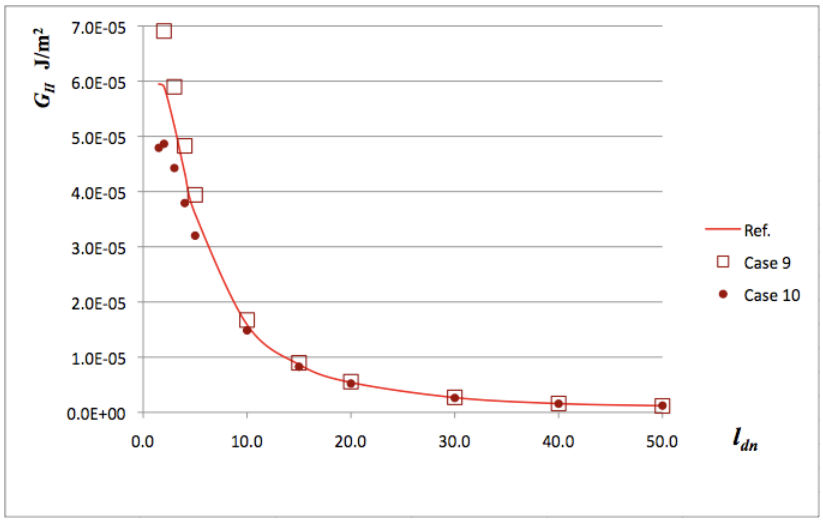


Fig.4.13. $G_{II}$ calculation results showing significance of concrete matrix modulus $E_m$. Cases according to Table 4.1

Similarly to fiber elastic modulus also the concrete matrix was observed to have a linear relation on both $G_I$ and $G_{II}$. Higher elastic modulus of the matrix $E_m$ results in higher stresses and hence higher values of $G$ are obtained.

Parametric analysis results showing significance of fiber Poisson's ratio $\nu_f$ are presented in Fig.4.14 and 4.15. Notable difference from previous parameters is that $\nu_f$ has a lot more

influence on Mode I energy release rate $G_I$ than on Mode II energy release rate $G_{II}$ where it can be considered as non-significant.

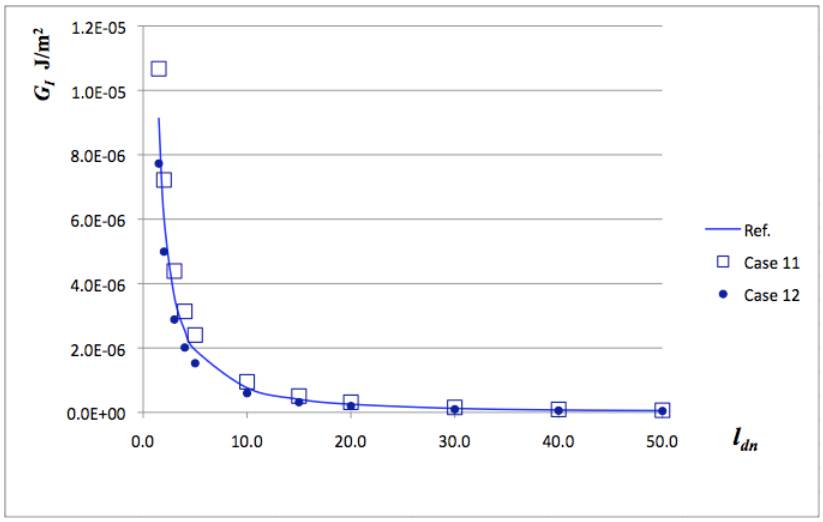


Fig.4.14. $G_I$ calculation results showing significance of fiber Poisson's ratio $\nu_f$. Cases according to Table 4.1

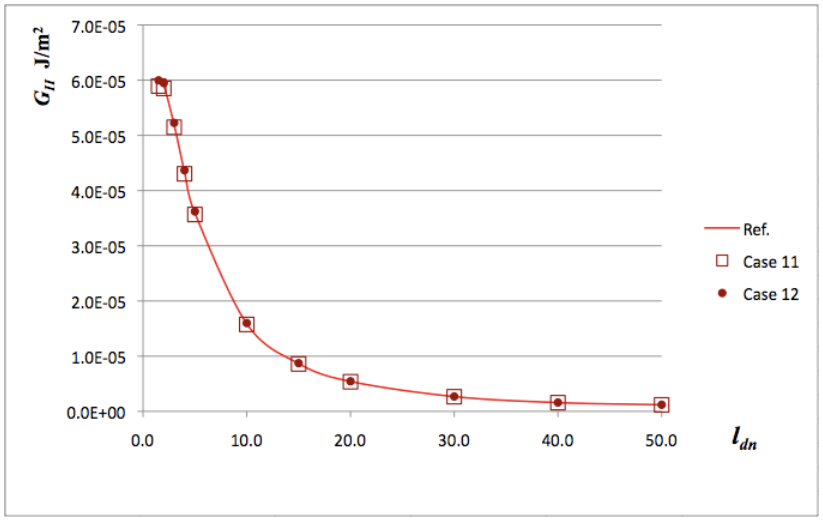


Fig.4.15. $G_{II}$ calculation results showing significance of fiber Poisson's ratio $\nu_f$. Cases according to Table 4.1

This is an expected result since it was described earlier that due to larger contraction of fiber compared to matrix contraction, i.e., $\nu_f > \nu_m$, Mode I crack propagation also occurs.

The results logically show a decrease of $G_I$ when fiber Poisson's ratio is decreased while even higher Poisson's ratio of fiber will cause even higher contribution of Mode I. In Case 11 $\nu_f = 0.35$, Case 12 $\nu_f = 0.25$. The opposite then is true if concrete matrix Poisson's ratio is

increased (as in Case 13, where $\nu_m = 0.25$) or decreased (as in Case 14, where $\nu_m = 0.15$) as proved in Fig.4.16 and 4.17.

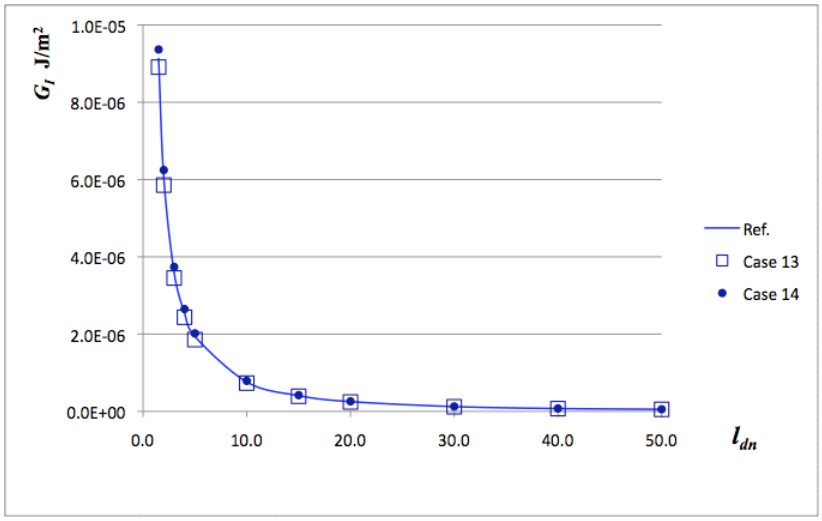


Fig.4.16. $G_I$ calculation results showing significance of concrete matrix Poisson's ratio $\nu_m$. Cases according to Table 4.1

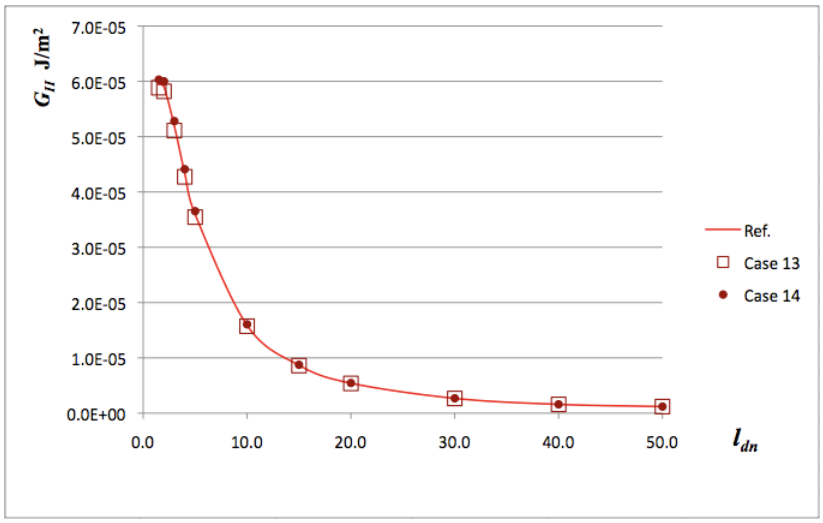


Fig.4.17. $G_{II}$ calculation results showing significance of concrete matrix Poisson's ratio $\nu_m$. Cases according to Table 4.1

Finally, parametric analysis results for significance of residual stresses is presented in Fig.4.18 and 4.19. As it was described before, thermal analogy was used to simulate formation of residual shrinkage stresses in concrete matrix. It could be expected that a negative temperature change $\Delta T < 0$ will cause the matrix to shrink and suppress the embedded fiber. However, if the debond is present like in the model used here, then applying

a negative temperature change can actually have the opposite effect – due to shrinkage of matrix block Mode I crack opening is actually enhanced.

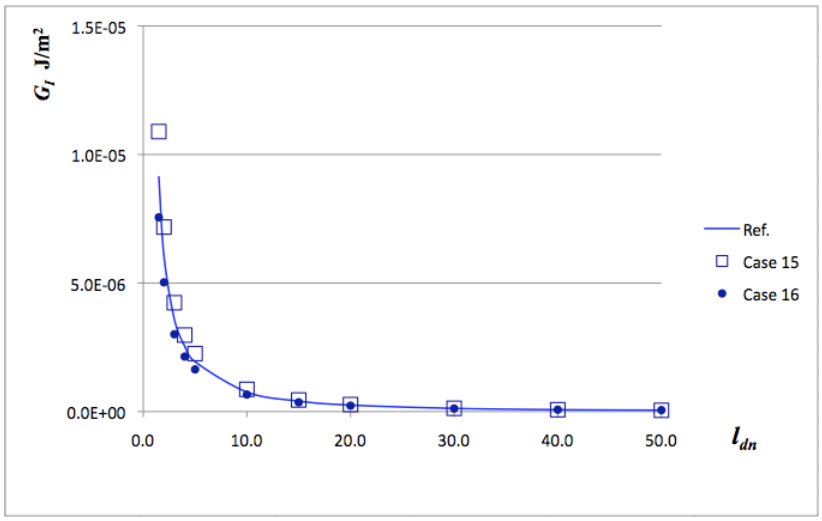


Fig.4.18. $G_I$ calculation results showing significance of initial temperature change $\Delta T$ in concrete matrix. Cases according to Table 4.1

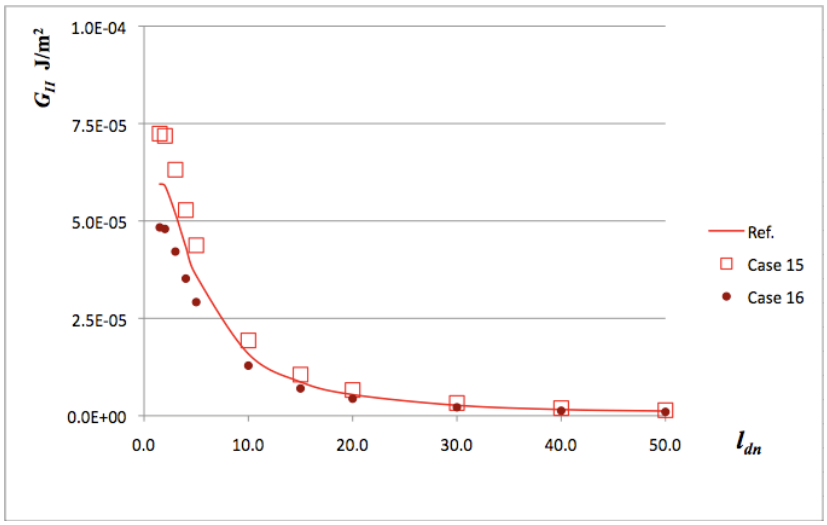


Fig.4.19. $G_{II}$ calculation results showing significance of initial temperature change $\Delta T$ in concrete matrix. Cases according to Table 4.1

In that case a positive temperature change $\Delta T > 0$ could actually be applied in order to reduce contribution of Mode I. That, however, is not a realistic representation of the shrinkage phenomenon. The results in Fig.4.18 and 4.19 actually indicating that both $G_I$ and $G_{II}$ decrease with a positive temperature change $\Delta T > 0$ (Case 16). This means that Mode I can not be really eliminated by the thermal analogy approach used here. Alternative would be to use contact pressure applied on the interface but then the model becomes more complicated.

In section 4.2., where a complete fiber pull-out process was modelled the residual stresses were included in analysis by interference fit approach.

Generally, the parametric analysis performed in this section demonstrated that only Poisson's ratios $\nu_f$ and $\nu_m$ affect Mode I and Mode II independently. The best way to eliminate the Mode I opening of the debond crack would be to use fiber and matrix with as close Poisson's ratios $\nu_f$ and $\nu_m$ as possible.

### 4.1.4. Debond growth simulations and fiber pull-out law during debonding stage

Although it was shown in the previous parametric analysis that Mode I crack propagation can be significant for short debond lengths, the overall results presented in the previous sub-section showed Mode II crack propagation domination in the fiber pull-out process. Even if the Mode I would be eliminated by a proper inclusion of residual stresses, the trends obtained for Mode II energy release rate $G_{II}$ would still be in power.

The results of parametric analysis also showed negligible influence of fiber and matrix Poisson's ratio and fiber embedded length $l_f$ on $G_{II}$. The relation between $G_{II}$ and fiber radius $r_f$ as well as fiber and matrix elastic modulus $E_f$ and $E_m$ was found to be linear. For the given system fiber modulus $E_f$ is an order of magnitude higher than the concrete matrix modulus $E_m$ therefore the amount of energy released from the fiber cylinder is expected to be larger. However the volume fraction of fiber compared to matrix is small, therefore both $E_f$ and $E_m$ influence the values of $G_{II}$.

Thus, by neglecting contribution of Mode I crack propagation and keeping in mind that in linear elastic fracture mechanics energy release rate $G$ is a quadratic function of the applied strain and hence also the applied displacement $u_z$ (for a system with constant length $l_{sum}$) Mode II energy release rate $G_{II}$ can be written in expression:

$$G_{II} = k_m E_f r_f (u_z)^2 \tag{4.7}$$

where $k_m$ is a coefficient related to mechanical response of the system. Knowing this coefficient would allow us to calculate the energy release rate $G_{II}$ for any arbitrary mechanical loading case (i.e., arbitrary value of $u_z$). Since in Eq.(4.7) fiber elastic modulus $E_f$ and radius $r_f$ are in open form, $G_{II}$ can be calculated also for any arbitrary fiber modulus and aspect ratio. Coefficient $k_m$ obviously also includes the elastic modulus of the matrix $E_m$

since linear relation was observed from the parametric analysis. However, in the present study it was decided not to use $E_m$ in an open form, because then it would demand to include the size or volume fraction of matrix as well.

In fact, since values of $G_{II}$, $E_f$, $r_f$ and the applied displacement $u_z$ for the reference case are known (see Table 4.1), calculation of coefficient $k_m$ is straightforward:

$$k_m = G_{II} \Big/ \left[ E_f r_f (u_z)^2 \right] \tag{4.8}$$

The value of the coefficient for the reference case was equal to $k_m = 6.0592 \cdot 10^{-4}\ 1/m^2$.

For the present study it was decided that it would be more convenient to use the mechanical load in a form of applied displacement $u_z$ instead of applied strain because the pull-out law, i.e., $F_z(u_z)$ will be later derived for the debonding stage of fiber pull-out process.

So, Eq.(4.7) gives the value of Mode II energy release rate for any applied axial displacement $u_z$. However, as it was proved in the previous sub-section (see Fig.4.4), $G_{II}$ significantly depends on the debond length $l_d$. For the further debond growth simulations and derivation of fiber pull-out law, it would be convenient to describe this variation of $G_{II}$ by a simple mathematical expression. For this reason one can assume that the Mode II energy release rate for fully debonded fiber is equal to $G_{II,l_f}$. In the reference case (see Table 4.1), for example, it could be assumed that $G_{II,l_f}$ corresponds to normalized debond length equal to $l_{dn} = 50$. $G_{II}$ for shorter debond lengths as seen in Fig.4.4. is higher and thus the magnification coefficient $k_m^*$ can be introduced as:

$$G_{II} = k_m^* \left[ k_m E_f r_f (u_z)^2 \right] \tag{4.9}$$

where $k_m^*$ is obviously a function of debond length $l_{dn}$. It has been shown that one can fit magnification of debond crack growth related energy release rate with an exponential [86] or hyperbolic [92] function.

In the current study exponential type of magnification function $k_m^*(l_{dn})$ was used in form of:

$$k_m^* = 1 + a \cdot e^{-b \cdot l_{dn}} \tag{4.10}$$

where $a$ and $b$ are fitting parameters to be found. Eq.(4.10) is written for the case, when the energy release rate $G_{II}$ is normalized with respect to energy release rate of a fully debonded fiber, i.e.:

$$k_m^*(l_{dn}) = G_{II}(l_{dn}) / G_{II,l_f} \tag{4.11}$$

Thus, when the normalized debond length $l_{dn}$ is small, values of magnification coefficient $k_m^*$ are higher and when $l_{dn} = l_f$, the value of $k_m^*$ is equal to 1.

Values of $k_m^*$ were calculated for several normalized debond lengths and thus the fitting parameters could be found by taking logarithm of Eq.(4.10):

$$\ln(k_m^* - 1) = \ln(a) - b \cdot l_{dn} \tag{4.12}$$

Linear fit of Eq.(4.12) is shown in Fig.4.20.

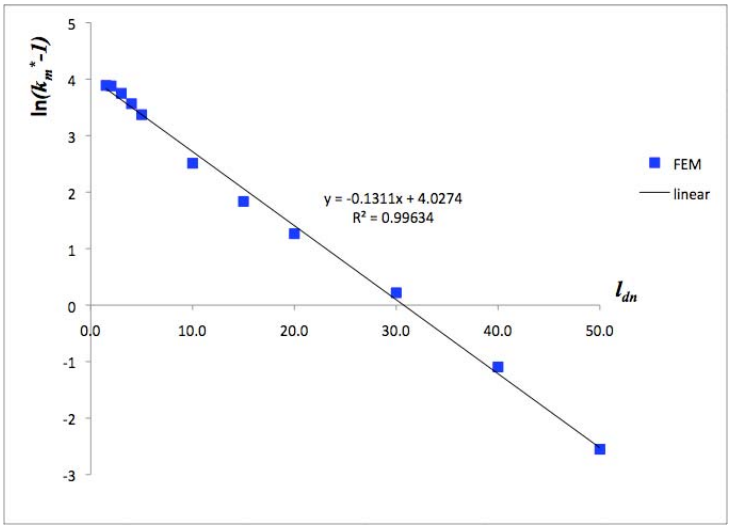


Fig.4.20. Linear fit of Eq.(4.12)

As it can be seen in Fig. 50, a good linear fit can be obtained for Eq.(4.12) and fitting parameters can be easily extracted from it.

The values of fitting parameters $a$ and $b$ for the reference case are presented in Table 4.2.

The resulting agreement between magnification coefficient $k_m^*(l_{dn})$ calculated by FEM with the predicted values using Eq.(4.10) is shown in Fig.4.21.

As it can be seen in the Fig.4.21., a very good agreement is obtained.

The same type of exponential function as in Eq.(4.9) can be used to comprise the magnification of reaction force $F_Z$ (see Fig.4.5) as a function of the normalized debond length. The magnification of reaction force $F_Z$ for short debond lengths is defined as $m^*$:

$$F_Z = m^* \cdot F_{Z,lf} \tag{4.13}$$

where $F_{Z,lf}$ is the reaction force corresponding to fully debonded fiber. Similarly as for magnification of $G_{II}$ in Eq.(4.10), the reaction force corresponding to the fully debonded fiber is assumed at $l_{dn} = 50$ (see Fig.4.5). The function describing the magnification of the reaction force $F_Z$ is then:

$$m^* = 1 + c \cdot e^{-d \cdot l_{dn}} \tag{4.14}$$

where $c$ and $d$ are fitting parameters.

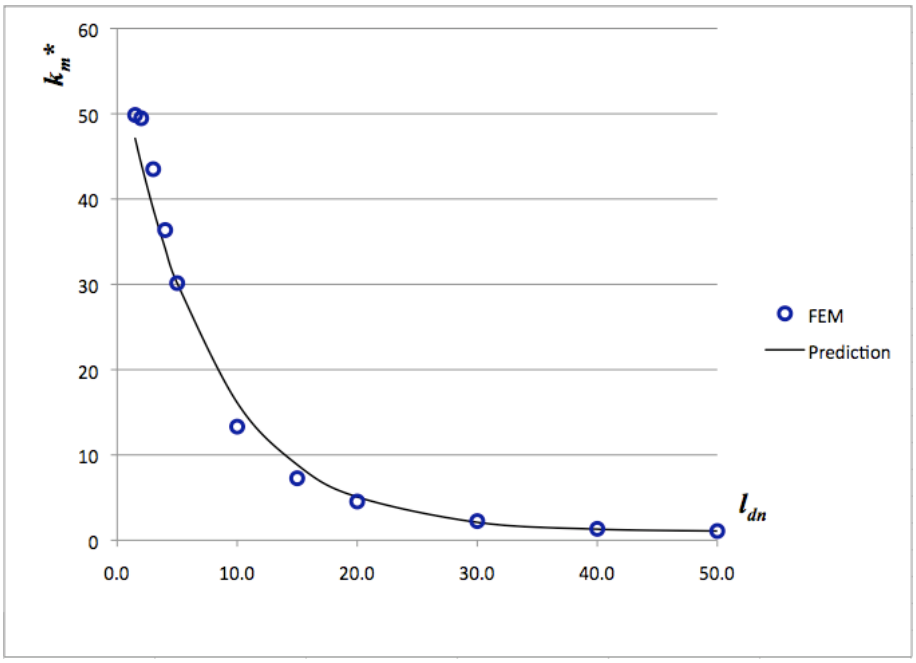


Fig.4.21. Magnification coefficient $k_m^*(l_{dn})$. FEM calculations and prediction.

Using the same procedure as in Eq.(4.12), logarithm was taken from Eq.(4.14) and the parameters were found from the best linear fit. The resulting agreement between FEM calculations and prediction using Eq.(4.14) is very good and it is shown in Fig.4.22.

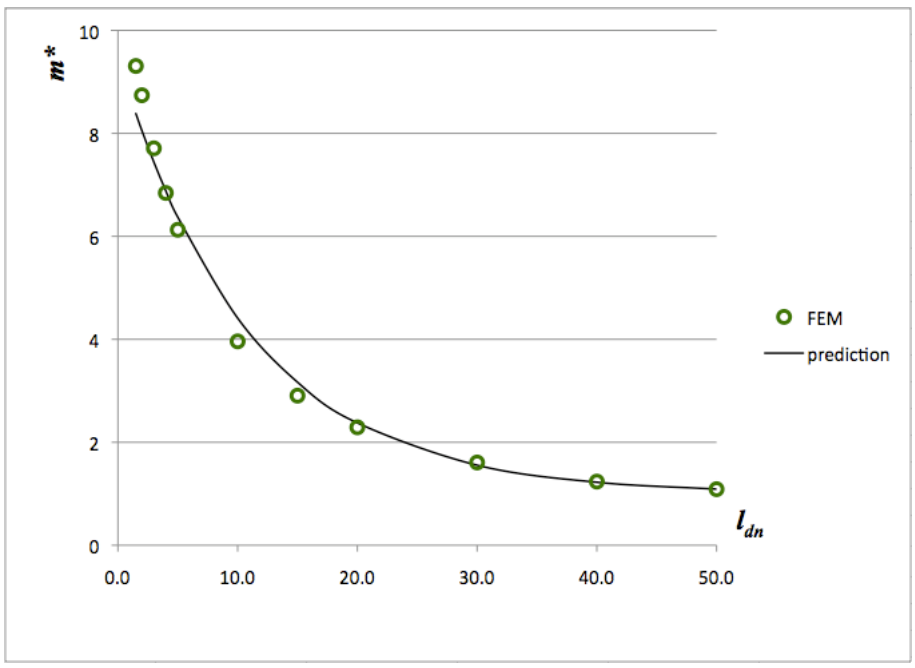


Fig.4.22. Magnification coefficient $m^*(l_{dn})$. FEM calculations and prediction

The values of fitting parameters $c$ and $d$ are given in Table 4.2.

Table 4.2.

Values of fitting parameters for Eq.(4.10), Eq.(4.14) and Eq.(4.16)

| $a$ | $b$ | $c$ | $d$ | $f$ |
|---|---|---|---|---|
| 56.1148 | 0.1311 | 0.0908 | 8.460 | 4619258 |

So now simple expressions have been obtained to describe magnification of Mode II energy release rate $G_{II}$ and the reaction force $F_Z$. This allows us to derive expressions for debond growth simulations and the fiber pull-out law $F_z(u_z)$ during interface debonding stage.

Debond growth simulations can be performed using Eq.(4.9) assuming that the crack propagates when the critical value of energy release rate $G_{IIc}$ (also known as the fracture toughness) is reached in the system. The fracture toughness $G_{IIc}$ is a material property and thus is not affected by the debond crack growth.

Combining Eq.(4.9) and Eq.(4.10) we obtain:

$$u_z = \sqrt{G_{IIc} \Big/ \left[k_m (1 + a \cdot e^{-b \cdot l_{dn}})\right]} \tag{4.15}$$

Eq.(4.15) basically gives relation between the displacement of the fiber as a function of normalized debond length $l_{dn}$. Simulations were performed by choosing a fixed fracture toughness value $G_{IIc}$, incrementing the debonded length $l_{dn}$ and calculating the corresponding fiber displacement using Eq.(4.15). The obtained relation can then be translated actually as the increase of debond with the applied fiber displacement.

Debond growth simulations for 4 different cases are presented in Fig.4.23.

Four different values of $G_{IIc}$ were used in debond growth simulations: $G_{IIc} = 10 \cdot 10^{-6}$, $8 \cdot 10^{-6}$, $6 \cdot 10^{-6}$ and $4 \cdot 10^{-6}$ $J/m^2$. According to simulation results in Fig.4.23. higher interface fracture toughness $G_{IIc}$ means that higher displacement $u_z$ has to be applied in order to cause propagation of the debond crack. It can also be observed from the results in Fig.4.23. that if a displacement is incremented linearly as in a displacement controled fiber pull-out test, the debond growth rate is higher for short debond lengths and near the complete debonding while in the medium debond lengths the debond crack growth rate is linear. This observation can be explained with the interaction between debond crack and matrix crack at short debond lengths and interaction with the end of embedded fiber for long debond lengths.

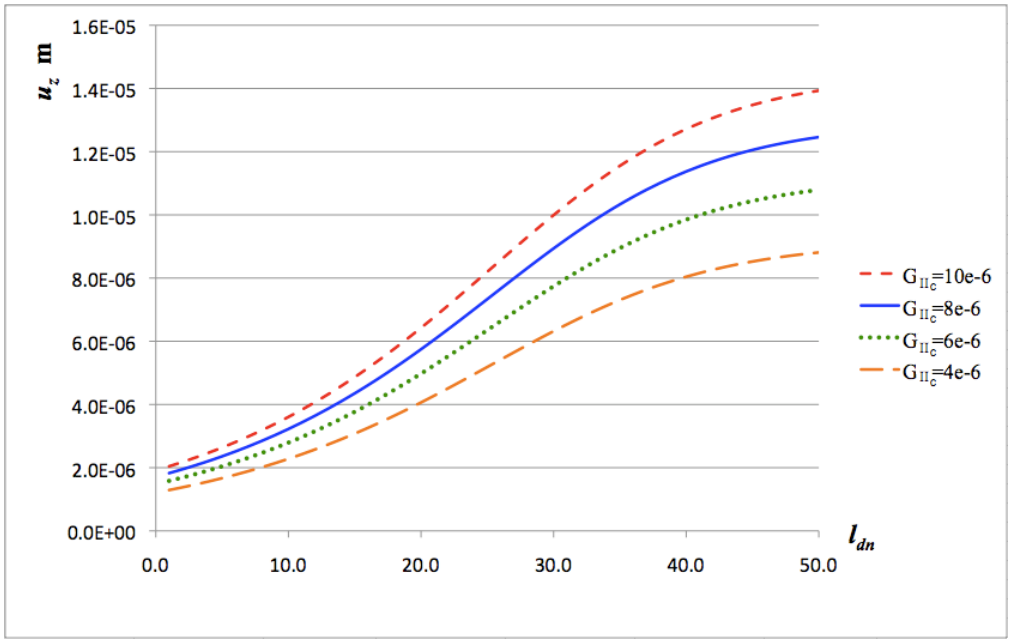


Fig.4.23. Debond growth simulations for various cases. $G_{IIc}$ values in calculation examples given in $J/m^2$

Finally, the pull-out law – the relation between applied force and the resulting displacement – for the stage of debonding can be derived. It is obvious that in a linear elastic fracture mechanics problem the reaction force $F_Z$ is linearly related to the applied displacement $u_z$:

$$F_Z = f \cdot u_z \tag{4.16}$$

where $f$ is linear slope coefficient.

For the reference case (see Table 4.1) the calculated value of coefficient $f$ is presented in Table 4.2. However, the reaction force $F_Z$ was earlier shown to significantly depend on the debond length (Fig.4.5). Thus, it must be concluded that the reaction force is a function of both the applied displacement $u_z$ and the debond length $l_{dn}$. Assuming that the reaction force in Eq.(4.16) is the one corresponding to fully debonded state, i.e., $F_{z,lf}$, the following relation can be written by combining Eq.(4.14) and Eq.(4.16):

$$F_z(l_{dn}) = f \cdot u_z \cdot m^*(1 + c \cdot e^{-d \cdot l_{dn}}) \tag{4.17}$$

Thus inserting Eq.(4.15) in Eq.(4.17) the pull-out law for a general debonding case can be written as:

$$F_z(l_{dn}) = f \cdot \sqrt{G_{IIc} \Big/ \left[k_m(1 + a \cdot e^{-b \cdot l_{dn}})\right]} \cdot m^*(1 + c \cdot e^{-d \cdot l_{dn}}) \tag{4.18}$$

Similarly as with debond growth, simulations of fiber pull-out law were performed for different values of Mode II fracture toughness $G_{IIc}$.

The modelled pull-out curves were validated with FEM calculations for each case and a good agreement was obtained as demonstrated in Fig.4.24.

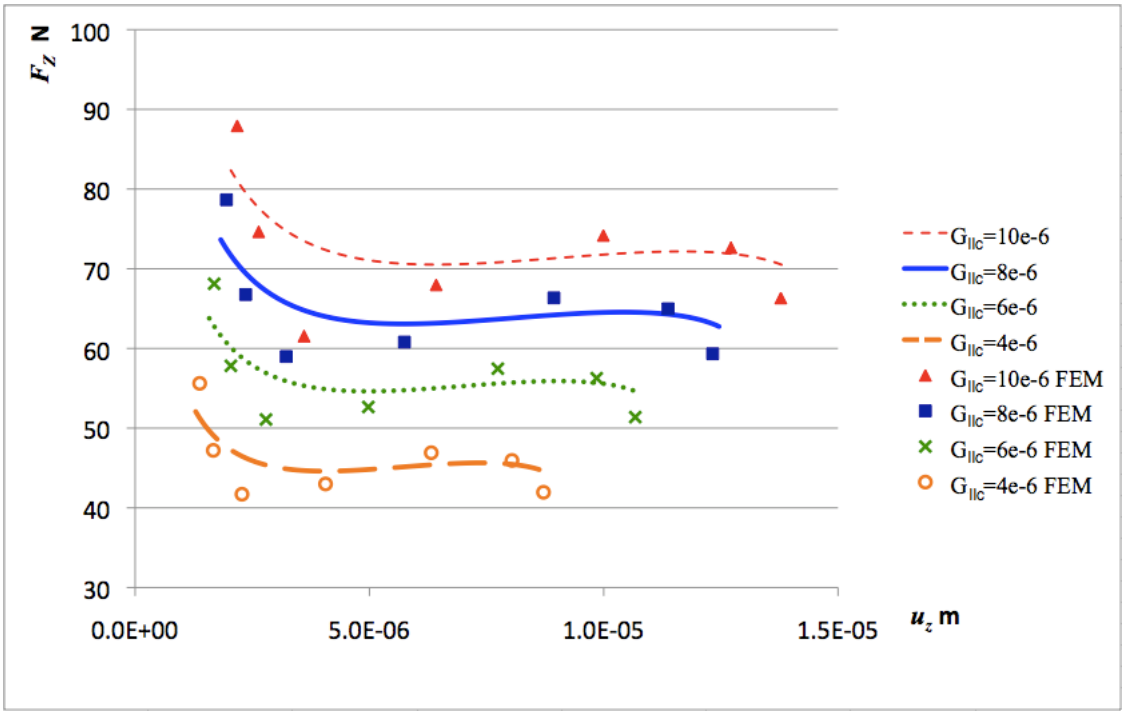


Fig.4.24. Modelled fiber pull-out law curves for different cases with FEM validation. $G_{IIc}$ values in calculation examples given in $J/m^2$

As it can be seen from the curves in Fig.4.24. the pull-out load significantly decreases at the early debonding stages due to large amount of released energy. The reaction force $F_z$ drops down until the linear debond growth region is achieved during which the reaction force generally is weakly increasing. The final stage is when the full debonding of fiber is approaching, which results in another significant decrease of $F_z$ as it is evident in Fig.4.24.

An obvious trend of the results is that the higher the fracture toughness $G_{IIc}$, the higher is the reaction force $F_z$. Fig.4.24. actually shows that $G_{IIc}$ and hence interface properties have a large influence on the pull-out load. These results indicate the necessity to improve steel fiber concrete matrix interface bonding as the pull-out resistance can be significantly increased.

Unfortunately, a direct comparison with experimental results was not possible since the experimental tests were carried out at displacement rate $\Delta u = 10$ mm/min and the detailed pull-out curve in debonding stage could not be experimentally recorded since the propagation

of the debond crack probably occured instantly. In the experimental measurements performed in this study probably only the maximal value of reaction force during the debonding was recorded.

Nevertheless, if we consider the maximal recorded pull-out load values from the experiments (samples B4F3, B4F7, B4F10, B4F13) then the range is between 30 and 120 N. Comparing the results presented in Fig.4.24. it can be seen that the maximum reaction forces for different cases are in a range between 50 and 90 N. So, although accurate and exact value of fracture toughness $G_{IIc}$ for the experimental samples can not be determined from the best fit, a general comparison with the modelling results allows to conclude that the order of magnitude of $G_{IIc}$ for the experimentaly tested samples is between $10 \cdot 10^{-6}$ to $4 \cdot 10^{-6}$ $J/m^2$. It has to be concluded that these values are really small compared to polymer composite interfaces where interface fracture toughness $G_{IIc}$ around 200 $J/m^2$ has beeen reported [87].

Generally, the model proposed here is a convenient tool to analyze the debond crack propagation and obtain the pull-out law of fiber during the debonding stage. The required parameters and coefficients can be calculated simply and if experimental data in form of a pull-out curve are available, the Mode II fracture toughness $G_{IIc}$ can be found.

## 4.2. Modelling of complete fiber pull-out

In the previous sub-section (4.1) the numerical calculation results were showing that mixed mode (Mode I and Mode II) debond crack propagation can occur. Although it was shown that Mode II crack propagation is dominating for all the studied cases it is important to remember that no initial stresses induced by concrete shrinkage were taken into account in debond growth simulations and fiber pull-out law modelling. While the parametric analysis performed and presented in the previous sub-section and the significance of all parameters is still relevant and could be used to analyze propagation of debond crack, the inclusion of the initial stresses into the analysis certainly would decrease or eliminate contribution of Mode I (since the stresses on fiber surface would be compressive, decreased or no Mode I opening could occur) depending, of coarse, on the magnitude of the shrinkage. Simulation of initial shrinkage stresses using thermal expansion analogy and applying mechanical pull-out load for the 2-D model in the previous section showed that Mode I crack propagation cannot be eliminated, even when relatively high and probably unrealistic thermal contraction was used in calculations. However, the observations from many cases in literature [82] as well as from the experimental part of the current study show that the Mode I is eliminated completely meaning that even after complete debonding of the fiber, the stresses on the fiber surface always remain compressive. This is well demonstrated in the experimental results (see Chapter 3), which still show a significant and generally stable pull-out resistance of fiber at the pull-out stage after complete debonding and after the peak load has been achieved. Haven't the compressive radial stresses existed, the straight and aligned fibers would pull out quite easily after completion of debonding judging from Poisson's effect for the given system, i.e., $\nu_f > \nu_m$. Since Poisson's ratio is higher for the fiber there will be a larger contraction of fiber compared to matrix giving rise to low and rather unstable pull-out resistance during the stage after complete interface debonding.

This generally means that the 2-D model, which was previously used for $G$ calculations, would not be applicable to study the pull-out process after completion of interface debonding along the whole fiber length.

Therefore, in this section a complete pull-out of fiber is modelled by a 3-D model including the initial residual shrinkage stresses in form of initial interference fit problem and employing contact elements. This basically means that the initial shrinkage stresses in the system, which induce compressive radial stresses on the fiber surface are applied by defining fiber with the exact diameter and length while the concrete matrix block is defined with a

certain cavity (cylindrical hole), which is by small unit smaller to fit in the given fiber geometry. The geometrical representation of such problem is shown in Fig.4.25.

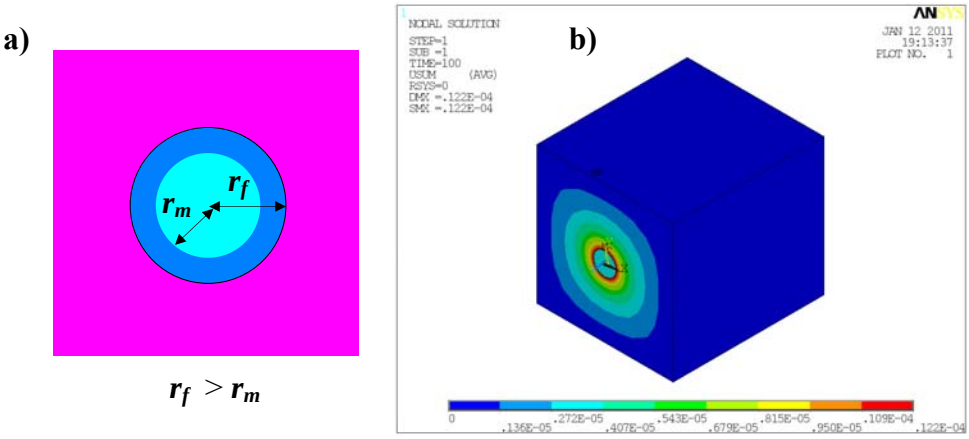


Fig.4.25. Interference fit of embedded fiber: a) geometrical representation where $r_f$ is fiber radius while $r_m$ is radius of the cylindrical cavity in matrix; b) von Mises stress distribution calculated by FEM contact element analysis

The interference fit problem is solved as the first load step in form of a contact analysis. According to surface-to-surface contact analysis procedure in ANSYS software [84], the corresponding concrete face is defined as a contact surface with flexible characteristics while the corresponding fiber face is defined as the target surface with rigid characteristics. Thus during the first step of analysis the concrete matrix is forced to correspond to the given fiber diameter, i.e., $r_m = r_f$, and a certain degree of compressive stresses are formed on the contact surface. As shown in Fig.4.25.b, where von Mises stress plot is presented after solution of load step 1 (interference fit), the compressive stresses form in the concrete matrix block also deforming the fiber in the process by a certain value which is not considered as important in the further analysis.

Although the radial stress distribution in the concrete matrix block from this kind of analysis may not be correct compared to reality, this modelling approach can still be considered as an accurate representation of the shrinkage phenomenon and formation of initial stresses. Obviously the magnitude of these compressive radial stresses acting on fiber surface depends on geometry of the defined interference fit and on the elastic properties of constituents (steel fiber and concrete matrix). The compressive radial stresses on the fiber surface certainly infuluence the pull-out resistance of the fiber through the whole pull-out

process. The complete pull-out of fiber is modelled as the 2nd load step, during which a mechanical pull-out displacement is applied to the fiber end.

Once again, the significance of residual stresses can be studied in detail through a parametric analysis. And since experimental pull-out curves are available (from Chapter 3), the value of the contact pressure for particular cases can be found from the best fit with the experimental results.

Two cases were subdivided in this section: 1) initially debonded fiber/matrix interface and 2) initially bonded fiber/matrix interface. In the first case the bonding strength between fiber and matrix is assumed to be negligible and the largest contribution to pull-out resistance is expected to occur from friction, which is magnified by the residual compression. In the second case the initial bond between fiber and matrix is considered to be significant and is expected to have an influence on the further pull-out resistance of the fiber.

In both of the mentioned cases the calculations were performed in a two step analysis, where first step is always the interference fit solution and the second step is application of pull-out displacement. Both load steps were defined as case of large displacement nonlinear analysis. FEM model and the boundary conditions for the 2nd load step is represented in Fig.4.26.

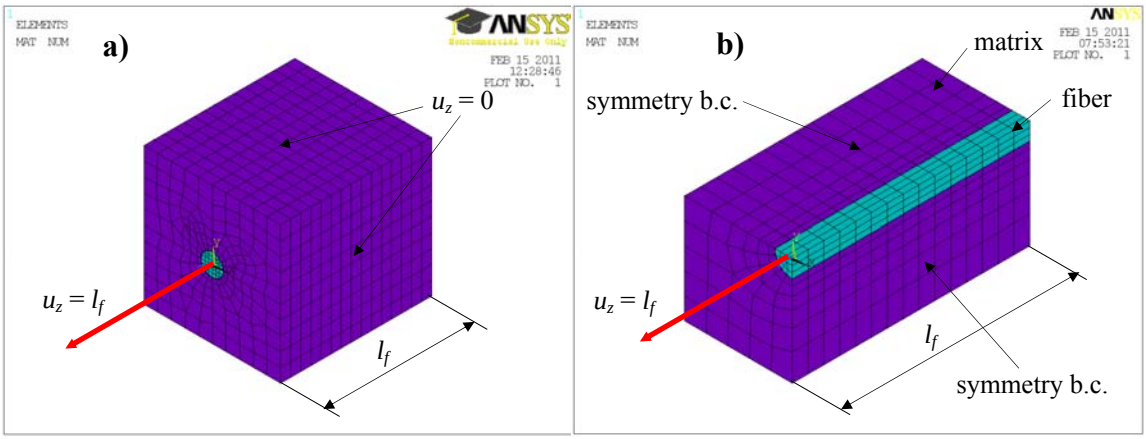


Fig.4.26. 3 D FEM model for complete fiber pull-out: a) full model; b) ¼ model with symmetry boundary conditions

In the following sub-sections a parametric analysis is performed for both initially debonded interface and bonded interface cases and the best fit with experimental results allows extraction of several strength and fracture mechanics parameters.

### 4.2.1. 3-D fiber pull-out problem with initially debonded interface

It has been proved in 2-D analysis in section 4.1. and it is recognized in the literature that the interface properties in steel fiber and concrete matrix system often cannot be considered as significant. Due to the fact that no chemical or mechanical bonding is present, like in the case of straight steel fiber, the initial interface bond strength may not be significant and the initial response to pull-out load of the fiber could only be a result from surface-to-surface friction.

In this sub-section a 3-D modelling of complete fiber pull-out is performed with neglecting the interface bond strength properties. A comparison with the experimental results would later show, whether this assumption of initially debonded interface can be reasonable.

The FEM model representing the current problem is shown in Fig.4.26. As it is shown in the picture, symmetry boundary conditions can be employed and only ¼ of the total volume was used, thus saving calculation time for this non-linear analysis. During the first load step only symmetry boundary conditions are applied on the symmetry planes. The second load step is defined as an axial constraint that is applied on the outer surface and axial (pull-out) displacement on the fiber exit point (see Fig.4.26.b).

Compared to 2-D FEM model used in previous section (Fig.4.2) it is notable from Fig.4.26. that model equal to fiber embedded length $l_f$ is used instead of model length $l_{sum}$, which corresponds to experimental samples. It was considered that because even the radial interface between steel fiber and concrete matrix is unlikely to have a high bond strength, the interaction between thin embedded fiber end and the concrete matrix may as well be neglected, especially if fiber pull-out stage is analyzed.

Furthermore, large displacement non-linear calculations usually are time consuming and require more computational resources, therefore less modelled volume is beneficial.

So, solving the 1st load step gives rise to formation of compressive radial stresses on the fiber surface and hence initial residual stresses can be modelled. The von Mises stress distribution for 1st load step solution was already demonstrated in Fig.4.25.b. For the 2nd load step an axial displacement equal to embedded fiber length, i.e., $u_z = l_f$ is applied. Because of the compressive stresses acting on the fiber surface the applied displacement is counteracted by a reaction force.

In the modelling software ANSYS [84] the solution of 2nd load step was divided into at least 20 substeps and reaction forces (opposite to the applied pull-out load) at each sub-step were calculated. Thus the fiber pull-out law $F_z(u_z)$ was numerically calculated. The sequence of complete fiber pull-out and the von Mises stress distribution at various stages for the case with initially debonded interface is illustrated in Fig.4.27.

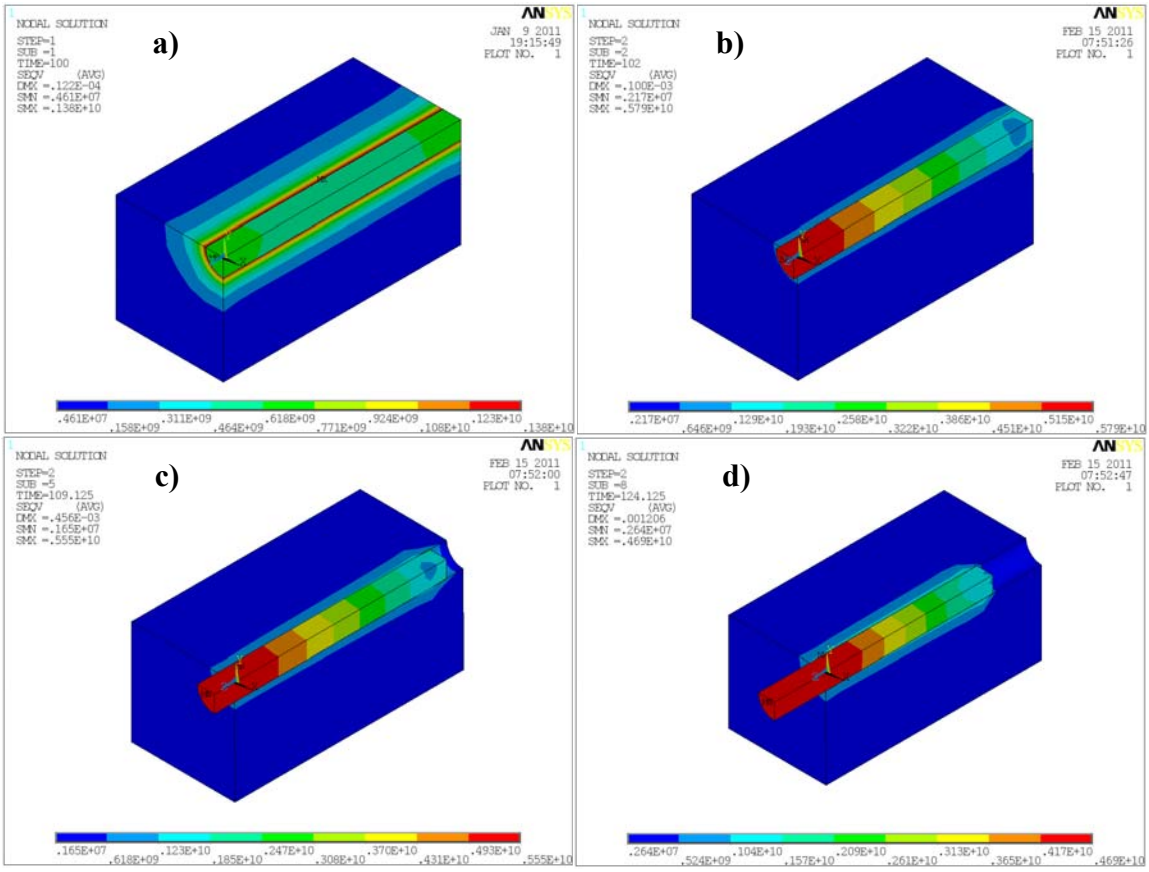


Fig.4.27. Von Mises stress distribution during various stages of the fiber pull-out for the initially debonded interface case: a) residual stresses before beginning of pull-out; b), c), d) fiber pull-out sliding with friction resistance

Fig.4.27.a. shows the distribution of residual stresses while in Fig.4.27.b, c, d von Mises stress distribution during the pull-out movement is shown. As expected, stress relaxation in matrix occurs following the pull-out of fiber.

### 4.2.2. 3D problem with initially bonded interface

Several experimental results for straight fibers (see Chapter 3) showed rather different characteristics of the pull-out curves between samples of the same configuration. In some

cases sharp, distinct peaks with maximal pull-out load were observed in the initial part of pull-out curves. However, in some cases the presence of the peaks was not clearly evident. The occurance of "smooth" pull-out curves corresponds well with the modelling results obtained from the model described in the previous sub-section (4.2.1), where initial bond strength of the fiber/matrix interface was neglected. As it is shown further in section 4.2.3, for the case of debonded interface the modelling results showed almost linear decrease of the pull-out load as the pull-out displacement and the length of the pulled-out section of the fiber increased.

To give answer to question why the experimental curves differed from each other in the initial part of pull-out, one of the explanations could, of coarse, be misalignment in the experimental samples since they were hand manufactured. The other explanation could be that probably initial bond strength is higher in some samples.

In this sub-section 3-D modelling of complete fiber pull-out process is performed for cases, where initial bonding between fiber and matrix is present. Debonding of interface is first necessary in order for the pull-out to occur. Therefore, debonding was included in the model described here.

A parametric analysis was performed to analyze the significance of value of bond strength and how it affects the pull-out response of the fiber.

The calculation was again performed in 2 steps, where the 1st load step corresponds to formation of initial residual stresses (see Fig.4.25) and during the 2nd load step a pull-out displacement $u_z = l_f$ was applied to the fiber.

FEM software ANSYS [84] allows including debonding in the contact analysis for both Mode I and Mode II crack propagation as well as for mixed mode crack propagation conditions. In the current problem only Mode II crack propagation can take place since Mode I is fully eliminated by residual compressive stresses acting on the fiber surface. In ANSYS [84] the debonding can be modelled, using the bilinear cohesive zone material model based on the model proposed in [93]. Other alternative is to use interface elements, however, the bilinear cohesive zone material model is easier to use since it can be adapted to already existing model, such as the model described in previous section 4.2.1. Thus, exactly the same mesh can be used as in the previous model (section 4.2.1) adding only a definition of the third phase (interface) material and specifying the interface strength properties.

According to description provideed in ANSYS [84] software, the equation for the tangential contact stress and tangential slip distance behavior is defined as:

$$\tau_t = K_t u_t (1 - d_t) \tag{4.19}$$

where $\tau_t$ is tangential contact stress, $K_t$ is tangential contact stiffness, $u_t$ is tangential slip distance and $d_t$ is debonding parameter, which is defined as:

$$d_t = \left( \frac{u_t - \overline{u}_t}{u_t} \right) \left( \frac{u_t^c}{u_t^c - \overline{u}_t} \right) \tag{4.20}$$

where $\overline{u}_t$ is tangential slip distance at the maximum tangential contact stress, $u_t^c$ is tangential slip distance at the completion of debonding. For the 3-D stress state an isotropic behavior is assumed in the calculation route and the debonding parameter $d_t$ is calculated by an equivalent tangential slip distance as:

$$u_t = \sqrt{u_1^2 + u_2^2} \tag{4.21}$$

where $u_1$ and $u_2$ are tangential slip distances in the two principal directions in the tangential plane. The respective tangential stress components are calculated according to Eq.(4.19).

The tangential critical fracture energy (Mode II fracture toughness) is calculated according to relation:

$$G_{IIc} = \frac{1}{2} \tau_{\max} u_t^c \tag{4.22}$$

In the modelling procedure performed in this study the bilinear behavior of the cohesive zone material in ANSYS was specified by inputing parameters $\tau_{\max}$ and $u_t^c$. Other alternative could be to specifiy the fracture toughness $G_{IIc}$ instead of tangential slip distance $u_t^c$. However, it is only a matter of input convenience, since Eq.(4.22) can always be used to reaclculate $G_{IIc}$ from $u_t^c$ and vice versa.

Certainly, in order to cause the interface debond sufficient pull-out load has to be applied. Debonding process takes place at the moment, when values of fracture energy $G$ in the modelled interface exceed the fracture toughness value $G_{IIc}$, which in ANSYS [84] is always calculated by Eq.(4.22). According to the boundary conditions applied to the model (see Fig.4.26) maximal interface shear stresses are located at the exit point of the fiber. Thus the debonding initiates at this location and then debond crack propagates along the interface due to stress redistribution until complete debonding has occured. The sequence of fiber pull-out and the von Mises stress distribution at various stages for the case with initial bond strength is illustrated in Fig.4.28.

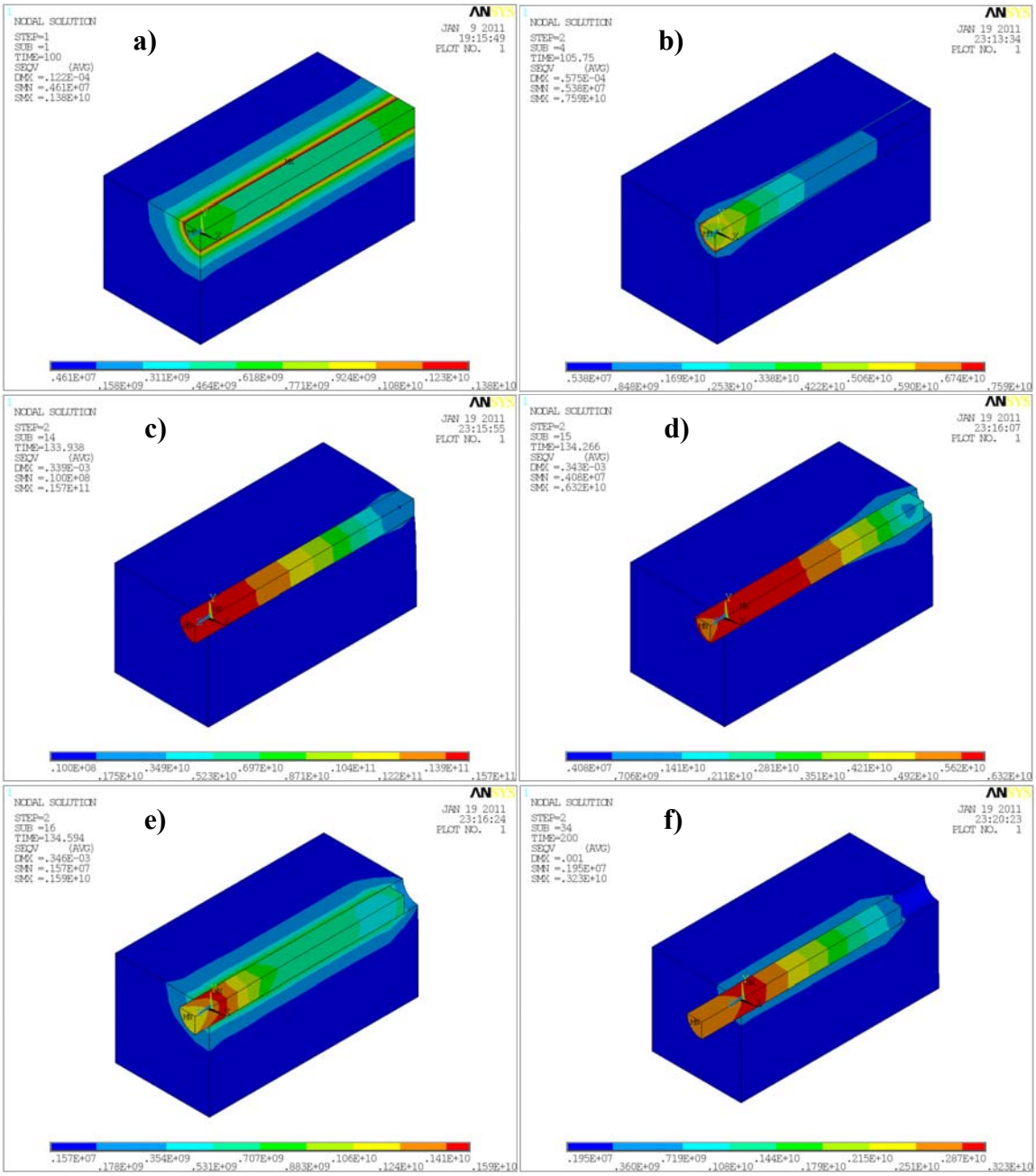


Fig.4.28. Von Mises stress distribution during various stages of the fiber pull-out for the initially bonded interface case: a) residual stresses before beginning of pull-out; b) debond crack initiation at the fiber exit point; c) debond crack propagation along the interface; d) fiber slip by $u_t^c$ after complete interface debonding; e) fiber pull-out slip after completion of debonding; f) fiber pull-out and stress relaxation of the matrix

The formation and distribution of residual stresses is the same as in the previous case, since it does not depend on the interface properties.

According to the model used [93] in ANSYS software [84], after completion of debonding the fiber slips by the specified distance $u_t^c$. Obviously such problem requires mutualy compatible and realistic values of the input parameters $\tau_{\max}$ and $u_t^c$ for a successful solution to be found during calculation. After completion of debonding and fiber slip, the pull-out process continues in the same way as in the case of debonded interface.

The model described in this sub-section is very convenient to use, since 3 different problems – formation of initial stresses, initiation and propagation of debond and fiber pull-out, can be solved in a single calculation procedure.

Once again, in order to calculate the reaction forces and obtain the fiber pull-out law $F_z(u_z)$, the 2nd load step was divided in at least 20 substeps. Because of complexity of such model, the bonded interface solution is more time consuming than the debonded interface case.

### 4.2.3. Modelling results. Parametric analysis

In section 4.1, 2-D Modelling results of fiber pull-out during the debonding stage showed that fiber embedded length $l_f$ does not influence the value of applied load $F_z$ or displacement $u_z$ at which interface debond crack will initiate. The peak load during the debonding stage was proved to depend only on the value of the critical energy release rate (fracture toughness) $G_{IIc}$.

After completion of debonding the pull-out load is resisted only by the residual compressive stresses reacting on the fiber surface. As it was discussed earlier, the Poisson's effect for steel fiber and concrete matrix system does not contribute to provide resistance to pull-out load.

Modelling results for initially debonded case are discussed first. Since the residual compressive stresses act on the whole length (surface) of the fiber, it is expected that longer fibers will therefore have higher resistance and shorter fibers would have lower resistance to pull-out loads. It was confirmed by the experimental results (See Fig.3.10. In Chapter 3) that straight fiber with longer embedded length has the highest value of pull-out load peak value compared to shorter embedded lengths.

In the present section the same four fiber embedded lengths $l_f$ were studied as in the experimental section, i.e., 5, 10, 15 and 20 mm. More detailed parametric analysis was performed for the embedded length $l_f = 5$ mm, however, the best fit with experimental data

was found for all embedded lengths. The tasks of parametric analysis for the case of no initial interface bonding are specified in Table 4.3.

Table 4.3.

Parametric analysis tasks for the case of initially debonded interface

| Case name: | $E_f$ | $E_m$ | $r_f$ | $r_m$ | $p_c$ | $l_f$ | $\mu$ |
|---|---|---|---|---|---|---|---|
| | [GPa] | [GPa] | [mm] | [-] | [MPa] | [mm] | [-] |
| Reference | 210 | 30 | 0.375 | 0.360 | 772.7 | 5 | 0.3 |
| Task 2 | 210 | 30 | 0.375 | 0.360 | 776.0 | 10 | 0.3 |
| Task 3 | 210 | 30 | 0.375 | 0.360 | 777.5 | 15 | 0.3 |
| Task 4 | 210 | 30 | 0.375 | 0.360 | 778.3 | 20 | 0.3 |
| Task 5 | 210 | 30 | 0.375 | 0.365 | 515.8 | 5 | 0.3 |
| Task 6 | 210 | 30 | 0.375 | 0.370 | 255.4 | 5 | 0.3 |
| Task 7 | 210 | 30 | 0.380 | 0.3648 | 772.7 | 5 | 0.3 |
| Task 8 | 210 | 30 | 0.400 | 0.384 | 767.9 | 5 | 0.3 |
| Task 9 | 210 | 30 | 0.375 | 0.360 | 772.7 | 5 | 0.2 |
| Task 10 | 210 | 30 | 0.375 | 0.360 | 772.7 | 5 | 0.1 |
| Task 11 | 220 | 30 | 0.375 | 0.360 | 774.6 | 5 | 0.3 |
| Task 12 | 200 | 30 | 0.375 | 0.360 | 770.7 | 5 | 0.3 |

As it is listed in Table 4.3, the significance of fiber embedded length $l_f$, contact pressure $p_c$, fiber radius $r_f$, coefficient of friction $\mu$ and fiber elastic modulus $E_f$ was analyzed.

Modelling results for different fiber embedded lengths $l_f$ are shown in Fig.4.29. It can be concluded that the pull-out resistance ($F_z$) is linearly dependent on the fiber embedded length $l_f$ and the load is higher for longer embedded lengths. According to Fig.4.29. the initial response before the peak load is reached follows the same curve for all cases. The peak load for longer embedded lengths is thus reached at larger displacements $u_z$ than for shorter embedded lengths.

After reaching the peak load, the values of pull-out load decrease almost linearly in all cases shown in Fig.4.29. until complete pull-out of fiber.

Numerical values of modelling results for $F_z$ in this example are too high to be realistic. However, the objective of this section is to perform parametric analysis and discuss the trends and significance of parameters.

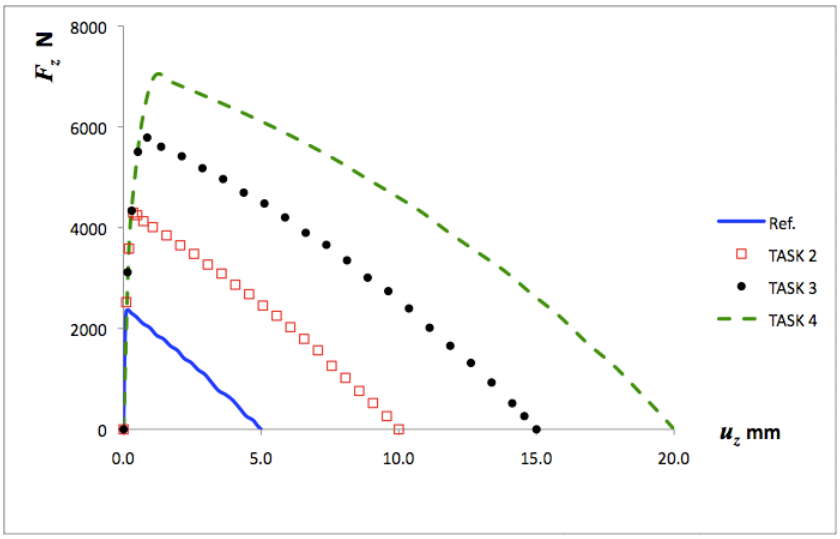


Fig.4.29. FEM modelling results showing significance of fiber embedded length $l_f$. Tasks according to Table 4.3

In Fig.4.30. parametric analysis results revealing significance of contact pressure $p_c$ caused by concrete shrinkage are presented. It is expected that the contact pressure $p_c$ is higher when the shrinkage is higher and in this model higher contact pressure is achieved through specifying smaller radius of the cavity $r_m$ with respect to given fiber radius $r_f$.

According to results in Fig.4.30. it has to be concluded that the contact pressure $p_c$ is an important parameter affecting the values of the peak pull-out load and the post peak pull-out resistance.

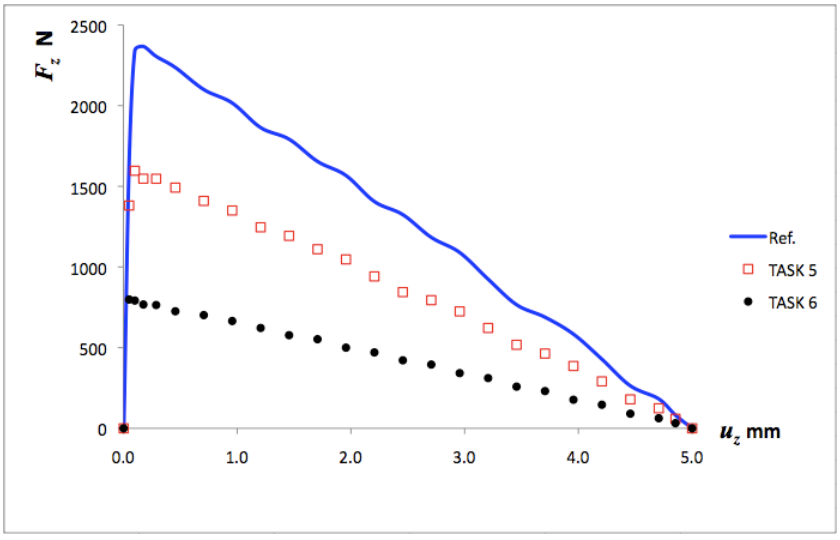


Fig.4.30. FEM modelling results showing significance of residual stresses caused by shrinkage of concrete. Tasks according to Table 4.3

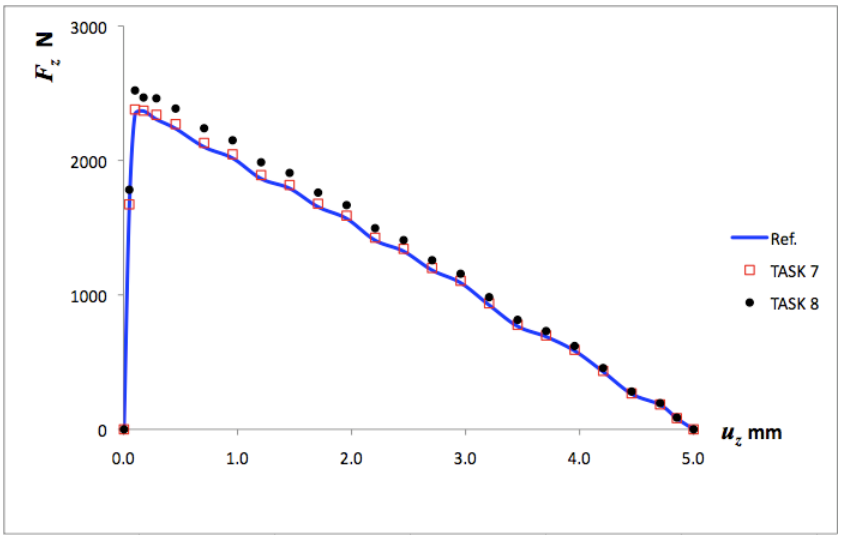


Fig.4.31. FEM modelling results showing significance of fiber radius $r_f$. Tasks according to Table 4.3

In Fig.4.31. results for different fiber radius $r_f$ values are presented in the range between 0.375 to 0.4 mm. Since fiber with a larger radius $r_f$ has larger surface area, the contact area is also larger thus resulting in higher resistance to applied pull-out load as seen in Fig.4.31.

Fig.4.32. shows the high significance of friction coefficient $\mu$ between fiber/concrete surfaces. While the previously studied contact pressure is physically related to concrete shrinkage, coefficient of friction is related to microstructure of concrete and steel fiber surfaces and thus can be different depending on concrete mix and fiber type.

Coefficient of friction $\mu$ was varied in the range between 0.3 to 0.1 and Fig.4.32. shows large differences in modelled pull-out relation between those cases. It has to be concluded that the pull-out resistance significantly depends on both contact pressure $p_c$ and the coefficient of friction. Thus, if an experimental pull-out test is performed, it is not possible to determine the values of both $p_c$ and $\mu$, but only their combined effect, i.e., $p_c \cdot \mu$, unless additional measurements on shrinkage or friction tests are performed.

Finally, modelling results demonstrated in Fig.4.33. show significance of fiber elastic modulus $E_f$. $E_f$ was varied in a narrow, realistic range for steel fibers – between 200 and 220 GPa explaining the narrow difference between pull-out curves in Fig.4.33.

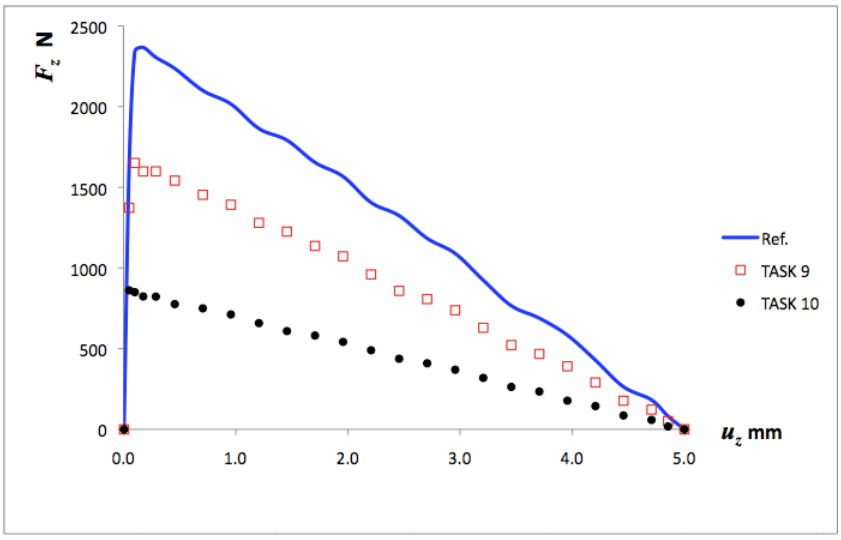


Fig.4.32. FEM modelling results showing significance of fiber/concrete surface friction coefficient $\mu$. Tasks according to Table 4.3

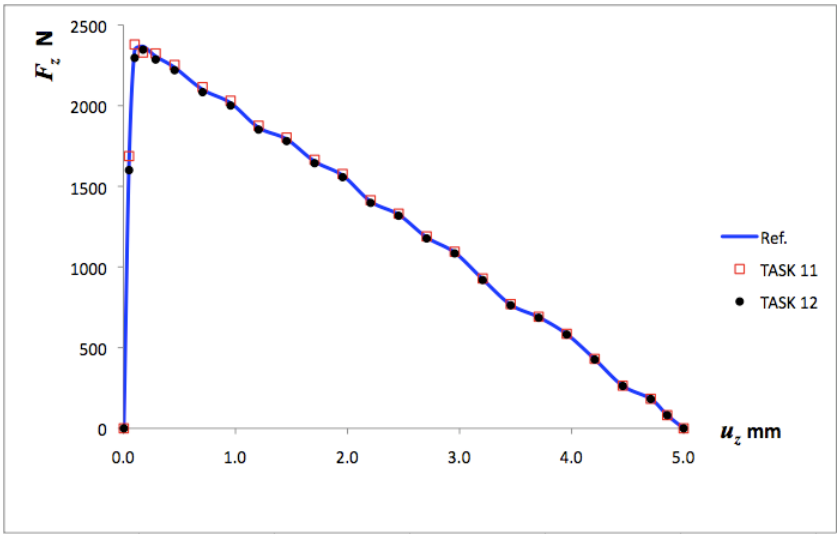


Fig.4.33. FEM modelling results showing significance of fiber elastic modulus $E_f$. Tasks according to Table 4.3

To summarize the fiber pull-out resistance parametric analysis results of initially debonded interface case it can certainly be concluded that the contact pressure $p_c$ and coefficient of friction $\mu$ are of highest significance. Steel fiber radius $r_f$ and elastic modulus $E_f$ variation within a realistic range provides only a minor change in pull-out resitance of fiber. Finally, the embedded fiber length $l_f$ proved to be significant. If steel fiber/concrete

interface bond strength is negligible, it would be preferable to use longer fibers to achieve higher pull-out resistance.

In the following, the modelling results for initially bonded interface case are discussed.

The tasks of parametric analysis for this case are described in Table 4.4. Different variations of maximal tangential contact stress $\tau_{\max}$, tangential slip after complete debonding $u_t^c$ as well as contact pressure $p_c$ have been studied in parametric analysis.

Table 4.4.

Parametric analysis tasks for the initially bonded interface

| Case name: | $E_f$ | $E_m$ | $r_f$ | $r_m$ | $p_c$ | $l_f$ | $\tau_{\max}$ | $u_t^c$ | $\mu$ |
|---|---|---|---|---|---|---|---|---|---|
| | [GPa] | [GPa] | [mm] | [-] | [MPa] | [mm] | [Pa] | [mm] | [-] |
| Reference | 210 | 30 | 0.375 | 0.360 | 772.7 | 5 | 5e9 | 0.3 | 0.3 |
| Task 13 | 210 | 30 | 0.375 | 0.360 | 772.7 | 5 | 2e9 | 0.3 | 0.3 |
| Task 14 | 210 | 30 | 0.375 | 0.365 | 515.8 | 5 | 2e9 | 0.3 | 0.3 |
| Task 15 | 210 | 30 | 0.375 | 0.365 | 515.8 | 5 | 1e9 | 0.3 | 0.3 |
| Task 16 | 210 | 30 | 0.375 | 0.365 | 515.8 | 5 | 1e9 | 0.25 | 0.3 |

Modelling results for all tasks of initially bonded interface case are presented in the same axes in Fig.4.34. Since it was found out that after completion of debonding the pull-out resistance is exactly the same as for the case of initially debonded interface, the modelling results are presented for displacement range between 0 and 1 mm.

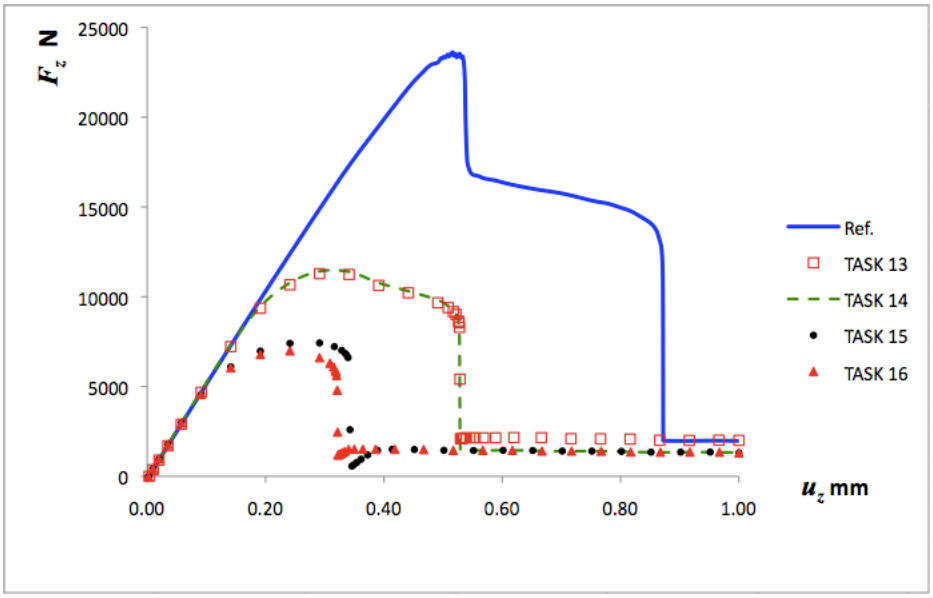


Fig.4.34. FEM modelling results showing significance of different parameters according to Table 4.4

As it is shown in Fig.4.34. initial response to the applied pull-out load in all tasks is linear since the interface is bonded. The non-linear behaviour continues until critical tangential fracture energy $G_{IIc}$ is reached according to Eq.(4.22). Then the interface debonding starts and according to section 4.1.4. and particularly to modelling results demonstrated in Fig.4.24. it is expected that the reaction force $F_z$ will decrease due to initiation and further propagation of debond crack. Due to relatively high bond strength in the reference case ( $\tau_{\max} = 5$ GPa) rather high displacement (load) has to be applied in order to cause interface debonding. When the debonding starts, a high amount of energy is released from this highly strained system. It can be seen in Fig.4.34. as a sharp decrease of reaction force $F_z$. As it was proved in section 4.1, when the debond length $l_d$ has increased, the debond crack growth related energy release rate $G_{II}$ and crack propagation rate decreases. In the reference case in Fig.4.34. it is evident from the much slow decrease of reaction force $F_z$ after the high decrease after peak load. Further, as it can be seen for the reference case, the reaction force $F_z$ decreases until completion of debonding, which results in another severe drop of $F_z$. After completion of debonding the reaction force $F_z$ forms only due to contact pressure ( $p_c$) and friction ($\mu$) and the reaction force gradually decreases with the applied displacement $u_z$. The behavior of fiber after completion of debonding is the same as in the case of initially debonded interface.

According to curves shown in Fig.4.34., the sharp peak signalling for high amount of released energy was found only for the reference case. In Tasks 12 and 13 (as listed in Table 4.4) the bond strength parameter $\tau_{\max}$ was equal to 2 GPa. From the modelled curves in Fig.4.34. it can be seen that the maximal load for Tasks 12 and 13 is lower than for the reference as a result of smaller bond strength and a slow decrease of reaction force $F_z$ occurs until completion of debonding. After completion of debonding, though, a significant decrease of $F_z$ occurs similarly as for the reference case. It can be noted that after completion of debonding the pull-out resistance is higher for Task 13 is higher than for Task 14 since the contact pressure $p_c$ is higher.

Considering results for Tasks 15 and 16 one can again note that maximal pull-out load is smaller since the bond strength is lower. Comparing Task 15 and 16 one can also note that maximal pull-out load for Task 16 is lower than for Task 15 because tangential slip at the completion of debonding is smaller (see Table 4.4).

To summarize the results of parametric analysis for the case of initially bonded interface first to mention would be that at high bond strengths ( $\tau_{\max}$ ) distinct peaks in pull-out curves

can occur because of the large amount of energy being released when the debond crack finally initiates and propagates.

For lower bond strength ( $\tau_{\max}$ ) values the amount of energy being released due to debond crack propagation is smaller and thus pull-out curve will not can have no distinct peak.

It is important to note that for some experimental pull-out samples those distinct peaks were found, while for other samples of the same configuration the curves were "smooth". The modelling results just presented can actually explain these differences. Certainly such differences in experimental results between samples of the same configuration speak for disadvantages and call for improvements of the hand lay-up method by which these samples were produced in order to reduce the scatter.

The contact pressure $p_c$ and coefficient of friction $\mu$ between steel fiber/concrete matrix surfaces are not included in the debonding model used in ANSYS. Therefore they do not affect the pull-out curve during initial and debonding stages. As proved by results, these parameters came into significance and affect the pull-out resistance only after completion of debonding.

Although initial linear pull-out response for the initially bonded case depends on fiber elastic modulus $E_f$ it was not analyzed in this parametric study because previously proved insignificant variation within realistic range.

### 4.2.4. Comparison between modelling and experimental results

In the previous section 4.2.3 parametric analysis results were presented for both initially debonded and initially bonded interface cases. In this section a comparison with experimental data is performed. The model parameters that give the best fit with experimental curves were found for both initially debonded and bonded models and results are summarized in Table 4.5. Comparison was performed with experimental results for configurations B4F4 ( $l_f = 20$ mm), B4F7 ( $l_f = 15$ mm), B4F10 ( $l_f = 10$ mm) and B4F13 ( $l_f = 5$ mm).

For the initially debonded interface model comparison with experimental data was performed in the whole displacement range ( $u_z = 0 \div l_f$ ) while for the initially bonded model comparison was performed in the range ( $u_z = 0 \div 1$ mm).

The comparison between modelling and experimental results is presented in Figs.4.35 – 4.42. Average experimental curves were used in all cases.

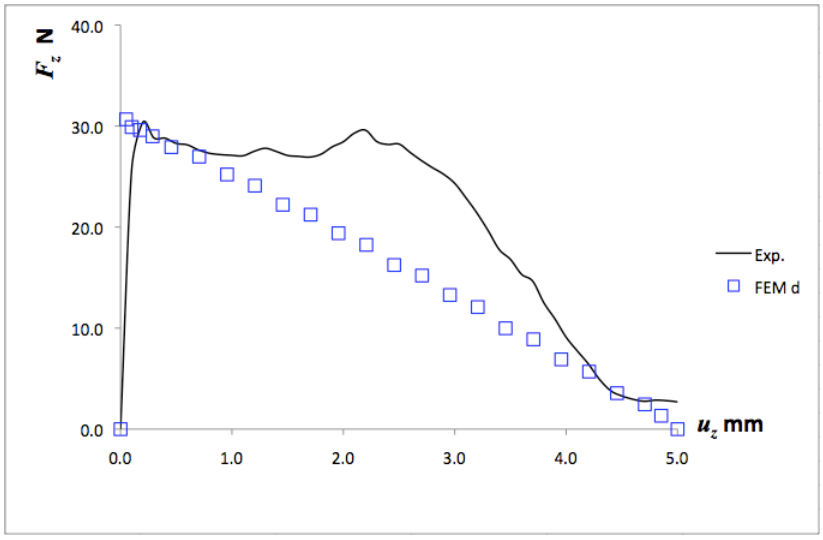


Fig.4.35. FEM modelling results using initially debonded interface model (FEM d), in comparison with the experimental data for $l_f = 5$ mm (see B4F13 in Chapter 3)

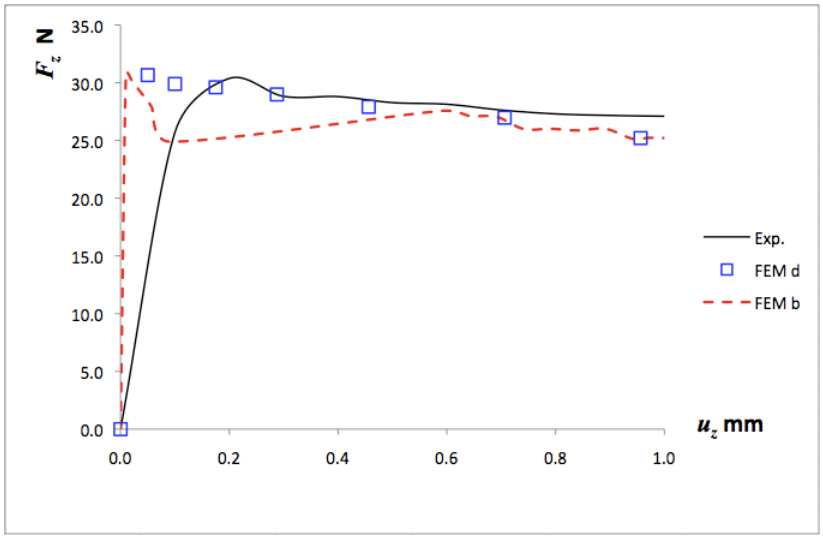


Fig.4.36. FEM modelling results using both initially debonded (FEM d) and bonded (FEM b) interface models, in comparison with the experimental data for $l_f = 5$ mm (see B4F13 in Chapter 3)

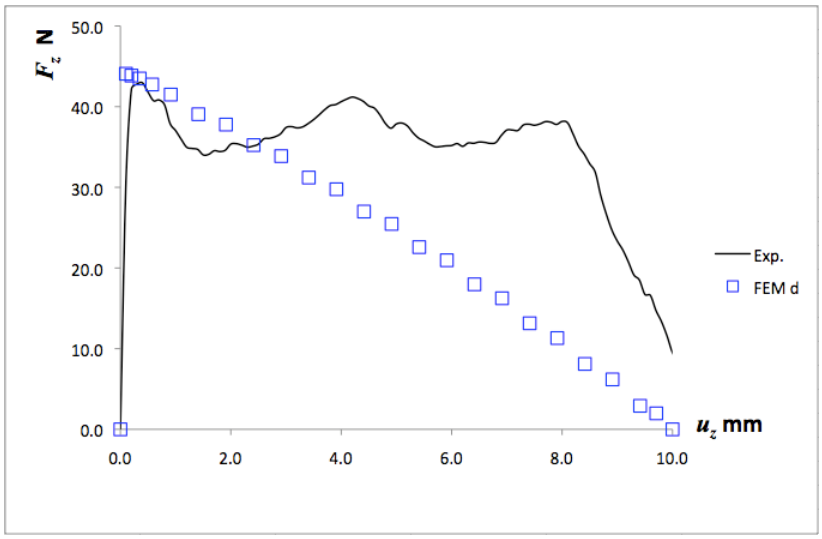


Fig.4.37. FEM modelling results using initially debonded interface model (FEM d), in comparison with the experimental data for $l_f = 10$ mm (B4F10 in Chapter 3)

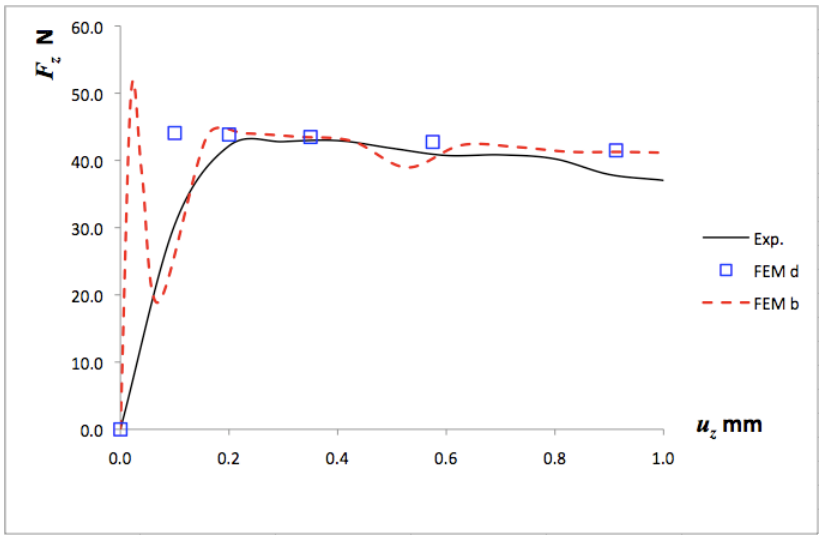


Fig.4.38. FEM modelling results using both initially debonded (FEM d) and bonded (FEM b) interface models, in comparison with the experimental data for $l_f = 10$ mm (B4F10 in Chapter 3)

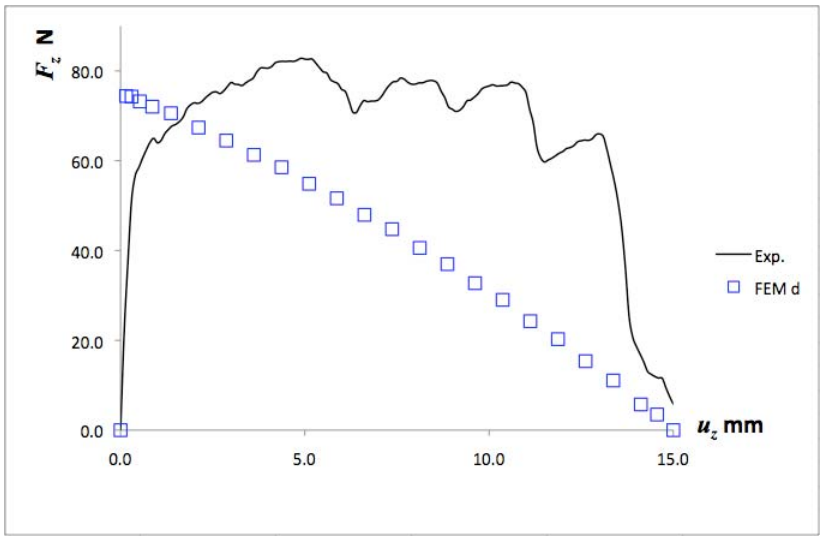


Fig.4.39. FEM modelling results using initially debonded interface model (FEM d), in comparison with the experimental data for $l_f = 15$ mm (B4F7 in Chapter 3)

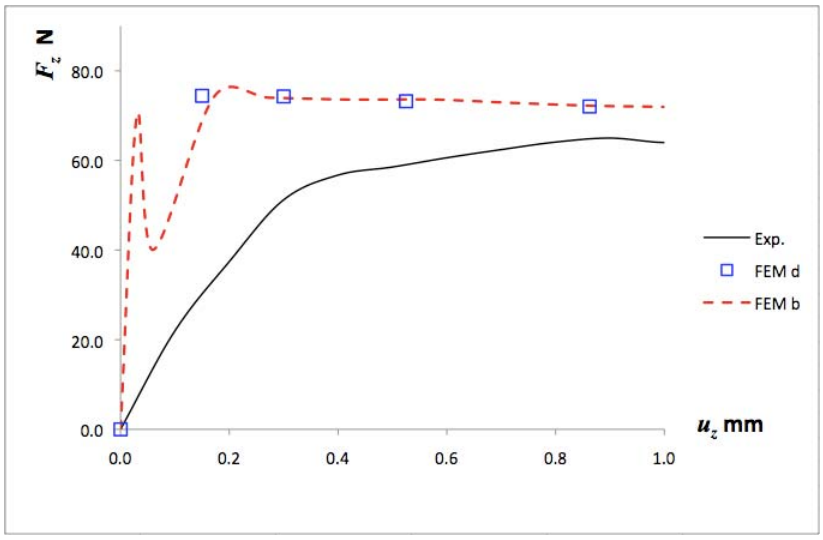


Fig.4.40. FEM modelling results using both initially debonded (FEM d) and bonded (FEM b) interface models, in comparison with the experimental data for $l_f = 15$ mm (B4F7 in Chapter 3)

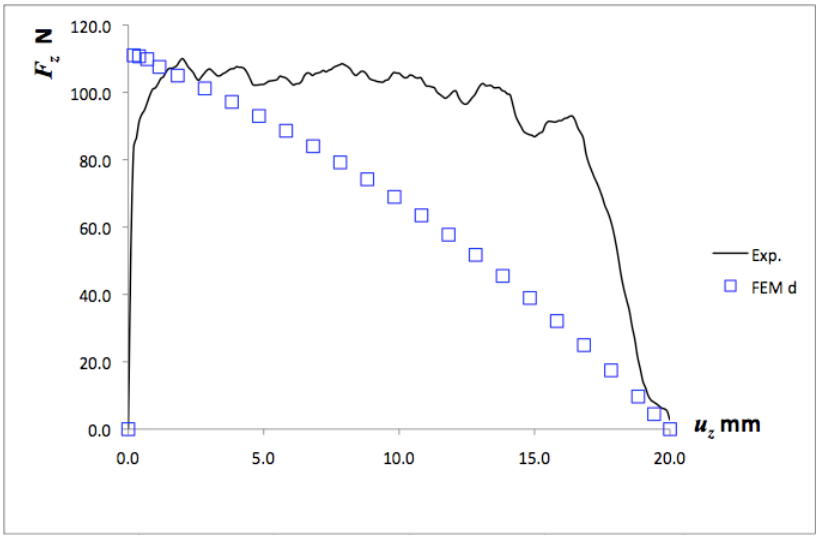


Fig.4.41. FEM modelling results using initially debonded interface model (FEM d), in comparison with the experimental data for $l_f = 20$ mm (B4F4 in Chapter 3)

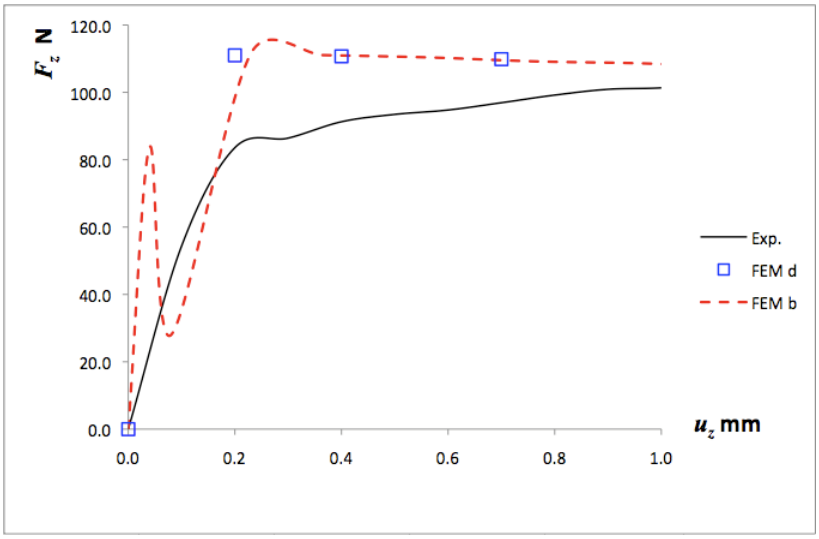


Fig.4.42. FEM modelling results using both initially debonded (FEM d) and bonded (FEM b) interface models, in comparison with the experimental data for $l_f = 20$ mm (B4F4 in Chapter 3)

Analyzing the comparison between experimental results and initially debonded interface model (Figs.4.35, 4.37, 4.39, 4.41) it is notable that the agreement in maximal load is good, in the middle part of the experimental curve the agreement is not satisfactory. In fact, it was already discussed in Chapter 3, were experimental results were presented, that pull-out of

straight fiber is probably accompanied by compaction of the concrete particles at the interface and thus increase of the coefficient of friction may occur. It was also discussed in Chapter 3 that not always the plateau zone of pull-out curve occurs because of particle compaction during pull-out. It is strictly dependant on the mix design and properties of the concrete matrix as for concrete mixes with relatively large particles and lower densities no compaction should be expected. A better agreement between modelling and experimental results could thus be obtained for the case of concrete mixes with larger ingredient sizes. The other option would be to account for the changes in the friction coefficient $\mu$ and use it as a function of pull-out length.

Concerning the agreement between experimental and initially bonded case modelling results one can note that no sharp peak is present in averaged experimental curves thus giving rise to bad agreement in the initial part of pull-out law. The values of $\tau_{\max}$ which are presented in Table 4.5 are therefore not exact, but are presented for assumed agreement. For few experimental samples initial peaks were found, however because of the averaging of results between samples, they are not clearly evident on the average experimental curve.

One can then question whether the bonded interface model can be applicable and also question the existance of initial bond in the experimental samples. Although no distinct peak is evident in the initial part of experimental curves it can be related to either averaging or partial debonding of the interface. Furthermore, the character in the further part of experimental curve is in rather good agreement with initially bonded model results, which confirms occurance of debond and its propagation.

The parameters according to the best fit with experimental data are summarized in Table 4.5.

Table 4.5.

Modelling parameters giving the best fit with different cases of experimental test results

| Experimental case | $l_f$ | $r_f$ | $r_m$ | $p_c$ | $\mu$ | $\tau_{\max}$ | $u_t^c$ | $G_{IIc}$ |
|---|---|---|---|---|---|---|---|---|
| | [mm] | [mm] | [mm] | [MPa] | [-] | [MPa] | [mm] | [J/m$^2$] |
| B4F4 | 20 | 0.375 | 0.37477 | 12.202 | 0.3 | 2.67 | 0.1 | 133.5 |
| B4F7 | 15 | 0.375 | 0.37481 | 9.838 | 0.3 | 2.67 | 0.1 | 133.5 |
| B4F10 | 10 | 0.375 | 0.37490 | 5.272 | 0.3 | 2.60 | 0.1 | 130.0 |
| B4F13 | 5 | 0.375 | 0.37481 | 9.767 | 0.3 | 2.67 | 0.1 | 133.5 |

In [82] a threshold interfacial contact pressure for cement mortar/ steel fiber system has been approximately estimated to be 10 MPa. The threshold contact pressure represents the magnitude of clamping that is able to maintain compressive mode before debonding takes

place. The Poisson's effect in steel fiber/concrete matrix system, as mentioned, is counteracting the residual compression and if compressive mode is reduced then unstable propagation of debond crack may occur. The values obtained in this study, which are presented in Table 4.5, are actually very close to reported 10 MPa, however, the results were proved to be very sensitive to the magnitude of friction coefficient which is also unknown a priori.

## 4.3. Summary of numerical modelling of fiber pull-out

In this section (Chapter 4) numerical modelling of fiber pull-out was performed. For analyzing the interface debond initiation and propagation a 2-D axisymmertric FEM model was developed to be used in combination with fracture mechanics approach. Virtual crack closure technique was employed to calculate the debond crack growth related energy release rate $G_I$ and $G_{II}$. It was proved that undesirable Mode I crack propagation could occur under certain conditions and parametric analysis was performed in order to evaluate possible options to eliminate it. Simple expressions were developed to describe Mode II debond crack growth and to perform debond growth simulations. Pull-out law for the debonding stage was derived in form of a simple expression and was validated by FEM calculations giving very good agreement.

3-D FEM models were developed to analyze the role of residual shrinkage stresses. Modelling of complete fiber pull-out was performed for two cases: initially debonded interface and initially bonded interface. Significance of interface and constituent properties was also evaluated through a parametric analysis.

The proposed numerical models were presented as a convenient modelling and analysis tool for the engineer. The models can be useful either to select materials to achieve desirable fiber resistance and thus desirable FRC post-cracking behavior or to characterize interface properties for a given system, for which experimental measurements of load-displacement are avilable.

In the present work, the numerical modelling of pull-out was performed only for straight and aligned fibers mainly due to practical reasons. Aligned fiber pull-out can be conveniently studied as a 2-D axisymmetric problem and the parametric study results can be analysed in a straightforward way. Pull-out of an inclined fiber on the other hand has to be a 3-D analysis because the axisymmetry is no longer valid and therefore more computer power must be involved in order to obtain FEM solution. Including bending and straightening of the inclined,

hooked-end and undulated shape fibers is related to plastic deformations and significantly more computer power is required for solution. In [44] a 3-D numerical (FEM) modelling of pull-out was performed for aligned hooked-end fiber by using interface elements to account for debonding and material plasticity to account for fiber straightening and concrete matrix compression. Symmetry conditions were used in order to reduce the size of the model. Notably, experimental results of straight fiber pull-out were used to define the properties of the interface. Thus it can be confirmed that the results of extended parametric analysis performed in this study can contribute as an input for more complicated models. Although results in [44] seem very interesting, they were specificly obtained only for a few configurations, therefore the authors in [44] still suggest a simpler 2-D modelling as an operating tool for parametric evaluation in order to save calculation time.

Nevertheless, because the personal computer power still keeps increasing, modelling of pull-out of complex shape fibers can soon be expected to become feasible. Then including effects of inclination of fiber and matrix spalling should not also be troublesome.

# 5. MODELLING OF LOAD BEARING CAPACITY OF FRC BEAMS

## 5.1. Objective of macro-mechanical model

The objective of this section is to elaborate modelling tool for calculating and predicting the load bearing capacity of FRC structural beams subjected to bending loads. In the literature review chapter (Chapter 1) the existing models were reviewed and analyzed. As it was concluded there the most of the existing models are based on the inverse approch, meaning that constitutive laws in form of a stress-strain ($\sigma-\varepsilon$) or stress-crack width ($\sigma-w$) relations are determined from experimental tests of FRC elements using linear or multi-linear aproximation. Exactly the same approach of determination of load bearing capacity of FRC elements is used in previously available and in recently proposed design regulations and recommendations [58,67-71,75] which are issued together with instructions for experimental specimen dimensions, suggested preparation and testing methodology. The principle of the constitutive laws used in regulations is based on linear, bilinear or multi-linear relations that are used for specific ranges of strains $\varepsilon$ or crack widths $w$. Certain values of corresponding stresses $\sigma$ are then defined in the intersections of these linear regions. Due to statistical distribution of experimentally tested samples, the stresses are multiplied by several safety factors $k_i$, where $k_i<1$. Thus the flexural strength values for structural design are determined. When a $\sigma-\varepsilon$ or $\sigma-w$ relation is available from the tests, it has to be readjusted according to the requirements of the linear and multi-linear models, depending on the requirements of recommendations being used. Fitting the values of experimental curve with multi-linear relations is not always feasible and often the fitting procedure is not straightforward and comprehensible. Therefore, large differences of flexural strengths can be obtained from seemingly similar curves.

The safety factors $k_i$ used in recommendations are often rather low and specified in form of a numerical constant rather than being dependant function on amount and type of fibers used in FRC. The overall use of design recommendations and regulations is, of course, gaining more widespread use, however, many aspects concerning determination of design strength are questionable. Thus, direct approaches may be attractive as alternative to often not applicable inverse methods.

Unfortunately, the direct approaches that have been presented in literature [63] have always been associated with many parameters that are also unknown unless determined experimentally.

In order to prevent the necessity to perform experimental measurements along with the structural design, a large database of systematically structured parameter values and relations is necessary. In the present work load bearing capacity and post-cracking behaviour of FRC beams are modelled using the database of experimental pull-out test results that were performed and summarized in Chapter 3. The general principle of the model proposed in this work is that the pull-out laws of individual fibers are applied in order to calculate the transferred load through the crack. The number of fibers in cross section is calculated through the given amount of fibers in the concrete mix. A random orientation angle is determined for each fiber and then the appropriate pull-out law for that specific inclination angle are used for calculations of the load that is transferred through the crack. The step-by-step modelling procedure is described further in the text.

It has been shown by this study and numerous previous research papers discussed in the literature review chapter that as soon as micro cracks appear in the structural FRC element, the fiber bridging mechanism activates instantly thus resisting the crack growth. Therefore the load bearing capacity of any structural FRC element directly depends on fiber capability to resist the pull-out loads. For structural beams and plates made form homogeneous isotropic materials subjected to bending loads the crack localization will most often occur at the cross-section where the highest bending moment is acting. For FRC beams or plates, however, the localization of a crack depends both on the maximal bending moment and also on the number of fibers in each cross-section. Notched beam specimens are therefore often used in order to initiate the crack at a desired cross-section so that representative, consistent values of flexural strength and other parameters can be obtained.

After the micro-cracks have formed in the tensile zone of FRC element, the further increase of applied load eventually leads to crack localization at the critical cross-section. The load bearing capacity of a FRC element will directly depend on the type, configuration (shortest embedded length, inclination angle) and number of fibers bridging this crack. The objective of Chapter 3 was to determine the pull-out laws for these different possible configurations of fibers so that these effects could be included in the model described here.

Analytical pull-out expressions for pull-out laws could be an alternative but, unfortunately, as it was discussed previously in the literature review chapter (Chapter 1) of this study, the analytical models are unable to accurately describe the pull-out response of fibers, especially when non-aligned and non straight fibers are used. The analytical prediction models that are presented in the literature are mostly based on experimentally obtained parameters in order to achieve a good agreement [9] and validation is always useful. The

numerical methods, another alternative of fiber pull-out studies require a lot of input data such as friction coefficients and residual stresses due to concrete shrinkage which again require validation. The numerical modelling results presented in Chapter 4 of this study proved that once these parameters are determined for one length of fiber, they can be applicable for other lengths and a good agreement with experimental data can be achieved.

Regarding the difficulties involved in obtaining reasonable analytical and numerical relations, a direct application of experimentally obtained pull-out relations, if available, is probably the best alternative.

The abovementioned discussion has emphasized the motivation and advantages of using the experimental pull-out test results as a model input.

## 5.2. Macro-scale modelling procedure

In this section the procedure of macro-scale modelling is described in detail. The aim of the macro-scale model is to obtain relation between the applied external load and the crack opening displacement at the critical cross-section. The model proposed in this work takes into account the types of fibers used in the concrete mix and also the quantity of each fiber type. It is worth noting that it has been shown by many research papers that the amount and type of fibers used in FRC mix significantly influence the load bearing capacity and behaviour of the FRC structural element. Still, the design recommendations currently available fail to accurately evaluate the fraction of fibers - only approximate classification has been introduced separating normal FRC from high-performance FRC with the latter being with higher fiber amount per volume unit than the first [58,67-71,75].

Considering the high cost of steel fibers, incorporating the fiber volume fraction in structural design would be of high economical interest also.

Furthermore, as it will be shown in the following, the model presented here is capable of accurately taking into consideration hybrid FRC, where two or more types of fibers are used in the same mix.

Understandably, in structural design regulations for many safety reasons no cracks or limited size and amount of cracks are allowed depending on significance of the structure in question. From scientific researchers point of view, however, the large amount of load bearing potential of FRC to resist loads in the post-cracking stage should not be disregarded. The motivation to study rather large crack openings in this study comes from research interest.

The macro-scale model was developed using parametric language in a MATLAB [94] software based code. Previously, the average pull-out relations for all fiber configurations

were stored in a database file and made available for input in form of text files with pull-out load and corresponding displacement results arranged in equally sized columns.

In the following, the modelling procedure will be described and illustrated.

A FRC beam with chaotic fiber orientation subjected to four point bending will be shown as a modelling example. The loading scheme and the bending moment diagram are shown in Fig.5.1. Four point bending test is a standard testing method to determine flexural strength and load bearing capacity of FRC beam. It has also been suggested in RILEM design recommendations [58,75].

It is expected that a major crack will form in the zone of maximal bending moment according to the diagram. Considering the heterogeneity of the fiber distribution in FRC the crack is actually expected to occur at the cross-section with the weakest cross-section in terms of number of fibers.

As the first inputs in model, the dimensions of the FRC beam are given, i.e., $L$ and $H$ are specified according to Fig.5.1.

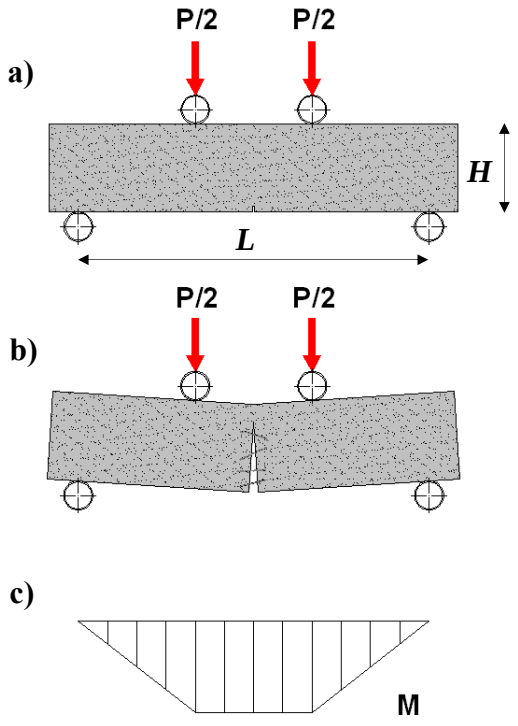


Fig.5.1. Loading scheme for a four point bending test: a) Initial state; b) formation of crack; c) bending moment diagram

The width of the beam is also specified as input parameter $B$.

The total length of fiber $l_{f,sum}$ and fiber radius $r_f$ are given so that the number of fibers per weight unit can be calculated as:

$$n_w = 1/m_f \tag{5.1}$$

where $m_f$ is the mass of one fiber calculated as:

$$m_f = \pi r_f l_{f,sum} \rho_f \tag{5.2}$$

where $\rho_f$ is fiber density.

If the fiber weight fraction in the concrete mix is given and it is denoted as $w_f$, then the number of fibers per one volume unit can be calculated as:

$$n_v = w_f \cdot n_w \tag{5.3}$$

Both number per weight unit $n_w$ and number per volume unit $n_v$ were rounded to integer number prior to further inputs.

The number of fibers in the beam can be simply calculated as:

$$n_b = L \cdot H \cdot B \cdot n_v \tag{5.4}$$

In the further procedure the calculated number of fibers in the beam is randomly distributed along the volume of beam. In the current model state, the fiber location distribution across the length and height of the beam as well as fiber orientation angle distribution have been assumed to be random without any preferred fiber concentration regions or orientation directions. Therefore, a random distribution function was applied in the model in order to assign location of fiber's centre of gravity and orientation angle of each fiber.

Since the loading case given in Fig.5.1. can be considered as two-dimensional and the macro-crack surface is assumed to be straight the width distribution of fibers along $B$ is not crucial and only length and height distribution have to be considered. Thus A 2-D random distribution in the modelling procedure was performed by assigning for each of the $n_b$ fibers a random coordinate for its centre of gravity along longitudinal direction $L$ and height of the beam. The coordinates of distributed fibers were stored as array parameters in the software [94], which were further used in order to find the weakest cross-section of the beam. The weakest (critical) cross-section was searched only within the zone of maximal bending moment according to the diagram shown in Fig.5.1.c. For a beam subjected to four point bending the maximal bending moment region is the distance between the applied loads.

Thus, fiber distribution in this region is analyzed by searching for a cross-section with the least amount of fibers according to the previously assigned distribution. Motivation to find the critical cross-section comes from assumption that the macro-crack growth will take place in it.

When the coordinate of the critical cross-section is found the number and distribution of each fiber type in it can also be found from the previously saved fiber coordinate and inclination arrays. Embedded length of each fiber $l_f$ and inclination angle $\alpha$ is specified with respect to the plane of the critical cross-section, which is assumed to be perpendicular to beam longitudinal axis. In the presented model the overlapping effect of fibers as a result of random distribution of fiber gravity center coordinates has not been taken into account in the algorithm, however, it is not expected that this assumption could cost the accuracy of the proposed model.

Since the input data – experimental pull-out load and corresponding displacement relations were obtained for fixed, well defined orientation angles (at $\alpha = 0°$, $\alpha = 10°$, $\alpha = 20°$, $\alpha = 30°$, $\alpha = 45°$, $\alpha = 60°$ from Chapter 3) and also for fixed embedded lengths (at $l_f = 25$ mm, $l_f = 20$ mm, $l_f = 15$ mm, $l_f = 10$ mm, $l_f = 5$ mm) the fibers bridging the critical cross-section have to be divided in groups of inclination angle and embedded length ranges. Thus, for example, a fiber, which according to the random distribution has an inclination angle $\alpha = 4°$ and embedded length $l_f = 17$ mm by performing interpolation is classified to belong to the group of inclination angle range $0° \le \alpha \le 10°$ and group of embedded length $15 < l_f \le 20$ mm.

The grouping of fibers into embedded length and inclination angle groups is not considered to introduce a significant inaccuracy since the number of the divided groups is sufficient.

The crack opening due to applied four point bending load is schematically shown in Fig.5.2.

In Fig.5.2. $\delta$ is the maximal crack opening at the lower side of the beam. In the same figure $b(y)$ is the local opening of the crack. Since the local opening of crack $b(y)$ is not constant and varies along the height of the crack the bridging force must be dependant on the local crack opening. In order to do that the type of fibers, number of fibers, embedded length, and orientation angle must be known at each point of the crack. Then the corresponding data from the database file, which contains all pull-out laws from experimental tests, must be correctly read and applied. The coordinates of fibers bridging the crack are known previously from the distribution procedure. Thus a command cycle can be written in the MATLAB [94]

based code, which for each fiber with given embedded length and inclination angle in the critical cross-section finds the pull-out load corresponding to of the local opening of crack $b(y)$.

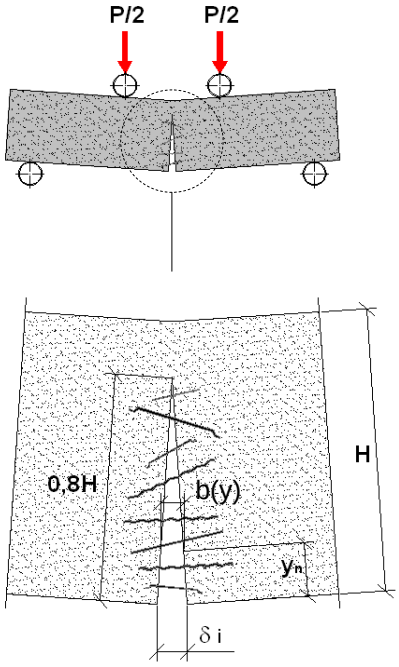


Fig.5.2. Schematic representation of maximal crack opening $\delta$ and local opening of crack $b(y)$

Since for each value of the maximal crack opening displacement $\delta_i$ there will be different values of corresponding local opening displacement $b(y)$, incremental increase of $\delta_i$ can serve as the outer cycle in the code. In the beginning of modelling procedure, the initial maximal crack opening value is set to $\delta = 0.2$ mm.

Fig.5.3. schematically shows the relation between the maximal crack opening $\delta_i$, local pull-out force along the height of the crack $p_{n,i}$ and the bending moment $M_i$ that is related to the external load $P$.

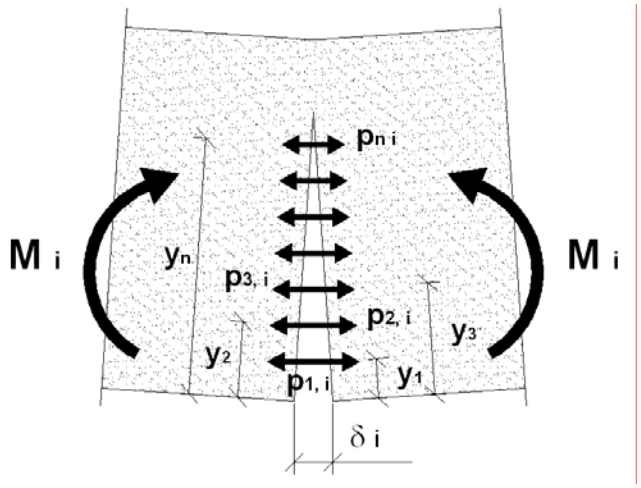


Fig.5.3. Representation of relation between maximal crack opening displacement $\delta_i$, local pull-out force $p_{n,i}$ and bending moment $M_i$

The local crack pull-out load $p_{n,i}$ is calculated for each step of fixed value of $\delta_i$ for each local opening value $b(y_n)$. The bridging pull-out forces at each step of $\delta_i$ can be summarized and thus the bending moment acting in the analyzed cross-section of the beam can be calculated through relation:

$$M_i = \sum_{n=1}^{m} 2 \cdot p_{n,i} \cdot (0{,}8H - y_n) \tag{5.5}$$

where $p_{n,i}$ is the pull-out load at the local coordinate $y_n$ corresponding to local crack opening $b(y_n)$. It has to be noted that in order to simplify the modelling procedure, a fixed crack height was assumed $y_{n,\max} = 0.8 \cdot H$. The chosen crack height was motivated by observations and measurements of the crack height from extensive experimental tests on FRC and HPFRC beams subjected to four point bending loads.

According to the loading scheme for four point bending (see Fig.5.1), the applied bending load $P_i$ at each step of maximal crack opening displacement $\delta_i$ can be calculated as:

$$P_i(\delta_i) = (2 \cdot M_i)/(L/3) \tag{5.6}$$

The relation in Eq.(5.6) can be considered as a constitutive law of the proposed model and it allows to calculate the applied load as a function of crack opening. Thus the load bearing capacity and the post-cracking behaviour of a beam can be characterized using this model for arbitrary type and amount of steel fiber reinforcement.

In each of the steps $i$ in Eq.(5.5) and Eq.(5.6) the values of crack opening were incremented by $\Delta\delta$ = 0.2 mm. The modelling was performed in the range of crack opening displacements between $\delta$ = 0.2 to 6 mm.

An example of the MATLAB input file with description of the listed commands is given in Appendix of this Dissertation Thesis.

## 5.3. Modelling results

As mentioned earlier, the modelling was performed by comprising the previously described commands and operations in Matlab software code [94]. Prior to modelling, text files of average fiber pull-out laws were prepared so that the experimental data can be easily read from the Matlab software environment.

The loading scheme and size of beams used in modelling was chosen with the aim to match experimentally feasible conditions. Therefore load bearing capacity of FRC beams with dimensions $150 \times 150 \times 600$ mm subjected to 4 point bending scheme according to Fig.5.8. were modelled.

Modelling results showing the load bearing capacity of FRC beams with different fiber types are presented in Fig.5.4. The three curves in Fig.5.4. represent modelling results for FRC beam whose reinforcement is either straight, hooked-end or undulated fibers. All curves in Fig.5.4. correspond to the case of fiber weight fraction $w_f = 150 kg/m^3$.

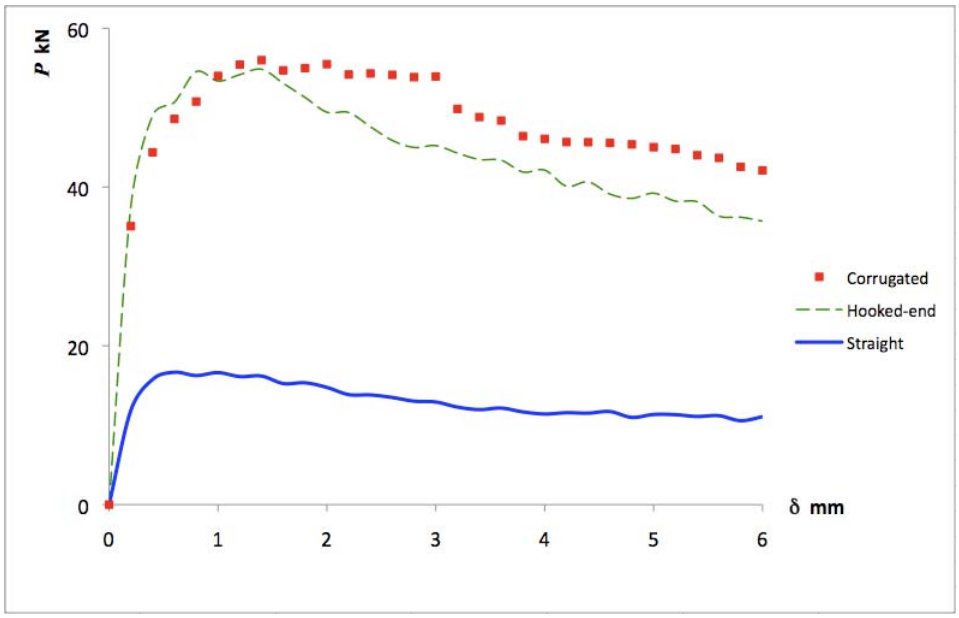


Fig.5.4. Modelling results of load bearing capacity of FRC beams with straight, hooked-end or undulated shape fibers. In all cases fiber weight fraction $w_f = 150 kg/m^3$

First of all, it can be seen that the model gives realistic prediction as compared with experimentally obtained curves. It can be seen that maximal load bearing capacity ($P$) is

achieved at small crack opening displacement $\delta$ values. As the crack opening displacement increases, the load bearing capacity of FRC beam slowly decreases. The modelling results are in accordance with the expectations, since individual fiber pull-out laws were used as input data. A detailed comparison with experimental results is performed further in this work (see section 5.4).

Analyzing the modelling results presented in Fig.5.4. it is notable that FRC beam reinforced with straight fibers will have much smaller load bearing capacity compared with hooked-end and undulated shape fiber reinforced concrete beams with the same weight fraction of reinforcement. It is due to much smaller pull-out resistance of straight fibers as it was demonstrated in Chapter 3.

Although in Chapter 3 it was clearly proved that undulated shape fibers have the highest pull-out resistance, it is important to remember that diameter of fibers is larger for these fibers. Therefore, for the same weight fraction of fibers (as in Fig.5.4. $w_f = 150kg/m^3$) the number of hooked-end fibers will be larger. Furthermore, in order to determine the number of fibers in the concrete mix, the total length of fiber $l_{f,sum}$ was used (see Eq.(5.2)) and it is much higher for undulated shape fibers taking into account their wavelike shape (see Fig.3.8. in Chapter 3). As a result, the nuber of undulated shape fibers is much smaller than the number of hooked-end fibers for a given constant weight fraction and as demonstrated in Fig.5.4., the corresponding load bearing capacity of FRC beams is almost the same. This is an important factor to consider, when structural design of FRC structures is performed. For obtaining an optimal reinforcement solution for a FRC structure, the model presented here is highly significant. If such situation exists as in Fig.5.4., that the same load bearing capacity can be achieved with two different fiber types, then it is always preferable to choose reinforcement with more fibers (in this case, hooked-end fibers) than reinforcement less in number but larger in size fibers (like undulated shape fibers in this example).

Nevertheless, it can still be distinguished that the load bearing capacity of FRC beams with undulated shape fibers (dotted line in Fig.5.4) is the highest. As it was characteristic for undulated shape fiber pull-out laws, also here it can be observed that the maximal load (load bearing capacity) is reached at higher crack opening displacement values than for the case of straight or hooked-end fibers.

Fig.5.5. shows modelling results for FRC beams with straight fibers. 3 different fiber weight fractions are compared in Fig.5.5.: $w_f = 100kg/m^3$, $w_f = 150kg/m^3$ and $w_f = 200kg/m^3$.

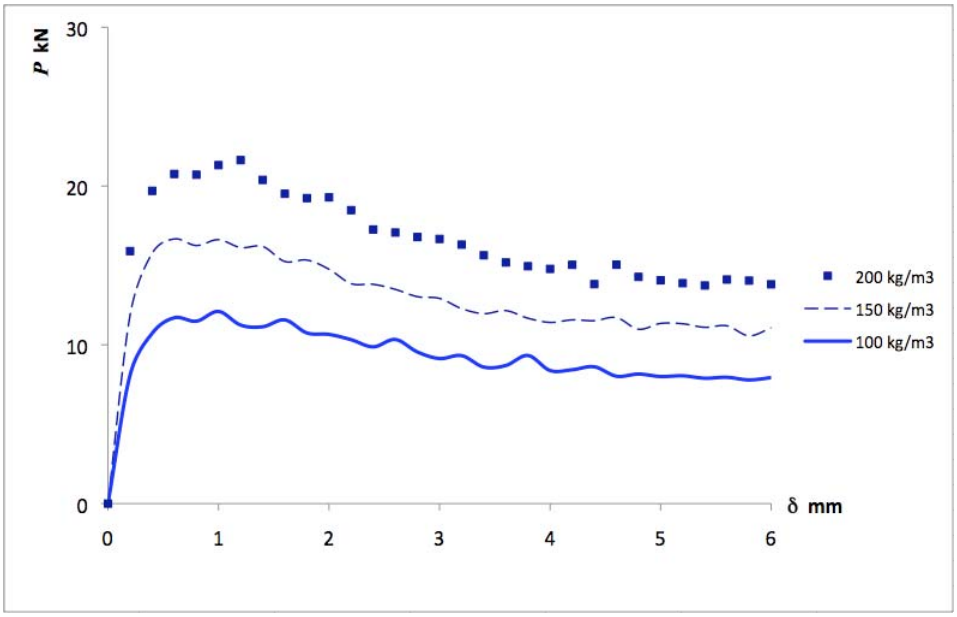


Fig.5.5. Modelling results of load bearing capacity of FRC beams with straight fibers

A linear increase of load bearing capacity with the weight fraction of fibers can be seen from the modelling results in Fig.5.5. It is important to remember that the model proposed in this work is valid in the range of crack opening displacements from $\delta$ = 0.2 to 6 mm and the initial part of all curves presented in Figs.5.4 – 5.7 is linear approximation. As known, the initial response of FRC beams is not directly dependant on the fiber reinforcement (since the practically achievable volume fractions are rather low) and thus the properties of concrete matrix determine the initial slope of the load bearing capacity curves. Judging from the values for straight fiber reinforced concrete shown in Fig.5.5. one can note that the maximal load $P_{max}$ is approximately in the range between 10 – 20 kN. Given the dimensions and loading scheme of the beam (see Fig.5.8) the corresponding maximal flexural stress $\sigma_{max}$ of the beam is in the range between 3.5 – 7.1 MPa. Certainly, tensile strength of high performance concrete can easily overachieve these values. This means that situation might occur when the initial response of the beam is higher than the maximal load bearing capacity provided by fiber bridging. In such case the initial response is linear until tensile strength of the matrix is achieved and the crack forms in the maximal tension zone (lower face of the beam in this case) and then a significant drop of load bearing capacity occurs as the number or type of fibers is not sufficient for withstanding the applied load. Certainly, including the initial response of concrete matrix would be very useful to evaluate this but then again the tensile and flexural strength of brittle concrete matrix is not a deterministic entity and statistical

strength approach would have to be employed. However, if the initial beam response prior to contribution of fiber pull-out mechanisms could be included, it would allow evaluating occurrence of strain softening or strain hardening behaviour which is of very high importance in structural design. It is expected that if the amount of reinforcement is not sufficient, the undesirable event of strain softening will take place, however, if the fiber reinforcement is sufficient (amount of fibers is large and their pull-out resistance is high) then the behaviour of the beam would proceed under strain hardening conditions which is desirable in building structures. These aspects certainly are among the tasks of the further study and development of the currently proposed simple model.

Fig.5.6. shows modelling results for FRC beams with hooked-end fibers. As before modelling results are shown for 3 different fiber weight fractions.

Certainly, the increase of fraction of reinforcement corresponds to load bearing capacity increase. In general, the modelling results presented in Fig.5.6. show that the maximal load bearing capacity $P_{max}$ for hooked-end fiber reinforced concrete beams is in the range between 35 – 80 kN meaning that the corresponding maximal flexural stress $\sigma_{max}$ of the beam is approximately in the range between 12 – 28 MPa.

This is much higher strength compared to straight fiber reinforced beams showed before achieved with the same weight fraction of fibers and the possibility of strain softening behaviour and distinct initial peak is highly reduced, if hooked-end fibers are selected instead of straight fibers.

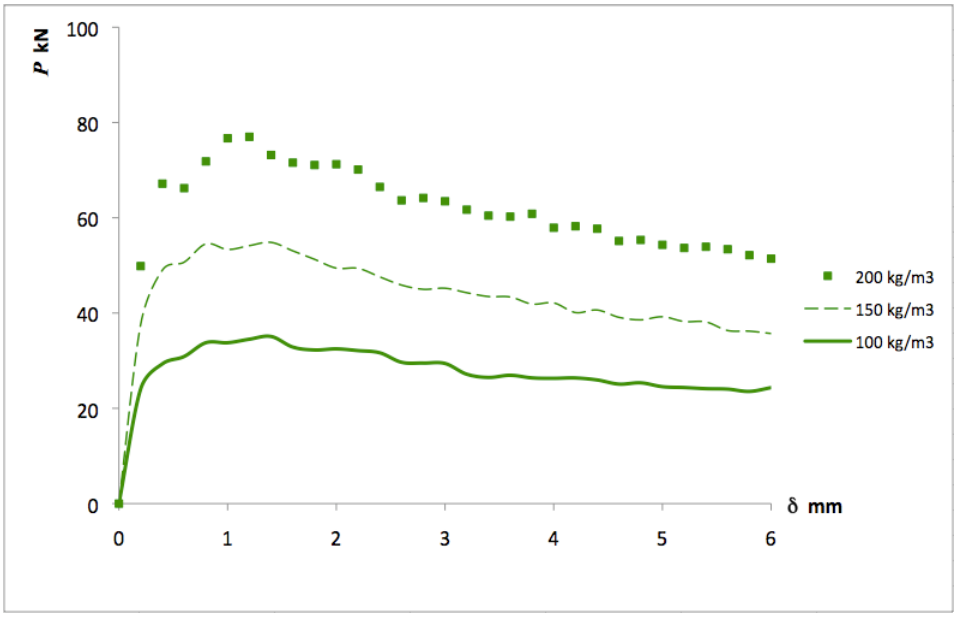


Fig.5.6. Modelling results of load bearing capacity of FRC beams with hooked-end fibers

Finally, modelling results for FRC beams with undulated shape fibers in 3 different weight fractions are shown in Fig.5.7.

The highest load bearing capacity logically corresponds to the highest fiber weight fraction. The range of maximal load bearing capacity $P_{max}$ for FRC beams with undulated shape fibers is within the range of approximately 50 – 90 kN. And the corresponding maximal flexural stress $\sigma_{max}$ of the beam is in the range between 18 – 32 MPa. Certainly, these values for the undulated shape fiber reinforced beams are rather high and if the flexural strength of a pure concrete matrix does not exceed these values, the desirable strain hardening behaviour will be ensured.

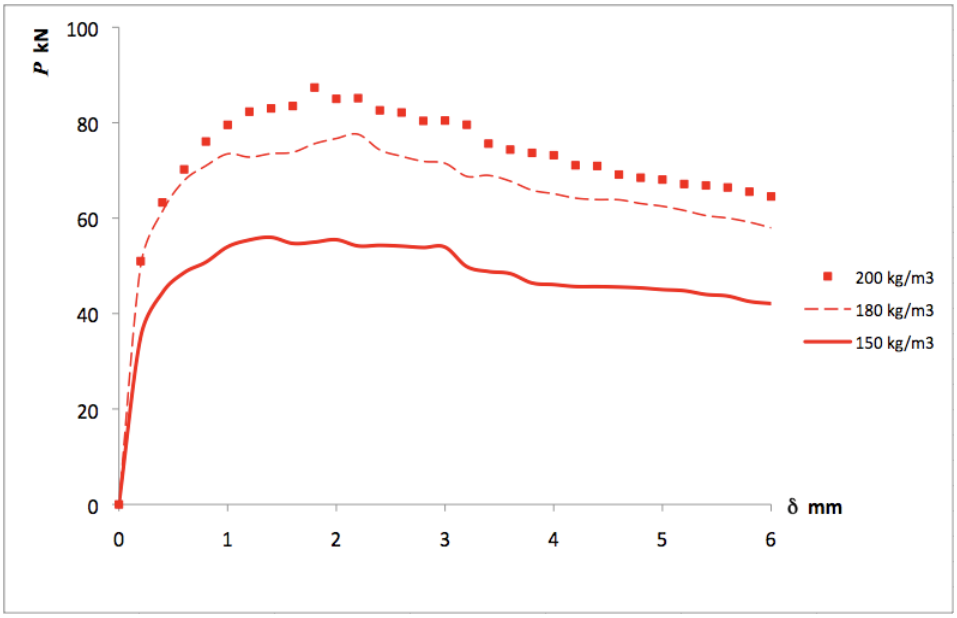


Fig.5.7. Modelling results of load bearing capacity of FRC beams with undulated shape fibers

## 5.4. Experimental validation

The model proposed and described in this chapter was validated with experimental tests. FRC beams with dimensions $150 \times 150 \times 600$ mm were manufactured and tested in 4 point bending scheme according to Fig.5.8. A 2 mm wide notch of 20 mm depth was cut in the middle of the span as demonstrated in Fig.5.8. The purpose of the notch was to initiate one major crack in the zone of the maximal bending moment in order to provide circumstances for reasonable comparison with the previously described model.

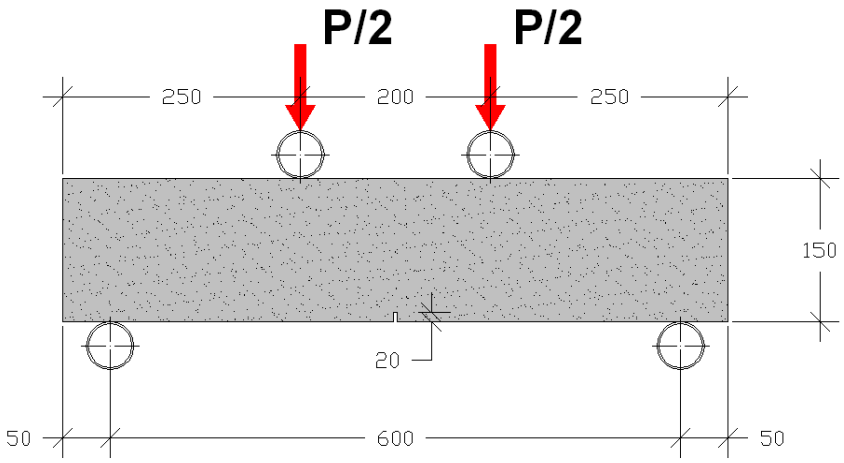


Fig.5.8. 4 point bending test loading scheme

Keeping in mind that the database of experimental pull-out test results was obtained using the concrete mix design specified in Table 3.1 (see Chapter 3) all beams for the model validation tests were prepared with the same mixture. Using a conventional concrete mixer pictured in Fig.3.2. in Chapter 3 a homogeneous concrete mix was obtained and the fibers were added after all the other ingredients were well mixed. Fibers were added by small amounts in steps until the desired weight fraction was reached. By such method a good fiber distribution was ensured and formation of clusters was prevented. It must be noted that the selected concrete mix design listed in Table 3.1 was capable to possess two important features: 1) good workability to allow adding of high weight fractions (up to 300 $kg/m^3$) of steel fibers and 2) ability to prevent fibers from sinking (commonly observed for concrete mixes with high flow-ability and self-compacting concretes). The sinking of fibers is undesirable from point of view of ensuring uniform reinforcement distribution. Also, in the previously described model it was assumed that fiber distribution is uniform in the volume of the FRC beam.

The concrete mix was then casted in moulds in one attempt thus minimizing the possibility of formation of flow fronts that could be the cause for weakened cross-sections. The process of filling of the mould is shown in Fig.5.9. and the freshly casted beam specimen is demonstrated in Fig.5.10.

Fig.5.9. Filling of the mould with FRC mix with high fiber weight fraction

Fig.5.10. FRC beam sample casted in a steel mould

After casting the beam samples were labelled and covered with a soft polyethylene film to prevent the surface of the beam from drying. Samples were demoulded not sooner than 24 hours after casting and the testing was performed after reaching 28 days of hardening.

The bending tests for all beams were performed on a frame produced by Controls S.R.L. company. The beam specimen in the testing frame is demonstrated in Fig.5.10. The capacity of frame that was used in the tests was 150 kN. The applied load $P$ was measured by load cell (pressure transducer) by HBM company. The bending tests were performed under load control using speed of approximately 14 kN/min which for the given FRC beam dimensions and loading scheme (Fig.5.8) corresponds to 5 MPa/min.

For measurements of beam deflection and crack opening displacement, displacement transducers were used as pictured in Fig.5.11. Displacement transducers are also manufactured by HBM company. The measurement range of the displacement transducers was 10 mm. Two transducers were mounted on the side surfaces in order to measure the beam

deflection and one transducer was attached on the lower face of the beam to measure the crack opening displacement.

Fig.5.11. Displacement transducers attached on a FRC beam

The measurements from load cell (pressure transducer) and all displacement transducers were simultaneously recorded on a computer using HBM Spider-8 data acquisition system.

In the present work the experimental results of only undulated shape fiber reinforced concrete beams are presented, similar trends as shown further were observed also for FRC beams with other types of fibers.

3 samples were manufactured and tested for each case of reinforcement weight fraction. Average experimental curves are presented and compared with modelling results in the following. If, for some reason, the beam crack did not initiate and propagate within the maximal bending moment region as according to the conditions of the modelling, the experimental results were discarded from comparison.

5 different weight fractions of undulated shape fibers were used in the experimental validation study of the proposed model. The lowest weight fraction was $w_f = 150 kg/m^3$ and the highest was $w_f = 280 kg/m^3$. It was concluded that the weight fraction of undulated fibers equal to $w_f = 280 kg/m^3$ was the maximal possible to mix in the concrete with mix design listed in Table 3.1 in Chapter 3, while maintaining sufficient workability.

The comparison between modelling and experimental curves for FRC beams with 5 different weight fractions is presented in Figs.5.12. – 5.16.

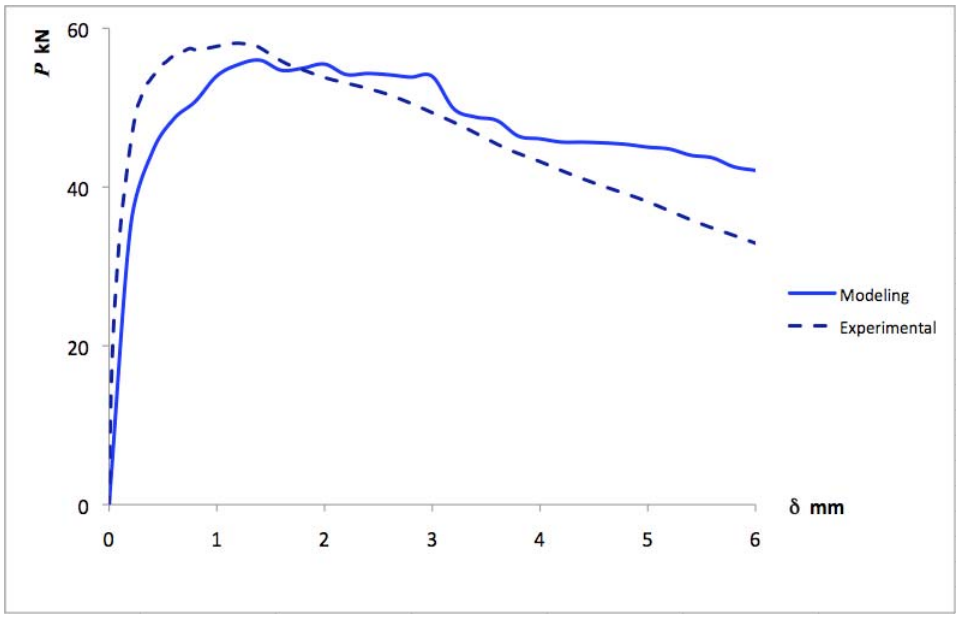


Fig.5.12. Experimental and modelling results for FRC beams F68. Fiber weight fraction $w_f = 150 kg/m^3$

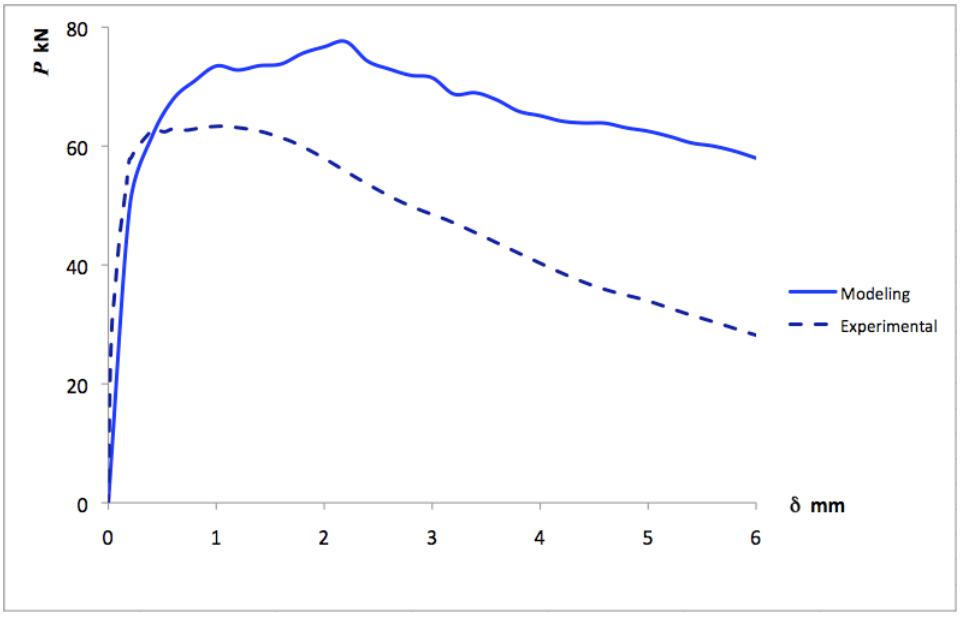


Fig.5.13. Experimental and modelling results for FRC beams F69. Fiber weight fraction $w_f = 180 kg/m^3$

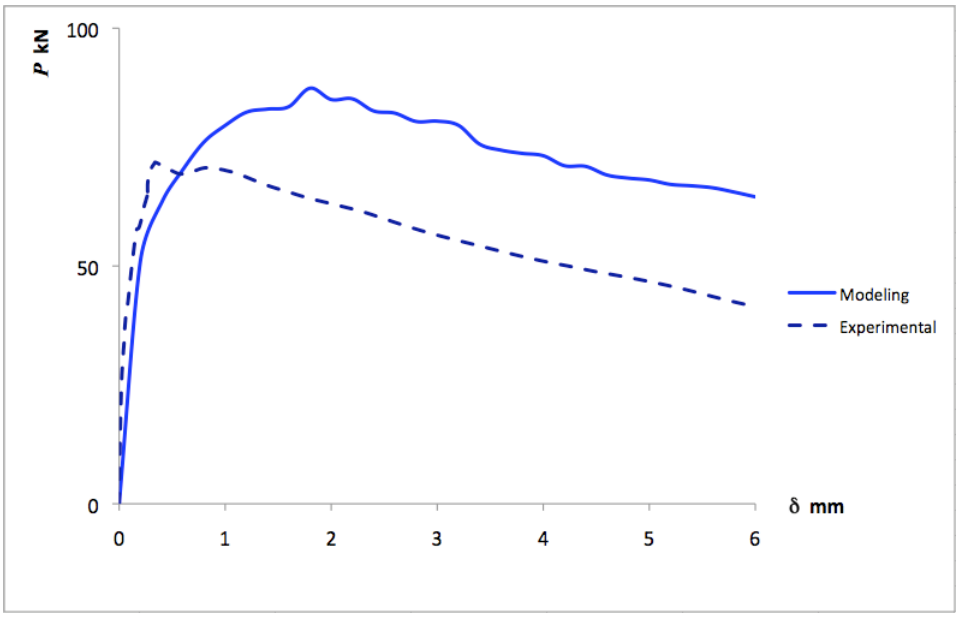


Fig.5.14. Experimental and modelling results for FRC beams F70. Fiber weight fraction $w_f = 200 kg/m^3$

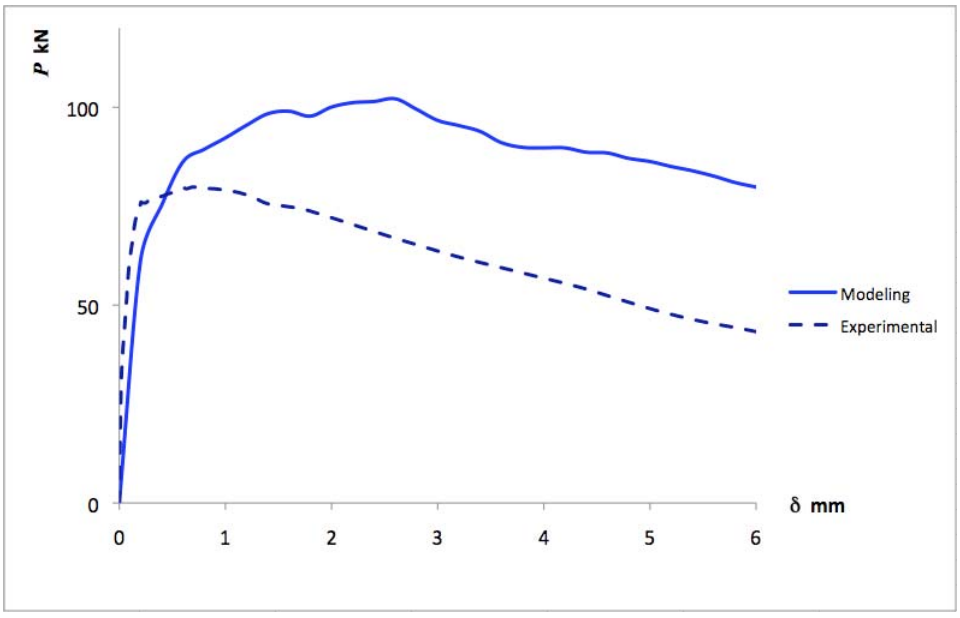


Fig.5.15. Experimental and modelling results for FRC beams F71. Fiber weight fraction $w_f = 220 kg/m^3$

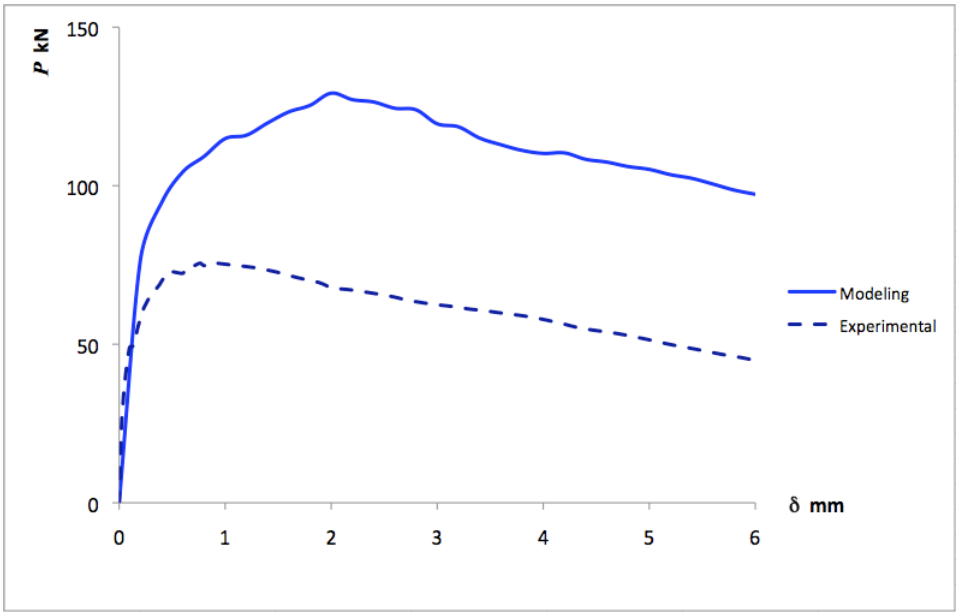


Fig.5.16. Experimental and modelling results for beams F74. Fiber weight fraction $w_f = 280 kg/m^3$

Notation for beams with, for example, F68 was used from point of view of convenience, since the same labelling was followed in the laboratory.

As it can be concluded from Figs.5.12. – 5.16. the presented model for prediction of load bearing capacity of FRC beams gives good results despite the general simplicity of the modelling procedure. The character of modelling and experimental curves is in excellent agreement meaning that the principle of using fiber pull-out laws for a larger scale model has proved to be very efficient. This proves once again the importance of pull-out resistance of individual fibers on load bearing capacity and post-cracking behaviour of FRC structural elements.

The common negative observation from the results shown in Fig.5.12. – 5.16. is that the agreement between modelling and experimental results decreases with increase of the fiber weight fraction in the concrete. There are several factors responsible for this disagreement which are characteristic for higher fiber fractions. For instance, non-uniform distribution of fibers, fiber segregation, multiple fiber interaction (that causes stress concentration and thus an intensive spalling of the matrix) and similar factors that have not been evaluated in the proposed model.

As mentioned earlier, similar trends were observed for other types of fibers as well.

Generally, the modelling results correlate well with the experimental results even some very simple modelling assumptions were used. Evaluating the previously mentioned factors within the model could give rise to better agreement in the future.

## 5.5. Summary of macro-mechanical modelling results

The general conclusion from macro-scale modelling results is that character-wise the agreement with experimental results is very good. The agreement in character of the modelling and experimental curves confirms that the direct modelling approach by using micro-scale experimentally obtained pull-out relations is reasonable. The moderate disagreement in numerical values can have various reasons. Judging from modelling results presented in Fig.5.12. to Fig.5.16. the agreement with experimental data depends on fiber fraction in the mix. According to the results a better agreement corresponds to case of fiber amount of $150kg/m^3$. The possible reason for higher discrepancy with experimental results when fiber amounts are higher than $150kg/m^3$ could be due to fiber distribution. A FRC mix with large fiber amounts does not necessarely follow random distribution across the volume and random distribution of orientation angles as it was assumed in the modelling procedure.

The modelling assumptions such as straight crack planes and constant crack height equal to $0.8H$ should also be revised in order to correspond better with the real conditions. It could be done without introducing complex procedures that are not useful for use in structural design.

Apart from the mentioned aspects the fiber overlapping effects have to be considered. The large amount of fibers often leads to stress concentration and overload of the concrete matrix which leads to spalling of the concrete.

To verify the actual distribution of fibers for various FRC mixes with various fiber fractions, counting of the fibers and in-situ measurements of embedded length and angle distributions are necessary. It could be done by observing the crack surfaces after complete failure of the tested beam.

It also has to be noted that only one size scale has been observed in this study. It is well known for FRC structural and laboratory tested elements that the size of the sample has a large influence on the strength and load bearing cacpacity.

To conclude this chapter it can be mentioned that the model presented in this study differs from the most of structural design guidelines and models available in literature by its ability to evaluate the actual fiber content in the concrete mix. The direct method approach in

the proposed model allows obtaining not only the maximal load bearing capacity but also the general post-cracking behaviour of the structural element. None of the currently available design regulations and guidelines are capable of similar. The model presented in this study can thus be concluded as novelty in the research of fiber reinforced concrete.

# CONCLUSIONS

As the final summary of the present work the following conclusions were drawn:

1. A model for prediction of load bearing capacity and post-cracking behaviour of steel fiber reinforced concrete structural elements was elaborated using the direct modelling approach. The proposed simple model is useful and easy to use, if the fiber pull-out laws are available. The model also differs from the most of the other methods described in structural design documents and models published in the literature by its ability to evaluate the actual type and amount of fibers used in the mix. Thus more economical and motivated use of steel fibers can be possible using the model proposed in this work.

2. Experimental pull-out test program was performed to determine the pull-out resistance of three types of commercially available steel fibers. The obtained experimental results show significant dependence of fiber pull-out resistance on the embedded length and inclination angle for straight shape fibers in particular.

3. Finite element method (FEM) and fracture mechanics were employed in order to analyze the steel fiber/concrete matrix inteface debond growth. The obtained calculation results indicate a high significance of interface properties for achieving high pull-out resistance. FEM modelling of complete pull-out process was also performed and from comparison with experimental test results, it was concluded that the elaborated FEM models are sufficient for determination of different mechanical parameters such as residual shrinkage stresses, coefficient of friction and interface fracture toughness.

4. A modelling algorithm was elaborated for prediction of load bearing capacity and post-cracking behaviour of fiber reinforced concrete elements subjected to bending loads. Previously obtained fiber pull-out laws were used as the input data in the model. The best agreement between the modelling and experimental validation results was obtained for beams with fiber content of 150 $kg/m^3$.

# REFERENCES

1. Walraven J.C. High performance fiber reinforced concrete: progress in knowledge and design codes, Materials and Structures – 42 (2009), pp.1247-1260.

2. Maidl B.R. Steel Fibre Reinforced Concrete. (1995) Berlin: Ernst, Verlag fur Architektur und techn. Wiss.

3. Oh B.H., Kim J.C., Choi Y.C. Fracture behavior of concrete members reinforced with structural synthetic fibers, Engineering Fracture Mechanics – 74 (2007), pp.243-257.

4. Stahli P., van Mier J.G.M. Three-fibre-type hybrid fibre concrete, Proceeding FRAMCOS-5, Vail, USA: ed. V.C. Li et al, (2004), pp.1105-1112.

5. Rossi P., Arca A., Parant E., Fakhri P. Bending and compressive behaviors of a new cement composite, Cement and Concrete Research. –35 (2003). pp.27-33.

6. Banthia N., Trottier J. Micromechanics of steel fiber pull-out: Rate sensitivity at very low temperatures, Cement & Concrete Composites – 14 (1992), pp.119-130.

7. Barragán B.E., Gettu R., Martin M.A., Zerbino R.L. Uniaxial tension test for steel fibre reinforced concrete – a parametric study, Cement & Concrete Composites – 25 (2003), pp.767-777.

8. Bayramov F., Taşdemir C., Taşdemir M.A. Optimisation of steel fibre reinforced concretes by means of statistical response surface method, Cement & Concrete Composites – 26 (2004), pp.665-675.

9. Cailleux E., Cutard T., Bernhart G. Pullout of steel fibres from a refractory castable: experiment and modelling, Mechanics of Materials – 37 (2005), pp.427-445.

10. Zhou Y., Li C., Mason J.J. Fiber-end deformation effects in enlarged-end, fiber-reinforced composites, Engineering Fracture Mechanics – 72 (2005), pp.1980-1992.

11. Banthia N., Pigeon M. Load relaxation in steel fibres embedded in cement matrices, International Journal of Cement Composites and Lightweight Concrete – 11 (1989), pp.229-234.

12. Hu X.D., Day R., Dux P. Micro-mechanical approximation to the stress field around an inclined fiber of FRCC, Mechanics Research Communications – 29 (2002), pp.27-34.

13. Pupurs A., Krasņikovs A., Kononova O., Šahmenko G. Non-linear post-cracking behaviour prediction method for high concentration steel fibre reinforced concrete (HCSFRC) beams, Scientific Proceedings of Riga Technical University (Architecture and Construction Science) – 8 (2007), pp. 60.-70.

14. Li Z., Perez Lara M.A., Bolander J.E. Restraining effects of fibers during non-uniform drying of cement composites, Cement and Concrete Research. – 36 (2006), pp.1643-1652.
15. Choi O.C., Lee C. Flexural performance of ring-type steel fiber-reinforced concrete, Cement and Concrete Research – 33 (2003), pp. 841-849.
16. Naaman A.E. SIFCON: tailored properties for structural performance in high performance fiber reinforced cement composites, Proceedings of the international workshop held by RILEM, ACI and others, Mainz, Germany (1991).
17. Kristulovic-Opara N., Dogan E., Uang C.M., Haghayeghi A.R. Flexural behaviour of composite R.C.-Slurry Infiltrated Mat Concrete (SIMCON) members, ACI Structural Journal – 94 (1997), pp.502-512.
18. Habel K., Viviani M., Denarie E., Bruhwiler E. Developement of the mechanical properties of an Ultra-High Performance Fiber Reinforced Concrete (UHPFRC), Cement and Concrete Research – 36 (2006), pp.1362-1370.
19. Chan Y.W., Chu S.H. Effect of silica fume on steel fiber bond characteristics in reactive powder concrete, Cement and Concrete Research. – 34 (2004), pp.1167-1172.
20. Serna P., Arango S., Ribeiro T., Nunez A.M., Garcia-Taengua E. Structural cast-in-place SFRC: technology, control criteria and recent applications in Spain, Materials and Structures – 42 (2009), pp.1233-1246.
21. Bruhwiler E., Denarie E. Rehabilitation of concrete structures using ultra high performance fibre reinforced concrete, Proceedings of second international symposium on ultra high performance concrete – (2008), Tokyo, Japan, pp.895-902.
22. Rokugo K., Kanda T., Yokota H., Sakata N. Applications and recommendations of high performance fiber reinforced cement composites with multiple fine cracking (HPFRCC) in Japan, Materials and Structures – 42 (2009), pp.1197-1208.
23. Bache H.H. Densified cement/ultra fine particle based materials, Second international conference on superplasticizers in concrete – (1991), Ottawa, Canada.
24. Foster S.J. The application of steel-fibres as concrete reinforcement in Australia: from material to structure, Materials and Structures – 42 (2009), pp.1209-1220.
25. Groth P. Fibre reinforced concrete, Doctoral Thesis, Luleå University of Technology, (2001), Luleå, Sweden.
26. Phyl T. Tragverhalten von Stahlfaserbeton, Doctoral Thesis, Eidgenössische Technische Hochschule Zürich, (2003), Zürich, Switzerland.
27. Markovic I. High performance hybrid fiber concrete: development and utilization. Doctoral Thesis, Delft University of Technology, (2006), Delft, Netherlands.

28. Löfgren I. Fibre reinforced concrete for industrial construction – a fracture mechanics approach to material testing and structural analysis, Doctoral Thesis, Chalmers University of Technology, (2005), Gothenburg, Sweden.
29. Laranjeira F. Design-oriented constitutive model for steel fiber reinforced concrete, Doctoral Thesis, Universitat Politecnica de Catalunya, (2010), Barcelona, Spain.
30. Carlswärd J. Shrinkage cracking of fiber reinforced self compacting concrete overlays – test methods and theoretical modelling, Doctoral Thesis, Luleå University of Technology, (2006), Luleå, Sweden.
31. Benthur A., Mindess S. Fibre reinforced cementitious composites, (2007), 2nd edition, New York: Taylor and Francis.
32. Johnston C. Fiber-Reinforced Cements And Concretes, (2000), London: Taylor and Francis.
33. Htut T., Foster S. Fracture Processes in Steel Fibre Reinforced Concrete, (2011), Saarbrucken: VDM Verlag Dr. Muller Aktiengesellschaft & Co.
34. Charron J.P., Denarie E., Bruhwiler E. Permeability of UHPFRC under high stresses, Proceedings of RILEM symposium, advances in concrete through science and engineering, (2004), Evanston, Il., USA.
35. Wuest J., Denarie E., Bruhwiler E. Model for predicting the UHPFRC tensile hardening response, Proceedings of 2nd international symposium on ultra high performance concrete, (2008) University of Kassel, Germany, pp.153–160.
36. Kang, S.-T., Lee, Y., Park, Y.-D., Kim, J.-K. Tensile fracture properties of an Ultra High Performance Fiber Reinforced Concrete (UHPFRC) with steel fiber, Composite Structures – 92 (2010), pp.61-71.
37. Banthia N., Trottier J. Test methods for flexural toughness characterization of fiber reinforced concrete: some concerns and a proposition, ACI Materials Journal – 92 (1995), pp.48-57.
38. Banthia N., Pigeon M. Load relaxation in steel fibres embedded in cement matrices, International Journal of Cement Composites and Lightweight Concrete – 11 (1989), pp. 229-234.
39. Hu X.D., Day R., Dux P. Biaxial failure model for fiber reinforced concrete, Journal of Materials in Civil Engineering – 15 (2003), pp.609-615.
40. Tsai J., Patra A.K., Wetherhold R. Numerical simulations of fracture-toughness improvement using short shaped head ductile fibers, Composites: Part A. – 34 (2003), pp. 1255-1264.

41. Zhou Y., Li C., Mason J.J. Fiber-end deformation effects in enlarged-end, fiber-reinforced composites, Engineering Fracture Mechanics. –72 (2005), pp.1980-1992.
42. Banholzer B., Brameshuber W., Jung W. Analytical simulation of pull-out tests – the direct problem, Cement & Concrete Composites – 27 (2005), pp.93-101.
43. Banholzer B., Brameshuber W., Jung W. Analytical simulation of pull-out tests – the inverse problem, Cement & Concrete Composites – 28 (2006), pp.564-571.
44. Georgiadi-Stefanidi K., Mistakidis E., Pantousa D., Zygomalas M. Numerical modelling of the pull-out of hooked steel fibres from high-strength cementitious matrix, supplemented by experimental results, Construction and Building Materials – 24 (2010), pp.2489–2506.
45. Krasnikovs A., Pupurs A. High Performance Steel Fiber Reinforced Concrete (SFRC) Fracture. Fiber Pull-out Experimental Investigation, 8th International Symposium on Utilization of High-Strength and High-Performance Concrete, (2008) Tokyo, Japan, pp.703-708.
46. Laranjeira, F., Aguado, A., Molins, C. Predicting the pullout response of inclined straight steel fibers, Materials and Structures – 43 (2010), pp.875-895.
47. Naaman, A.E., Shah, S.P. Pullout mechanism in steel fiber reinforced concrete, ASCE J Struct Div. – 102 (1976), pp.1537-1548.
48. Cunha V.M.C.F., Barros J.A.O., Cruz J.S. Pullout behaviour of hooked-end steel fibres in self-compacting concrete, Report 07-DC/E06, (2007), Universidade do Minho, Guimares.
49. Leung C.K.Y., Shapiro N. Optimal steel fiber strength reinforcement of cementitious materials, Journal of Materials in Civil Engineering – 11 (1999), pp.116-123.
50. di Prisco M., Plizzari G., Vandewalle L. Fibre reinforced concrete: new design perspectives, Materials and Structures – 42 (2009), pp.1261-1281.
51. Lee M.K., Barr B.I.G. Strength and fracture properties of industrially prepared steel fibre reinforced concrete, Cement & Concrete Composites. – 25 (2003), pp.321-332.
52. Leung C.K.Y., Lai R., Lee A.Y.F. Properties of wet-mixed fiber reinforced shotcrete and fiber reinforced concrete with similar composition, Cement and Concrete Research – 35 (2005), pp.788-795.
53. Gettu, R., Gardner, D.R., Saldívar, H., Barragán, B.E. Study of the distribution and orientation of fibers in SFRC specimens, Materials and Structures – 38 (2005), pp.31-37.
54. Habel K., Viviani M., Denarie E., Bruhwiler E. Developement of the mechanical properties of an Ultra-High Performance Fiber Reinforced Concrete (UHPFRC), Cement and Concrete Research – 36 (2006), pp.1362-1370.

55. Singh S.P., Kaushik S.K. Fatigue strength of steel fibre reinforced concrete in flexure, Cement & Concrete Composites – 25 (2003), pp.779-786.
56. Lim T.Y., Paramasivam P., Lee S.L. Analytical Model for Tensile Behavior of Steel-Fiber Concrete, ACI Materials Journal – 84(1987), pp.286-298.
57. Lok T.S., Xiao L. Tensile behavior and moment-curvature relationship of steel fibre reinforced concrete, Magazine of Concrete Research – 50(1998), pp.359-368.
58. Vandewalle L., et al. Recommendation of RILEM TC162-TDF: test and design methods for steel fibre reinforced concrete: design of steel fibre reinforced concrete using the σ−ω method: principles and applications, Materials and Structures – 35 (2002), pp.262-278.
59. Kooiman A.G. Modelling Steel Fibre Reinforced Concrete for Structural Design, Doctoral Thesis, Delft University of Technology, (2000), Delft, Netherlands.
60. Barragán B.E. Failure and toughness of steel fiber reinforced concrete under tension and shear, Doctoral Thesis, Universitat Politècnica de Catalunya, (2002), Barcelona, Spain.
61. di Prisco M., Ferrara L., Colombo M., Mauri M. On the identification of SFRC constitutive law in uniaxial tension, Proceedings of Sixth RILEM Symposium on Fibre-Reinforced Concretes, BEFIB, (2004), pp.827-836.
62. Lee M.K., Barr B.I.G. Strength and fracture properties of industrially prepared steel fibre reinforced concrete, Cement & Concrete Composites – 25 (2003), pp.321-332.
63. Li V.C, Stang H., Krenchel H. Micromechanics of crack bridging in fiber reinforced concrete, Materials and Structures, – 26 (1993), pp.486-494.
64. Kononova O., Krasnikovs A., Pupurs A. High Performance Steel Fiber Reinforced Concrete (SFRC) Strength. Prediction and Experimental Investigation, 8th International Symposium on Utilization of High-Strength and High-Performance Concrete, Tokyo, Japan, (2008), pp.543-548.
65. Zhang J., Li V.C. Simulation of crack propagation in fiber-reinforced concrete by fracture mechanics, Cement and Concrete Research – 34 (2004), pp.333-339.
66. Guo, X.H., Tin-Loi, F., Li, H. Determination of quasibrittle fracture law for cohesive crack models, Cement and Concrete Research, – 29 (1999), pp.1055-1059.
67. AFGC-SETRA Ultra High Performance Fibre-Reinforced Concretes. Interim recommendations, AFGC Publication, France, (2002).
68. Stalfiberbetong, rekommendationer for konstruction, utforande och provning. Betongrapport n.4., Svenska Betongforeningen, (1995).
69. Deutscher Ausschuss fur Stahlbeton (DAfStb). Guidelines for steel fiber reinforced concrete—23th Draft, richtlinie Stahlfaserbeton, DIN 1045, Annex parts 1-4., (2007).

70. Faserbeton, Osterreichische Vereinigung fur Beton und Bautechnik. OBBV, Wien international symposium dedicated to Prof. S. P. Shah, (2002).
71. CNR-DT 204. Guidelines for design, construction and production control of fiber reinforced concrete structures, National Research Council of Italy, Italy, (2006).
72. СП 52-104-2006 „Сталефибробетонные конструкции", Moscow, Russia, (2006).
73. ACI Committee 544. Design considerations for steel fiber reinforced concrete. ACI 544.4R-88, American Concrete Institute, (1996).
74. ACI Committee 318. Building Code and commentary, Report ACI 318-08/318R-08., American Concrete Institute, (2008).
75. Vandewalle L., et al. Recommendation of RILEM TC162-TDF: test and design methods for steel fibre reinforced concrete: σ−ε design method (final recommendation), Materials and Structures – 36 (2003), pp.560-567.
76. Japan Society of Civil Engineers. Recommendations for design and construction of high performance fiber reinforced cement composite with multiple fine cracks (draft), Concrete Library 127, (2007).
77. Kanda T., Sakata N., Kunieda M., Rokugo K. State-of-the-art of high performance fiber reinforced cement composite research, Concr J. – 44 (2006), pp.3–10.
78. Lambrechts A.N. The variation of steel fibre reinforced concrete characteristics. Study on toughness results 2002–2003, Fiber Reinforced Concrete: from theory to practice. International workshop on advances in Fiber Reinforced Concrete. Starrylink Editrice, Brescia, Italy, (2004), pp.135–148.
79. Minelli F., Plizzari G. Fiber reinforced concrete characterization: round panel vs. beam test toward a harmonization, Proceedings of 3rd central European congress on Concrete Engineering, Visegrad, Hungary, Publishing Company of Budapest University of Technology, Budapest, Hungary, (2007), pp.213–220.
80. Robins P., Austin S., Jones P. Pull-out behaviour of hooked steel fibers, Materials and Structures – 35 (2002), pp.434-442.
81. Krenchel H. "Fibre spacing and specific fibre surface" in "Testing and Test Methods of Fibre Cement Composites", Proceedings of RILEM Symposium, (1978), pp.69-79.
82. Cotterell B., Mai Y.W. Fracture Mechanics of Cementious Materials, (1995), Melbourne: Blackie Academic & Professional.
83. Banthia N., Yan C. Bond-slip characteristics of steel fibers in high reactivity metakaolin (HRM) modified cement-based matrices, Cement and Concrete Research, – 26 (1996), pp.657-662.

84. ANSYS Release 11.0, ANSYS Academic Research, (2007) ANSYS Inc., Canonsburg, Pennsylvania
85. Pupurs A., Varna J. Energy release rate based fiber/matrix debond growth in fatigue. Part I: Self-similar crack growth, Mechanics of Advanced Materials and Structures, In Press (2010).
86. Pupurs A., Krasņikovs A., Varna J. Energy release rate based fiber/matrix debond growth in fatigue. Part II: Debond growth analysis using Paris law, Mechanics of Advanced Materials and Structures, In Press (2010).
87. Wu W., Verpoest I., Varna J., Prediction of energy release rate due to the growth of an interface crack by variational analysis, Compos. Sci. Technol. – 60 (2000), pp.351-360.
88. Graciani E., Mantič V., París F., Varna J., Numerical analysis of debond propagation in the Single Fibre Fragmentation Test, Compos. Sci. Technol. – 69 (2009), pp.2514-2520.
89. Nairn J.A., A variational mechanics analysis of the stresses around breaks in embedded fibers, Mech. Mater. – 13 (1992), pp.131-154.
90. Irwin G.R., Fracture, Handbuch der Physik, vol.5, (1958), Springer Verlag, Berlin.
91. Krueger R., Goetze D. Influence of Finite Element Software on Energy Release Rates Computed Using the Virtual Crack Closure Technique, National Institute of Aerospace (NIA) Report Nr. 2006-06, (2006).
92. Pupurs A., Varna J. Fracture mechanics analysis of debond growth in a single-fiber composite under cyclic loading, Mechanics of Composite Materials, – 47 (2011), pp.109-124.
93. Alfano G., Crisfield M.A. Finite element interface models for the delamination analysis of laminated composites: Mechanical and computational issues, International Journal for Numeriacal Methods in Engineering, – 50 (2001), pp.1701-1736.
94. MATLAB Release 7.9, (2009).

# APPENDIX

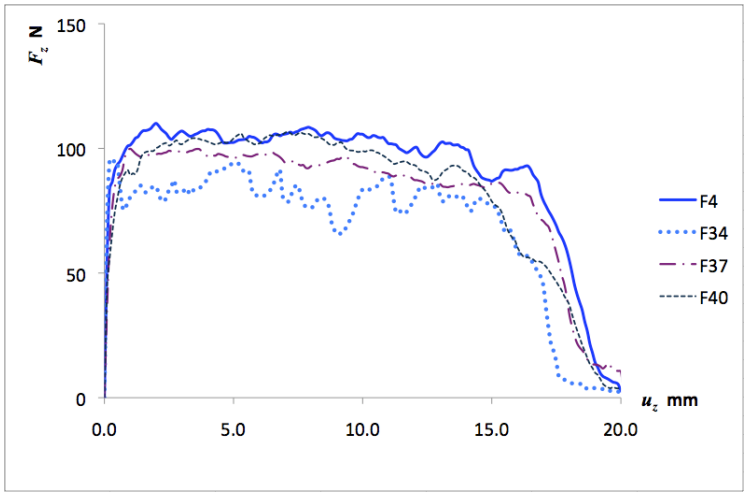


Fig.A1. Average pull-out curves for inclined straight fibers with embedded length $l_f = 20$ mm: F4 ($\alpha = 0°$); F34 ($\alpha = 30°$); F37 ($\alpha = 45°$ ); F40 ($\alpha = 60°$ )

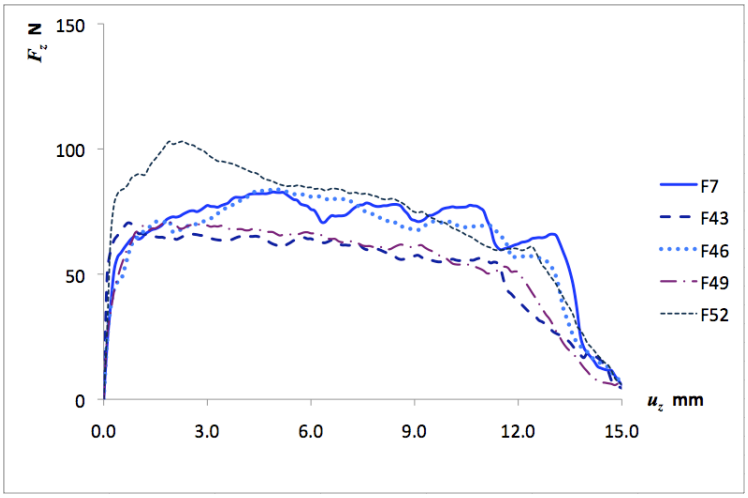


Fig.A2. Average pull-out curves for inclined straight fibers with embedded length $l_f = 15$ mm: F7 ($\alpha = 0°$); F43 ($\alpha = 20°$);F46 ($\alpha = 30°$); F49 ($\alpha = 45°$); F52($\alpha = 60°$)

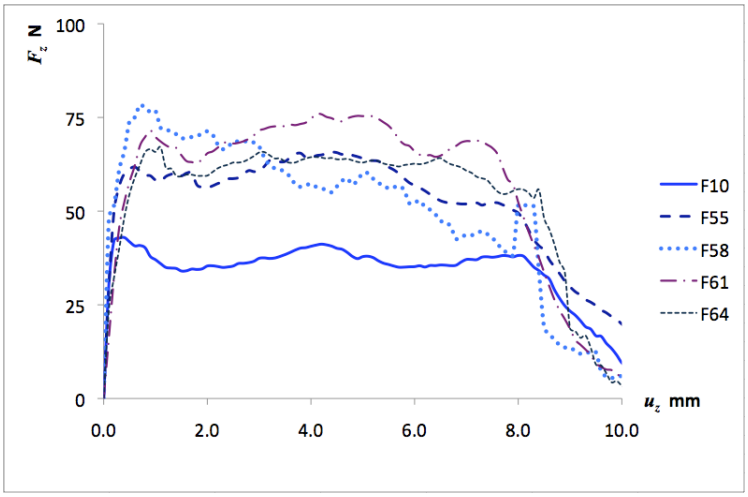


Fig.A3. Average pull-out curves for inclined straight fibers with embedded length $l_f = 10$ mm: F10 ($\alpha = 0°$); F55 ($\alpha = 20°$); F58 ($\alpha = 30°$); F61 ($\alpha = 45°$); F64 ($\alpha = 60°$)

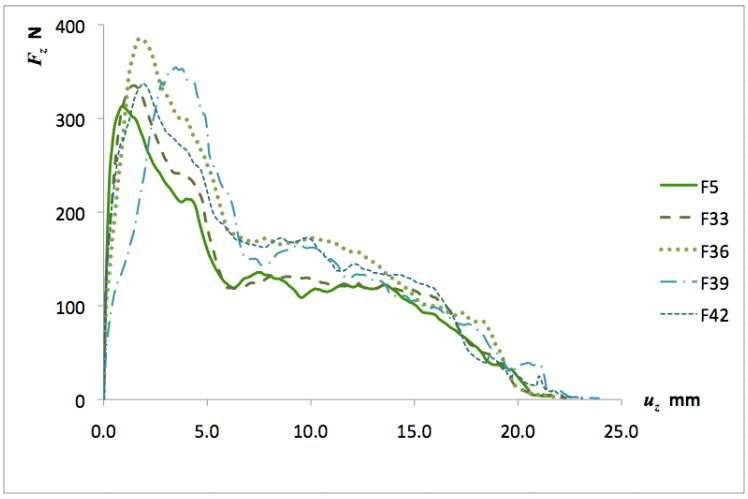


Fig.A4. Average pull-out curves for inclined hooked-end fibers with embedded length $l_f = 20$ mm: F5 ($\alpha = 0°$); F33 ($\alpha = 20°$); F36 ($\alpha = 30°$); F39 ($\alpha = 45°$); F42 ($\alpha = 60°$).

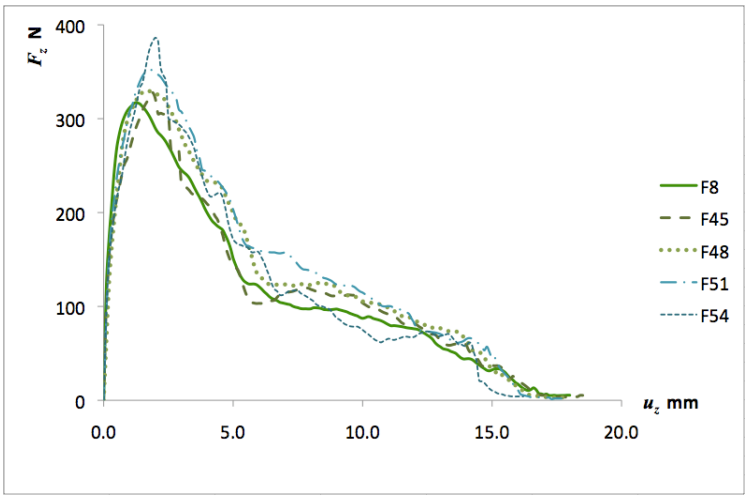


Fig.A5. Average pull-out curves for inclined hooked-end fibers with embedded length $l_f = 15$ mm: F8 ($\alpha = 0°$); F45 ($\alpha = 20°$); F48 ($\alpha = 30°$); F51 ($\alpha = 45°$); F54 ($\alpha = 60°$)

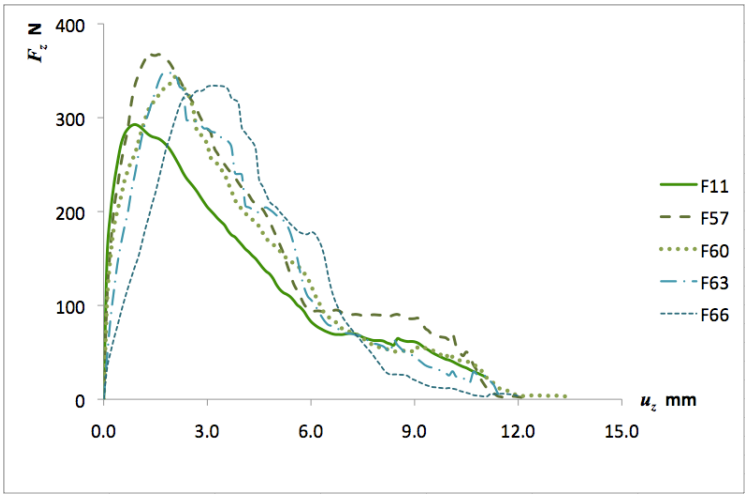


Fig.A6. Average pull-out curves for inclined hooked-end fibers with embedded length $l_f = 10$ mm: F11 ($\alpha = 0°$); F57 ($\alpha = 20°$); F60 ($\alpha = 30°$); F63 ($\alpha = 45°$); F66 ($\alpha = 60°$)

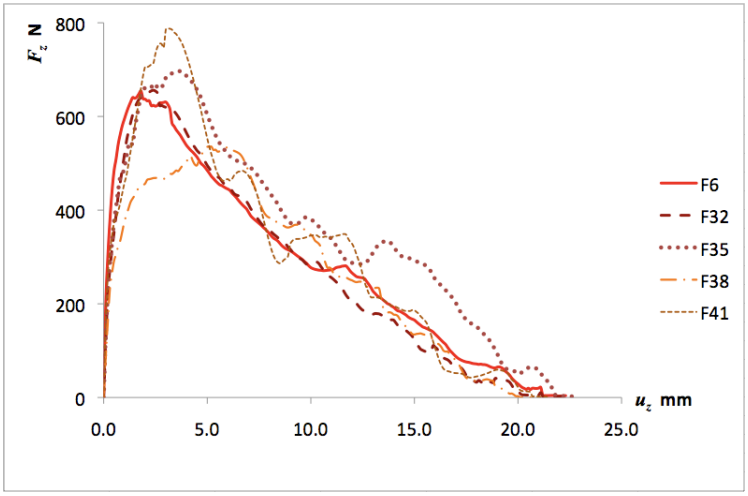


Fig.A7. Average pull-out curves for inclined undulated shape fibers with embedded length $l_f = 20$ mm: F6 ($\alpha = 0°$); F32 ($\alpha = 20°$); F35 ($\alpha = 30°$); F38 ($\alpha = 45°$); F41 ($\alpha = 60°$)

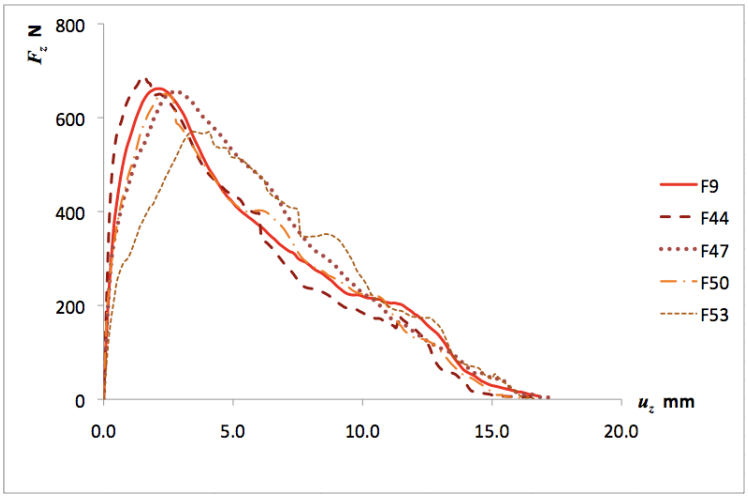


Fig.A8. Average pull-out curves for inclined undulated shape fibers with embedded length $l_f = 15$ mm: F9 ($\alpha = 0°$); F44 ($\alpha = 20°$); F47 ($\alpha = 30°$); F50 ($\alpha = 45°$); F53 ($\alpha = 60°$)

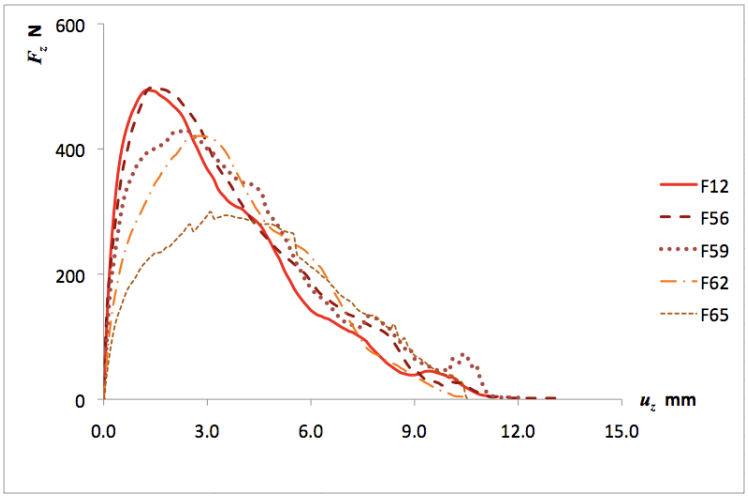


Fig.A9. Average pull-out curves for inclined undulated shape fibers with embedded length $l_f = 10$ mm: F12 ($\alpha = 0°$); F56 ($\alpha = 20°$); F59 ($\alpha = 30°$); F62 ($\alpha = 45°$); F65 ($\alpha = 60°$)

**Algorithm of the model described in Chapter 5 (example of a Matlab input code)**

clear; (beginning of the input code)

L=50; (length of the fiber)
Lp=L*1.1; (total length of the undulated shape fiber)
d=1; (diameter of the fiber)
NN=35; (coordinate of the critical cross-section, assumed to be in the middle of the beam span)
H=15; (height of the beam)
B=70; (total length of the beam)
C=60; (span of the beam)

ro=7800*10^-6; (density of steel (unit $g/mm^3$)

kg=150; (amount of fibers in the concrete mix (unit $kg/m^3$)

r=d/2; (fiber radius)

m=pi*r^2*Lp*ro; (weight of one fiber)

num_kg=1000/m; (number of fibers per 1 kg weight of fibers)

num _m3=kg*num_kg; (number of fibers per 1 kg of concrete mix)

num _pr=(num_m3*H*H*B*10^-6); (number of fibers in the beam sample)

num =round(num_pr); (number of fibers in the beam sample (rounded to an integer number))

fid=fopen('uTb50_1.txt','r'); (read in data from the pull-out law database)

Mas=fscanf(fid,'%g',[18,2857]); (definition of an array of read-in data with 18 columns and 2857 rows in the given example).

fclose(fid); (close the database file after reading the data and storing in array)

Mas=Mas';

for i=1: num; ("i" is the number of the fiber in consideration, "num" is the number of the last fiber)

x(i)=rand*H; (the x-coordinate of the center of gravity of the fiber)

y(i)=rand*15; (the y-coordinate of the center of gravity of the fiber)

a(i)=rand*(pi/2); (the angle of the fiber (in range between 0 and $\pi/2$ radians)

end (end of the command cycle in which given number of fibers is randomly distributed within the volume of the given sample)

```
X=x'; (x-coordinate vector)

aa=a*180/pi; (fiber inclination angle in degrees)

for j=B/2

   M(j-34)=0;

   for k=1: num; (for all fibers with numbers 1 to “num”)

      if X(k)>=j-1; (logical test if fiber with given number is within the critical cross-section, the number of fibers is found in a ±1 cm long distance from the coordinate of the critical cross-section)

         if X(k)<j;

           M(j-34)=M(j-34)+1; (the number of fibers within the assumed critical cross section)

        end

     end

   end

end

end

end

ang(9)=0; (the ranges of the fiber inclination angles (there are 9 ranges assumed in this model: 0-10°, 10°-20°, 20°-30°, 30°-40°, 40°-50°, 50°-60°, 60°-70°, 70°-80°,80°-90°))

dll(10)=0; (the ranges of the embedded lengths (there are 10 ranges assumed in this model: 0-5, 5-10, 10-15, 15-20, 20-25, 25-30, 30-35, 35-40, 40-45, 45-50))

for i=1:num; (it is verified whether the fiber will be crossing the critical cross-section of the beam)

      p1=0;p2=0; (2 endpoints of each fiber are observed)

      if X(i)-0.5*L*0.1*cos(a(i))<N p1=1;

      end

      if N<X(i)+0.5*L*0.1*cos(a(i)) p2=1;

      end
```

```
        p(i)=p1*p2;
        alfa(i)=1; (parameter showing to which range of angles the fiber belongs to)
        while alfa(i)*pi/(2*9)<a(i);
           alfa(i)=alfa(i)+1;
        end
         dl(i)=1; (parameter showing to which range of embedded lengths the fiber belongs to)
         while dl(i)*0.5<((X(i)+0.5*L*0.1*cos(a(i))-N)/cos(a(i)))*p(i);
            dl(i)=dl(i)+1;
         end
         ang(alfa(i))=ang(alfa(i))+1*p(i); (the inclination angle of the observed fiber)
         dll(dl(i))=dll(dl(i))+1*p(i); (the embedded length of the observed fiber)
      end
      angang=ang'
      dlldll=dll'

PP=0; (the resulting fiber bridging load P)
MM=0; (the corresponding bending moment M)
for z=0.2:0.2:6; (crack opening displacements from 0.2 to 6 mm with a step of 0.2 mm)
    P=0;M=0; (initial values of bridging load P and bending moment M)
    for i=1: num;
        b=z*(0.8*H-y(i))/(0.8*H); (local crack opening b corresponding to height coordinate y)
        end
        Pm=Mas(x,2*alfa(i)); (the value of the load corresponding to local crack opening b)
        P=P+Pm*p(i); (the values of the transferred load are accumulated for all fibers crossing
the crack in the critical cross-section)
        M=M+Pm*p(i)*((0.8*H-y(i))/100); (the values of the bending moment are accumulated)
```

```
    end
    PP=[PP;P]; (array of the transferred load)
    MM=[MM;M]; (array of the bending moment)
end
Pg=2*MM/(C/3); (the values of the externally applied load)
```